Atmospheric Aerosol Characterization Using Lidar Power Profile
&
UPRM Lidar Development

by

Javier Méndez Rodríguez

A project report submitted in partial fulfillment of the requirements for the degree of
MASTER OF ENGINEERING
in
ELECTRICAL ENGINEERING

UNIVERSITY OF PUERTO RICO
MAYAGÜEZ CAMPUS
JUNE 2009

Approved by:

_____   _____
Hamed Parsiani, PhD   Date
President, Graduate Committee

_____   _____
José Rosado, PhD   Date
Member, Graduate Committee

_____   _____
Ramón Vásquez, PhD   Date
Member, Graduate Committee

_____   _____
Agustín Rullán, PhD   Date
Representative of Graduate Studies

_____   _____
Chairperson of the Department   Date

Atmospheric Aerosol Characterization Using Lidar Power Profile & UPRM Lidar Development

By
Javier Méndez Rodríguez
June 2009

Chair: Hamed Parsiani
Major Department: Electrical and Computer Engineering

This work presents the implementation of a multi-wavelength Lidar system at the UPRM (University of Puerto Rico at Mayagüez) located at the western region of the island of Puerto Rico. The UPRM-Lidar system is situated close to the coastal region where sea-salt particles and mountains play an important role in cloud formation. Remote measurements with this system provide vertical and horizontal remote sensing information of backscatter and extinction coefficient of aerosol, cirrus clouds, upper troposphere, PBL (Planetary Boundary Layer), and other events such as: Saharan dust, smoke, volcano haze, etc.

The UPRM-Lidar system is based on the laser transmission wavelengths of 355, 532, and 1064nm and the detection of elastic backscatter light (same wavelengths). Profiles of backscatter and extinction coefficients of aerosols and clouds at different heights are obtained using algorithms developed in this research to determine the aerosols size distributions, particle matter concentrations, air quality indices, and others.

Resumen de Disertación Presentado a Escuela Graduada de la Universidad de Puerto Rico

como requisito parcial de los Requerimientos para el grado de Maestría en Ingeniería

Eléctrica

Caracterización de Aerosoles Atmosféricos Utilizando Perfiles de Potencia de un Lidar y Desarrollo del UPRM Lidar

Por
Javier Méndez Rodríguez
Junio 2009

Consejero: Hamed Parsiani
Departamento: Ingeniería Eléctrica y Computadoras

Este trabajo tiene como objetivo la implementación de un sistema de Lidar de múltiples largos de ondas (UPRM-Lidar) en la UPRM (Universidad de Puerto Rico en Mayagüez) localizado en la región oeste de la isla de PR (Puerto Rico) (18^012'4N, 67^008'24W, y una elevación de 13m sobre el nivel del mar). El sistema de UPRM-Lidar se encuentra situado cerca de la región costera, donde las partículas de sal y montañas juegan un papel importante en la formación de nubes. Mediciones remotas de este sistema proveen información vertical y horizontal de los coeficientes de extinción y de retrodispersión (backscatter) de aerosoles, nubes cirrus, parte alta de la tropósfera, PBL, y otros eventos como los son: polvo del desierto de Sahara, humo, etc.

El sistema de UPRM-Lidar está basado en un láser que transmite los largos de onda de 355, 532 y 1064nm y que detecta la luz elástica reflejada por la atmósfera a los mismos

tres largos de onda transmitidos. Perfiles de los coeficientes de extinción y de retrodispersión de los aerosoles y nubes en diferentes alturas son obtenidas utilizando algoritmos desarrollados en esta investigación para determinar las distribuciones de los tamaños de los aerosoles, concentraciones de partículas y el índice de la calidad del aire, entre otros.

To GOD . . .

To my Family…

To Loraine, for her unconditional support…

To everyone who has goals, challenges, and works hard to continue forward in their life…

Acknowledgements

past years. Special thanks to Henry Rodríguez and Allen Lizarraga for their collaboration in the correction of this work.

Thanks to all my class partners in special to Wilma and Sol for their friendship, and thanks to Sandra Montalvo and Yakaira Pérez for their friendship and patience to help me in some occasions. Finally, thanks to my father Santiago, my mother Nilda, my brother Gabriel and my love Loraine for believing in me, and for their unconditional love and support.

Table of Contents

x

Table List

TABLES

Figure List

FIGURES

xiii

1 INTRODUCTION

Life consist on a cycle where the natural elements drive, transport, and exchange the energy and matter defined in time and space that are related with life on Earth. These natural cycles are affected by the human activities, having a negative impact that affect the human life itself. These activities are responsible of the Earth perturbation, where the GW (global warming) is the most popular today.

The global perturbations start with the soil restoration and deforestation, but this increase in magnitude with the industrial revolution [1]. The environmental natural substances began to be strongly affected by the exploitation of natural resources. The creation of new products and their use have the responsibility of the environmental perturbation, affecting direct or indirect the environment and natural cycles between the air, waste, and soil systems. "The short term (local area) effects are discovered rapidly by the human community and fast solutions are applied, but the long term (global area) effects are more difficult to discover, and the solutions are more difficult to find" [2].

The atmosphere is definitely involved in this environmental problem in all its processes. The short term concerns the problem of air quality, and the long term concerns the Earth radiation budget, GW, surface Albedo (cooling), and others. These two issues (short and long term) cause an important effect in the meteorological process to drive regional air pollution and subsequently influence the climate change. The regional air pollution problem is caused by the gases emission, dessert dust, haze, fog and aerosols. The

gasses emissions caused by industries which are responsible of volatile organic carbons (VOC) and cars which are responsible of NO_2 [1,2] are affecting the clouds properties which play an important role in the Earth's energy balance, where the negative impact is the GW or the albedo effect. The regional air quality is affected by the air pollution and this problem is concerning in the first 3km of the atmosphere, strongly influenced by the PBL (planetary boundary layer). The magnitude of the pollution effects depends on the intensity, type and distribution of the emissions sources. For example, the air pollution is driven by the regional dynamics of the PBL, topography, and meteorological conditions [3]. To control the regional air pollution many countries are created ACTs and protocols to regulate the emissions, meanwhile other countries are creating government agencies to supervise and regulate emissions.

This project report presents a state of the art Lidar system as an innovative method for atmospheric measurements, as a necessary component in a future global Lidar Network to help understand the effects of the atmospheric compounds in radiative forcing climate. The implementation of the UPRM Lidar laboratory helps scan the atmosphere in a vertical column at different altitudes. These new measurements concern the troposphere region (first 10 to 12km of the atmosphere) and are based on a multi-wavelength Lidar system implemented at the Electrical and Computer Engineering (ECE) Building. Right now, the Lidar consist in the three basic wavelengths of 355, 532, and 1064nm, which are transmitted and received (elastic channels). These three channels are used to study the tropospheric aerosols, but the staff is working on the evaluation to add inelastic (Raman) channels to study the q_{H2O} (water vapor mixing ratio) and RH (relative humidity). By analyzing the received

signal suitable at the mentioned wavelengths, one may retrieve: optical parameters such as α (extinction) and β (backscatter) coefficient of aerosol and clouds, AOD (aerosol optical depth), and ASD (aerosol size distributions), and microphysical parameters (effective radius, total surface area, total volume concentration, etc.), and atmospheric concentrations such as WV (water vapor) with high space-time resolution.

1.1 Problem Statement

Atmospheric aerosols are important in numerous atmospheric processes. They have considerable influence in the air quality, Earth's radiation budget, clouds, and precipitation. Scattering and absorption of incoming solar and long-wave terrestrial radiation by the different particles found on Earth cause direct climate forcing, whereas indirect climate forcing can be attributed to the influence of particles in the size distribution of cloud droplets, thus change their optical properties. To understand better the importance of atmospheric particles and aerosols, the investigation of the spatial and temporal variability of their chemical and physical properties is imperative to describe their mean size, their volume or mass, surface-area, number concentrations, and their complex refractive index. To gain information on aerosol-particles parameters, a Lidar system has been used to obtain the optical information (α and β coefficient) of the atmosphere [4].

The importance of this research is to study the aerosols in the Caribbean region, since there are different types of aerosols. The objective of this project is observing the aerosol interaction in the Western part of PR with the implementation of a Lidar System. The Lidar

scan the atmosphere at different altitudes and give us raw data, which is used to study the aerosols. The aerosols characterization can improve weather prediction, and do so with a more exact approach. The aerosol characterization which is the projects topic shows that the aerosol microphysical plays an important role in atmospheric process and in air quality. The small aerosol component known as $PM_{2.5}$ (particle matter with radius, $r \leq 2.5\mu m$), and are the most concern to human health because smaller particles can be easily inhaled into the lungs [5]. Along with the health issues, the size distribution and r_{eff} have significant implications for aesthetics of natural environment and for climatic change [5].

1.2   Objectives

1.2.1   Aerosol Characterization Using Lidar Raw Data

The objective of this research is the algorithm development for determining different aerosol parameters. The data is obtained from a Lidar system at the three wavelengths of 355, 532, and 1064nm. The data will be obtained from the UPRM-Lidar which is ready to collect data. However, the developed algorithms could also be verified using any other Lidar data. The CCNY (City Collage of New York) has made available their Lidar data at the indicated three wavelengths for this project, and has data of two additional wavelength (387, & 407nm) known as Raman channels of 355nm used also in this research.

MatLab based algorithms have developed which permit the determination of α and β coefficient, AOD leading to the calculation of ASD and microphysical parameters. The

microphysical parameter corresponds to r_{eff}, a_t (total area), v_t (total volume), and n_t (total number of particles per cm^{-3}). The calculation of the molecular α and β coefficient are based on the ASA76 (USA atmospheric standard assumptions 1976) for pressure and temperature. The results of power profiles, β and α coefficients, AOD, ASD, microphysical parameters, and logarithmic power intensity images will be presented in this project [6, 7].

1.2.2   UPRM Lidar Development

The UPRM Lidar Laboratory system and the function of each component are presented in this project (Appendix F). Also, the result of the data collected in Mayagüez on March 24th, 2009 is presented and discussed in this work (Chapter 4 & 5).

1.3   Contributions

The important contribution in this work is based on the developing of aerosol characterization algorithms, and the UPRM-Lidar assemble, test and data collection processes.

1.4   Project Outline

This project report is organized as follow: Chapter 2 shows the theoretical literature review, Chapter 3 presents the Lidar technique theory based on mathematical methods, Chapter 4 shows the Lidar systems as a remote sensing tool, Chapter 5 presents the aerosol

characterization algorithm results and analysis, and Chapter 6 shows the conclusions and recommended future work.

2 LITERATURE REVIEW

Remote sensing is defined in this project as the measurement of the object under study, such as properties suspended on the atmosphere or Earth's surface using data acquired from Lidar, satellite, and aircraft. It is an attempt to measure something at a distance, rather than *in situ*. The remote sensing techniques are composing of two types, passive and active systems. Passive remote sensing systems use the sunlight as a light source, and active remote sensing techniques employ an artificial light source of radiation as a probe.

This Chapter presents the Literature review of the principal topics covered in the developed research, obtained from other works. The Lidar system is introduced as a remote sensing tool, and then the atmospheric region under study is presented with a brief characterization of the object to be studied. Finally, different types of scattering used in Lidar systems are presented, and is presented the ASA76 which is used to study the natural molecules suspended in the atmosphere [8].

2.1 Lidar System

Lidar is the acronym for LIght Detection And Ranging, commonly referred as a laser radar [9]. A Lidar system transmits a light beam at a certain wavelengths that interacts with the object under study. Some of the emitted light is scattered back toward the Lidar and is collected by a telescope. Then, the collected light is separated by a detector system into the

different wavelengths, generating a signal per wavelength. The measured signals are then analyzed to obtain measurements of atmospheric constituents and properties.

Lidar operates in the same way as radar, but the difference between Lidar and radar is the wavelength of radiation used. Radar operates in the radio bands meanwhile Lidar use the light in form of particles such as photons. The light wavelengths used in Lidar systems depend on the types of measurements being made. The wavelength varies from the UV (ultra violet) through the V (visible), and into the NIR (near infrared). The Lidar has many different applications, but its major use is in remote sensing [9].

Comparing Lidar systems with the common remote sensing system such as radars, the Lidar system is a better choice to study a specific object because has a greater ability to reflect images with good spatial and temporal resolutions. Radars data collection systems involve aiming wavelengths at the target and waiting for a reflection, it is usually possible to collect information for objects with the same size as the wavelength or different [9]. Lidar uses waves ten to one hundred thousand times shorter than radar waves, meaning that is able to collect much data with more characteristic of the object under study. The problem with the Lidar system is that it could not operate during the rain because the system is very sensitive in detection and in hardware.

2.2 Lidar System for Atmospheric Studies

The Lidar is a sophisticate system used in this research to take remote measurements of particles, aerosol, molecules, and clouds suspended in the atmosphere. The atmospheric

Lidar relies on the interactions, scattering and absorption of light beam with the atmosphere [10]. The Lidar generate a light pulse direct to the atmosphere, and then collect the backscatter light to analyze the different properties of the atmosphere that cause the backscatter. Different atmosphere parameters can be measured, depending of the Lidar design and location. For this reason the majority of Lidar systems have a receiver with multiple wavelengths. A specified wavelength helps us to study the different atmospheric parameters, for example: aerosols and cloud properties, wind velocity, temperature, SSA (Single Scattering Albedo), and others. A general block diagram of the proposed Lidar system is shown in Fig. 2-1 [10].
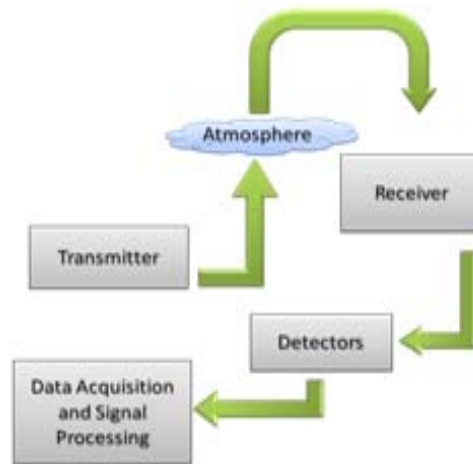
Figure 2-1 Basics Lidar block diagram.

This system consists of the following parts: Transmitter, Receiver, Detection, and Data Acquisition and Signal Processing. The transmitter is the part of the Lidar that generates a light pulse direct to the atmosphere. The receiver system collects and processes the scattered laser light, and directs it into the photo-detector (sensors). The photo-detector is

9

a device that converts the light to an electric signal. The detection and data acquisition takes the light from the receiver and produces a record of the measure intensity as a function of altitude [10].

2.2.1 History

The Lidar technology starts early on the 19th century when Synge proposed the first method for determining the atmospheric density profile. The proposed methodology was based on detecting scattering from a beam of light projected into the atmosphere, using an anti-aircraft searching light as a beam source and a large telescope as a receiver. "This methodology is based on the bistatic configuration, where the source of light and the receiver are several kilometers separated. The receiver field of view (FOV) could be scanned along the searching beam to obtain a height profile of the scattered light's intensity from simple geometric considerations. The lights could be detected using a photoelectric apparatus. To improve the signal level and thus increase the maximum altitude, Synge also suggested a large array of several hundred searchlights could be used to illuminate the same region of the sky" [11].

The first results of the proposed method were reported by Duclaux. He was taking photography of the backscatter light around a distance of 2.4km from the search light using f/15 lens and exposure of 1.5hours, the light was visible at an altitude of 3.4km. Then, in 1936 Hulbert extended these results taken photography of 28km of altitude and he made calculations of atmospheric density profiles from his measurements [9].

The suggested Lidar type is known today as biaxial Lidar. Modern systems use the monostatic configuration where the transmitter and the receiver are in the same location. Fig. 2-2 shows the Lidar typical configuration where the monostatic systems are sub-divided in two categories, coaxial and biaxial systems. In the coaxial systems the laser beam is transmitted coaxially with the receiver's FOV. While, in the biaxial system the transmitter and the receiver are located adjacent to each other [9].

Monostatic coaxial   Monostatic biaxial   Biaxial
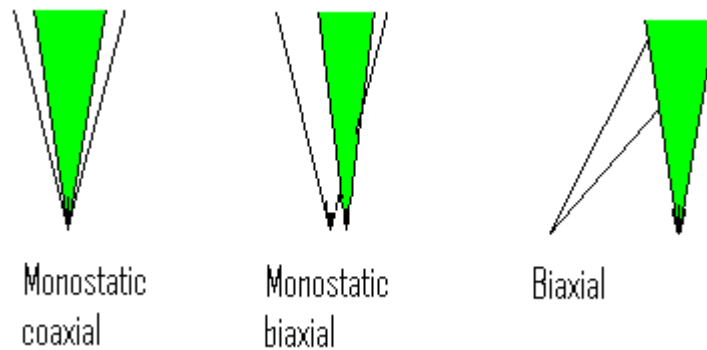
Figure 2-2 Types of receiver FOV, where green cones represent the laser beam, and the others are the receiver's FOV {adapted from:[9]}.

In 1938, the first monostatic system was used by Bureau for determining cloud heights. Bareau use light pulses as source, thus enabling the range at which the scattering occurred to be determinate from the round trip time of the scattered light pulses [9]. Fig. 2-3 shows an example of the round trip time and range in the object under study. Eqs 2.1 and 2.2 show the relation between the round trip time and range. These equations are used by Bureau to determine the clouds heights (R).

11
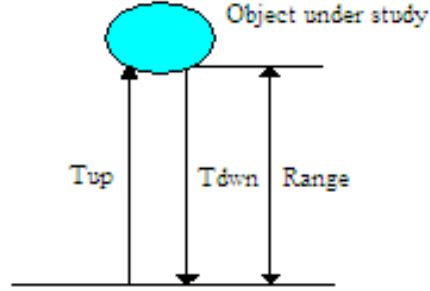
Figure 2-3 Lidar range and round trip time relationship between the object under study {adapted from [9]}.

$$t_{total} = t_{up} + t_{down} = \frac{2*R}{c} \qquad\qquad 2.1$$

$$R = \frac{t_{total} \cdot c}{2} \qquad\qquad 2.2$$

Then, density profiles up to 67.7km were calculated by Eltelman using an improved instrumentation, including electrical recording of backscattered light [9]. He used a bistatic system where the transmitter and receivers were 20.5km apart. From the measured density profiles, the temperature profiles were calculated using Rayleigh technique.

In 1956, Friedland reports the first pulsed monostatic system for measuring atmospheric density. Pulsed monostatic Lidar has the advantage to record a complete scattering profile, and have a useful signal to noise ratio. The bistatic Lidar only can detect scattering from small layer in the atmosphere at one time, and the detector must be moved to many times to obtain altitude profiles. The realignment of the detector can be difficult due to large separations and the strict alignment requirements of the beam and the FOV of the system detector. Monostatic Lidar inherently averages the measurements at all altitudes

across exactly at the same period, whereas a bistatic system takes a snapshot of each layer at a different time [9].

Lidar systems come to be more popular in 1960 with the invention of the laser, but the powerful light source of moderns Lidar comes in 1962 with the creation of the giant or Q-switched lasers. Since the invention of the laser, development of the Lidar has been closely linked to advances in laser technology. The use of a laser in Lidar systems was reporter in 1962 by Smillins and Fiocco [9], who detected laser light scattered from the lunar surface using a ruby laser that fired 0.5J pulses at 694nm. In the same year, these two same workers reported the detection of the atmospheric backscatter using the same laser system [9].

2.3   Troposphere Structure and Process

The lower atmosphere region is known as troposphere and it is divided into two parts, the PBL and free troposphere. The PBL is directly influenced by the presence of the Earth's surface and responds rapidly to forcing such as solar heating, evaporation and transpiration, frictional drag, and terrain-induced flow modification. This forcing generated turbulence, keeping this part of the atmosphere well mixed [12]. The top of the PBL is associated with the lifting condensation level at which moist air becomes sutured and starts to condensate. This issue creates a region of increasing temperature called capping inversion presented in Fig. 2-4.
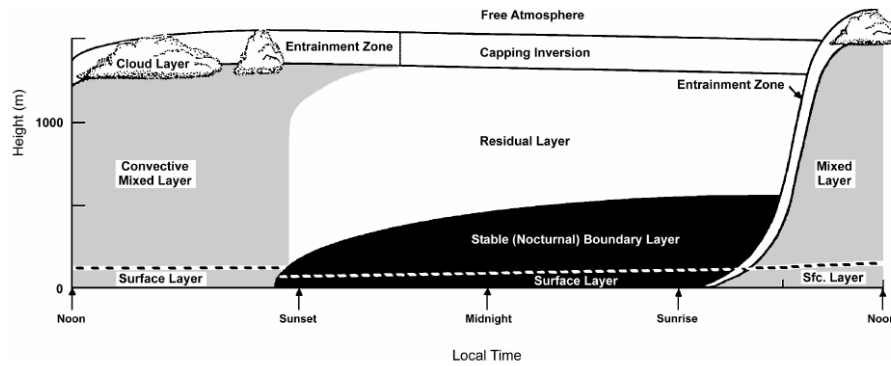
Figure 2-4 Troposphere composition {source: [12]}.

2.3.1 Planetary Boundary layer (PBL)

The PBL is affected by human activity, play an important role in weather and in climate because both processes integrate the Earth's surface such as evaporation and heat transfer with the rest of the troposphere. This energy transfer between the atmosphere and the Earth's surface is essential to describe the dynamical behavior of the atmosphere [12].

The atmosphere heating process comes from the air that absorbs the solar radiation and from the ground absorption of solar radiation, followed by the convective heat transfer in the air near the ground. The air near to the ground is started to heat at sunrise, and it becomes buoyant and rises as thermal bubbles [12]. The combination of the convection process with wind shear, produces mixing through the troposphere. This strong mixing is limited to the lowest couple of kilometers because fall rapidly above the surface, creating the boundary layer or PBL. Later at sunset, the air near the surface is cooled when the heat is removed decreasing the convective process and wind shear turbulence. After the temperature of the air near to the ground starts to cool below the temperature of air higher than it, the nighttime temperature inversion has been established, forming a stable layer between the

14

surface and the inversion altitude (Fig. 2-4) [12]. The PBL is in the range of 2-4km of altitude over continental regions during the day and 200-600m in nighttime.

The processes that take place in this layer are directly influenced by surface processes in the form of transportation and transformation of pollutants, and the chemical processes that take place dependent on the geographical location, time, and daily weather conditions [12]. There are particles in different types and sizes that play an important role in the regional atmospheric conditions and air quality [13].

2.3.2 Free Troposphere

The troposphere occupies the lowest 10 or 12km of the atmosphere. Due to the decrease in pressure with altitude, the rising surface warm air expands and cools to lower temperature. When the rising buoyant air parcel cools to the dew point, the water contained condenses. The result of this condensation allows the warm air bubbles rise higher due to the release of the latent heat as condensation. The troposphere, where the buoyant forces establish the temperature gradient and daytime surface heating, causes strong convection mixing, which is the lowest thermal layer of the atmosphere. The troposphere extends upward to the tropopause (boundary region between the troposphere and the stratosphere), which is an isothermal layer caused by the temperature balance between the solar heating from the surface and the heating from the ultraviolet absorption by the atmospheric ozone layer above [13]. The troposphere height is close 10km at mid-latitudes, but decrease less than 2 km at polar latitudes, and achieves altitudes above 15 km over the equator. One of the most important effects of the tropopause layer is its action as a barrier, where buoyant forces

15

no longer have the effect on the atmosphere mixing. Since temperature gradients determine the stability of the atmosphere, convection is seldom strong enough to bring air and its contents through this barrier where the temperature gradient becomes positive [13].

2.4   Tropospheric Aerosols

The aerosol studies have generally been focused on three areas: effects on climate, effect on human health, and effects on electro-optic systems. Scattering and absorption by particles, those in aerosols and clouds, together with the contributions from molecular scattering and absorption by gases, play a major role in determining what fraction of the solar radiation incident at the top of the atmosphere reaches the Earth's surface. In certain parts of the spectrum, the absorption by water vapor, ozone and other molecules play a dominant role in determining the transmittance. Aerosols are a major factor in determining the Earth's climate because has a direct effect on the radiation budget [10].

2.4.1 Aerosol Size Description

Aerosol is the composition of small particle in a gas, may be a solid or liquid state. The size of the particles range roughly 1nm up to 100μm. The aerosol particle lifetime in the atmosphere can extend up to weeks or in extreme cases a year [14]. Smallest particles lie on the boundary to molecular clusters have a limited lifetime by the coagulation with other particles, while for larger particles it is the deposition rate that limits the lifetime.

The aerosols particle comes from natural and anthropogenic sources. There are different types of aerosols in the atmosphere, for example: mineral particles, sulfate droplets, WV, organic compounds, dust, burning biomass and others. Aerosol particles can also arise in the form of so-called secondary aerosols through gas to particle conversion. Examples of these particles consist of sulfate formed from sulfur dioxide oxidation in cloud droplets, particles formed via condensation of hot gases emitted during combustion and particles generated from oxidation of low vapor pressure organics released from vegetation [14].

The aerosols particle has influence in the Earth's radiation budget, air quality, clouds, precipitation, and chemical processes in the atmosphere. These particles called aerosols can affect the environment and climate in several ways. The depth of aerosols (AOD) in the top of the atmosphere determines the sunlight radiation in the Earth's. The Earth's contamination helps to increase the aerosol depth (AOD) layer in the atmosphere. This is one of the principal factors that we can see today in GW effects, because the solar radiation controls the Earth's temperature. Also, plants, animals, human, and ecological systems are affected with this issue.

Aerosols from about 0.01 to 10µm in diameter are of greatest interest. Particles in this size range dominate and have direct interaction with sunlight, and also make up the majority of the aerosol mass. Small particles than 0.01µm play an important role in the interactions with clouds, and large particles than 10 µm can contribute near dust and volcanic sources which alters the clouds properties. In marine zones, giant salt particles play an important role in cloud formations [14].

A good way to represent the smaller particles is the determination of number concentration and mass of particles. Mass concentration are reported in terms of PM (particle matter), $PM_{2.5}$ and PM_{10}, which are the particulate mass per air volume of particles with radius between 0.1-2.5µm and 2.5-10 µm, respectively [5]. PM particles are divides into *Fine* and *Coarse* mode, between which the limit has been set from 0.01-2.5µm and 2.5-10 µm, respectively. This is roughly the size below which particles starts to follow the inhaled air far enough down the respiratory system. *Coarse* particles on the other hand do not so easily follow the air flow but are deposited early in the respiratory system and then removed from the body by mucus [5]. The *Fine* particles are divided into two modes, *Aitken* mode ($r \leq 0.1$ µm) and the accumulation mode ($0.1 \leq r \geq 2.5$ µm). Particles in this size mode are short lived. Fig. 2-5 shows the aerosol spectrum divided into regions based on typical mass distribution and Table 2-1 shows aerosols classifications based on the mentioned types.
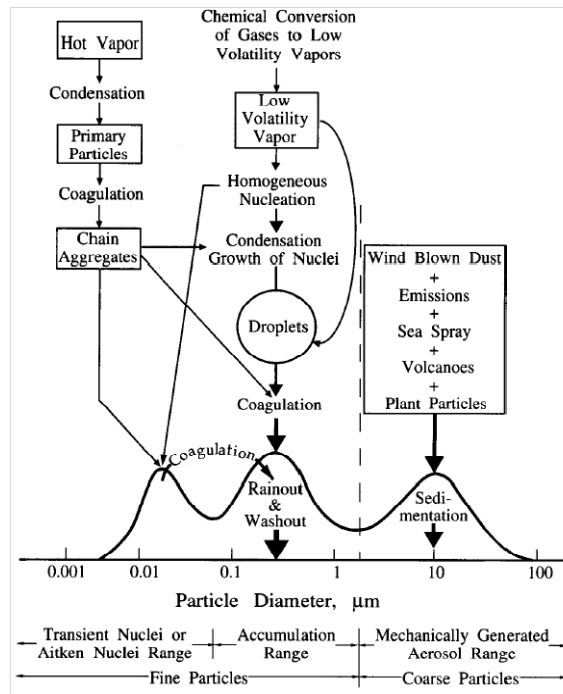
Figure 2-5 Aerosol size classification {source: [5]}.

Small sizes particles make them very mobile resulting in a rapid coagulation which together with condensation of low volatility vapor result in the formation of large particles eventually ending up in the *Accumulation or Coarse mode* [15]. The particles are too small to undergo any effective sedimentation and too big for coagulation *Aitken* mode particles. The decomposition processes for the *Accumulation mode* are rainout. Rainout is the most efficient mode to remove smaller particles which are removed by incorporation into cloud droplets. The larger particle in the *accumulation mode* can be tapped by falling rain drops and removed from the atmosphere in that case called washout.

Aerosol Classification				
Type	**Class**	**Mode**	**Formation Mechanism**	**Size**
I	Nucleation	Aitken	Gas-to-particle conversion	0.001-0.1 µm
II	Large	Accumulation	Coagulation/Heterogeneous	0.1-2.5 µm
III	Giant	Coarse	Mechanical process	$> 2.5\mu m$

Table 2-1 Particle types classified according to radius and formation mechanism {source: [14]}.

2.4.2 Aerosols interactions with weather and clouds

An important issue in the Global Weather Change (GWC) is the study of biochemical cycle of tropospheric aerosol, and the generation of it from the surface, the uplift, and transportation into different atmospheric layers and the interaction with the Atmosphere [16, 17]. The aerosols cause direct and indirect impact on different climate process. The direct impact is produced through the diffusion and absorption of solar radiation. This direct impact has an important consequence on the Earth's temperature, leading to cooling caused by sulfuric aerosols or warming caused by carbonaceous aerosols [18]. The indirect impact has an important role in cloud formation, by forming cloud condensation nuclei (CCN). Aerosols in the CCN affect the microphysical properties of clouds, and ultimately, clouds will be affecting the Earth's radiation budget [16]. The indirect impact of aerosols affects the different cloud properties, for instance: brighter clouds can reflect more solar radiation. The precipitation is affected also by increasing the number of droplets in warm clouds [18, 19]. Another important issue to be considered is the semi-indirect effect occasioned by aerosols in

their capacity to absorb the solar radiation causing local heating which will evaporate the surrounding clouds [19].

Aerosols have different physical and optical properties that depend on their composition and size. Condensation of WV upon aerosols affects the aerosols size, shape, composition, and modifies their optical properties affecting the direct radiative forcing. There are different groups of scientific that are opposed in the explication of the aerosol contribution with the GW issue. One group said: "The ASD is space and time dependent (with short atmospheric lifetime) and cannot be considered responsible for long-term effects such as the GW" [16, 17]. The reason is if the aerosols play an important role in the Earth radiation budget because there are particles that absorb and scatter, affecting this natural energy balance and having negative impact on climate and in the GW issue.

Cirrus clouds are composed of water or ice particles suspended in the atmosphere. "These clouds are formed by the air that contains water vapor, which is cooled by cold air and condenses into droplets on *condensation nuclei* or ice crystal particles. The air is cooled by expansion during the upward convection resulting from intense solar heating of the ground, or by a cold front system near the ground causing a mass of warm air to be forced aloft. Orographic movements are responsible in the formation of clouds causing air oscillations as it moves downstream mixing the warmer and cooler air currents, caused by the mountains" [20].

High clouds are present in altitudes between 6km and 14km, and can be cirrus, cirrostratus, and cirrocumulus. Intermediate clouds are between 2km-6km, and can be cumulus, altostratus and altocumulus; and low clouds are in altitudes less than 2km, they can

be stratus, nimbostratus, and stratocumulus. Finally, clouds with vertical development are in altitudes between 0.5km and 6km and are called cumulonimbus [21]. Cirrus clouds increase the Earth's *albedo* and at the same time absorb the infrared radiation that is emitted to the space by the Earth. Warming or cooling effects are both possible and are dependent on cloud location, composition and structure. Greenhouse gases have a weak effect on low altitude clouds, so their *albedo* (index of reflection) effect dominates occasioning a net cooling effect on the climate [22].

The atmosphere and the Earth's surface absorb and reflect the solar energy, creating a heat balance. Clouds have an important role in this energy balance [22]. Clouds reflect the sunlight backward to the space, reducing the solar energy in the Earth surface (Albedo effect). Also, the clouds decrease heat radiating to the space as it absorbs solar energy (greenhouse effect). These two effects depend on the cloud structure, cloud particles, cloud optical depth, and other cloud properties.

Several publications classify the cloud formations as:

- Low altitude clouds, these types are located in the first 800m above the sea level, are generally due to air mass intrusions from the PBL in summer or in dry seasons, orographic air mass movements, flying snow crystals, haze, fog, and etc. [23- 25].

- Middle tropospheric cirrus, this type is located between 4.5 and 9km and are a family of cirrus having various geometrical depths from thin contrails of 100 to 750m up to thick cirrus close to 2km which may be caused by the PBL to Free troposphere (>3km) air mass exchanges, from long range transport, vertical dynamics or aviation traffic [23- 25].

22

- Tropopause cirrus clouds are often observed and easily identified as they have their top always trapped at the bottom of the tropopause (above 12km). The geometrical thickness may vary from a thickness 100m to 4km with differing consistencies, ranging from very dense and compact, to diffuse with large air pockets [23- 25].

2.5 Water Vapor Mixing Ratio (q_{H2O})

Water vapor (WV) is one of the most important greenhouse gases and an agent of the hydrological cycle which makes it vital for global climate model calculations and weather predictions [25-29]. The water is the main method of transportation of matter and energy for particles of different sizes, shapes and types, as well as the universal solvent that can be mixed easily with other particles to form new types that have a negative impact in the atmospheric process [26].

2.5.1 Water Vapor (WV) Measurements

Several different methods exist to measure the WV in the troposphere region. AERONET reports the WV coefficient, but of the whole atmospheric column. GPS systems, based on the delays occasioned by the atmospheric WV on the paths between the antennas of the receiver and the satellite of the GPS network, can be used to estimate WV of the total column [30-33]. Inexpensive *in situ* sensors provide reasonable WV measurements but not as a function of height. Microwave instruments are also utilized for the estimation of H_2O

and humidity, but are only designed for the Stratosphere and Mesosphere [26]. Satellite sensors are most widely used method which provide excellent global coverage of WV distributions, but encounter difficulties in the presence of clouds. *Radiosonds* are effective in providing WV measurements in terms of height, but are susceptible to wind changes. High spatial and temporal resolutions of the q_{H2O} profiles are possible with the Raman-Lidar techniques [27, 28].

The 27 – 37% of the atmospheric radiation absorption is caused by the WV content in the middle and upper tropospheric region [29-31]. This effect is due to the strong absorption in the infrared region of the spectral band [32]. The WV measurements are needed to investigate the tropopause phenomena, vertical troposphere and stratosphere exchanges, CCN processes, cloud formation, lower stratosphere WV concentrations, and other important issues. The WV data is necessary for initializing the NWP (Numerical Weather Prediction) and global climate models [33].

2.6 Scattering Theory

The atmospheric scattering can be obtained by two methods; The Elastic and Inelastic backscatter (Fig. 2-6). The followings sub-sections show the most important theory about the different scattering for atmospheric studies based on Lidar systems.
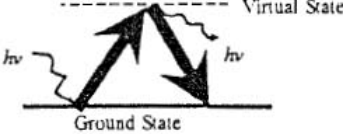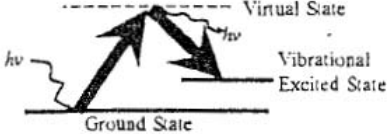
Lidar Technique	Schematic and Physical Description
Rayleigh Scattering/ Mie Scatering (Particles)	Elastic Scattering : laser radiation scattered from atoms, molecules, or particles with no change of frequency.
Raman Scattering	Inelastic Scattering : laser radiation scattered from molecules with a frequency shift characteristic of the molecule.

Figure 2-6 Elastic and Inelastic scattering used in most Lidar technique {source: [15]}.

2.6.1 Elastic Scattering

The Elastic-backscatter detects the total atmospheric backscatter without separation of particle and molecular contributions to the backscattered signal. There are two types of Elastic-backscatter that can separate the particles and molecules of the backscatter signal. The elastic-backscatter is present when the transmitted and the received wavelengths are the same. Fig. 2-7 shows a summary of this type of scattering, explaining the Rayleigh and Mie scattering.

25
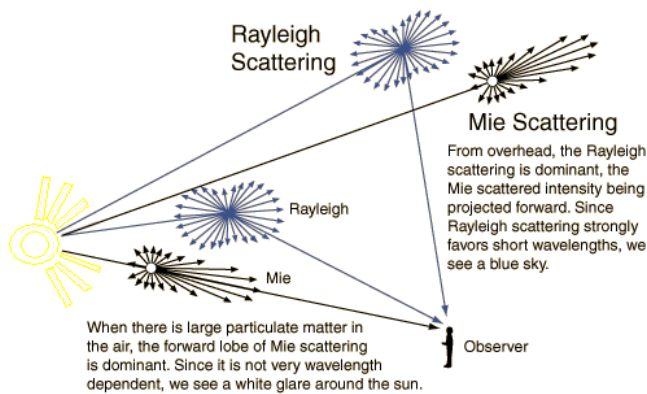
Figure 2-7 Rayleigh and Mie Scattering concept {source: [34]}.

2.6.1.1 Rayleigh scattering (Molecules)

Rayleigh scattering is for clean atmosphere (molecules only, for example ozone and oxygen) and is the light scattering by particles much smaller than the wavelength of the light. In some occasions it occurs when the light travels in clear solids and liquids molecules, but is more common in gasses [15]. Scattering of sunlight in clear atmosphere is the reason of the blue color in the sky. This color is caused by the scattering of molecules in the atmosphere, and is more effective at short wavelengths where blue end in the visible spectrum (Fig. 2-8).
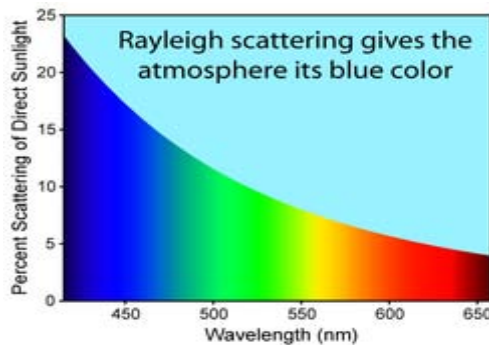
Figure 2-8 Visible Spectrum {adapted from [17]}.

2.6.1.2 Mie scattering

Mie scattering is referred to spherical particles or aerosols, where the radiation is reflected in all directions. The particles and aerosol which scatter light in all directions are from anthropogenic and natural sources. This type of scattering occurs when a light beam is scattered by particles or aerosols that corresponds at the same frequency of the transmitted light beam. The difference between this type and Rayleigh is that this type of scattering is applied for larger matter presented in the atmosphere considered particles or aerosols meanwhile Rayleigh is considered for molecules.

2.6.2 Inelastic scattering

The Inelastic-backscatter is present when the wavelengths of the transmitted light beam and the returned light beam are different. Aerosols, particles, and molecules cause a shift in the wavelength of the radiant energy, very common in molecules.

2.6.2.1 Raman scattering

Raman shift occurs when a beam of light is scattered by molecules at wavelengths that correspond to energy differences associated with the vibrational and rotational energy states of molecules [15]. This shift in frequency of the scatters photon is due to the energy that characteristic of the vibrational and rotational energy states of each molecule. If the resulting radiation has a longer wavelength, or lower frequency, the molecule has gained energy, and the red-shifted scattered radiation is referred to as the Strokes components. If the molecules loses energy, the scattered radiation is blue shifted and is referred to as the anti-Strokes components [5,15]. In the Strokes case, the energy shift is given by $E+\Delta E = hc/\lambda$,

meanwhile in the anti-Strokes case the energy is given by E-ΔE =hc/λ, where E is energy, c is the light velocity, h is Plank's constant, and λ is the wavelength.

The Raman spectrum consists of scattered radiation at wavelengths corresponding to the energies of molecule's vibrational stated and rotational states. Typically, Raman Lidar measurements of an atmospheric species are made as a ratio of signals of specific molecules to a signal that represents the total density, for example: N_2 and O_2. This ratio provides a direct a measure of the relative concentration of the species and removes much uncertainty by canceling the effect of many system parameters [5, 15].

2.7   USA Atmospheric Standard Assumptions 1976 (ASA76)

A hypothetical vertical distribution of atmospheric temperature, pressure, and density are needed to be representatives of the atmosphere for purposes of α_{mol} (molecular extinction) and β_{mol} (molecular backscatter) performance calculations [8]. The α_{mol} and β_{mol} coefficients depend of the atmospheric parameters of temperature, pressure, and density profiles. The temperature profile can be determined using a linear equation that depends of range (altitude). Eq. 2.3 shows the linear equation for temperature simulation.

$$T(R) = T(0) - 6.5 \times R \qquad 2.3$$

Where, the units of 6.5 are Kelvin/km, $T(0)$ is the surface temperature in Kelvin, and R is the range in km. The pressure profile is calculated using an exponential equation that depends of range, and is measured in Pa (Pascals).

$$P(R) = P(0)e^{-R/r_p} \qquad 2.4$$

Where, r_p=7.8km and $P(0)$ is the surface pressure in Pa. The density coefficient is also known as number density and depends of temperature, pressure, and the Boltzmann's constant. Density is measured in g/m^2 (grams per square meters) or in m^{-3}.

$$N(R) = \frac{P(R)}{kT(R)} \qquad 2.5$$

Where, k is the Boltzmann's constant and is equal to 1.380622×10^{-23} N*m/Kelvin. Fig. 2-9 shows the results based the ASA76 for temperature, pressure, and number density.
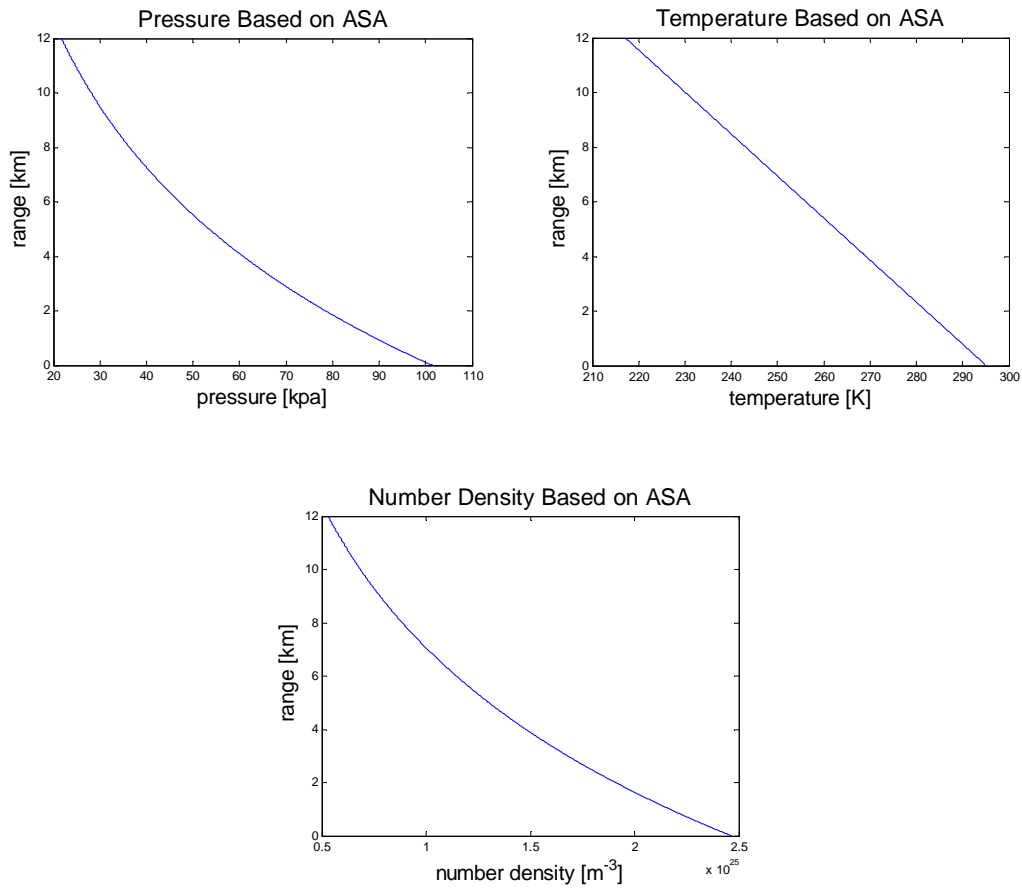
Figure 2-9 Results of ASA76 for temperature, pressure, and number density.

2.7.1 Molecular Extinction (α_{mol}) and Backscatter (β_{mol}) Coefficients

α_{mol} is determinate using the ASA76 for density, and is given by eq. 2.6 where the units are in m^{-1}.

$$\alpha_{mol}(\lambda, R) = e^{-\sigma_{Ray}(\lambda)\int_0^r N(r)dr}$$

2.6

Where, $\sigma_{Ray}(\lambda)$ is the cross-sectional area and depends of the wavelength. The following equation represent the cross-sectional area which depend on the following two constants $\gamma = 0.0279$ and $N_s = 2.547 \times 10^{25} m^{-3}$.

$$\sigma_{Ray}(\lambda) = \frac{8\pi^3 (n(\lambda)^2 - 1)^2}{3\lambda^4 N_s^2} * \left(\frac{6 + 3\gamma}{6 - 7\gamma}\right)$$

2.7

β_{mol} can be obtained using the molecular extinction-to-backscatter ratio or molecular lidar ratio (L_{mol}), which is given by eqs.2.8 & 2.9.

$$L_{mol} = \frac{\alpha_{mol}(R)}{\beta_{mol}(R)} = \frac{8\pi}{3} sr$$

2.8

$$\beta_{mol}(R) = \frac{3 \cdot \alpha_{mol}(R)}{8\pi}$$

2.9

Based on ASA76, α_{mol} and β_{mol} coefficients are calculated (Fig.2-10). This calculation represents the Rayleigh scattering for natural molecules or clear atmosphere conditions.
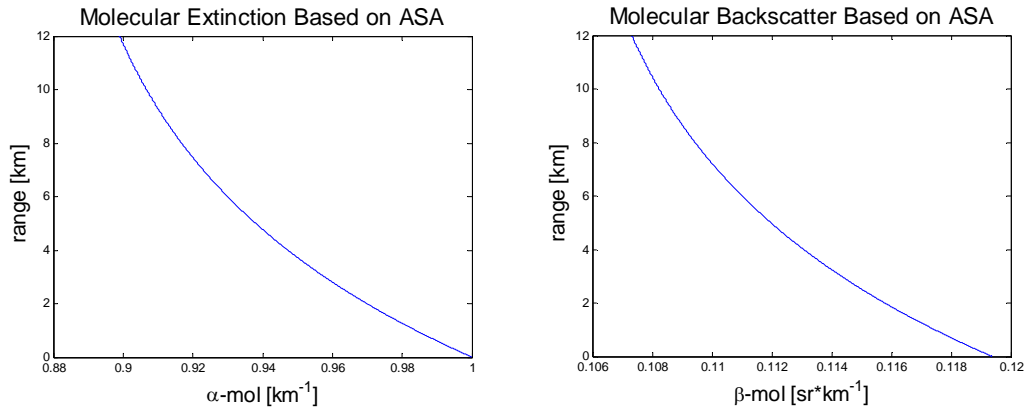
Figure 2-10 Molecular extinction and backscatter coefficient based on ASA76.

2.8 Conclusion

Based on the presented literature, Lidar systems have advancement over traditional radar systems to make remote sensing. Lidar systems have good spatial, temporal and vertical resolution to study different aerosols or particles properties scanning an atmospheric region. There are different types of Lidar systems that depend on the different scattering types (Rayleigh, Mie, and Raman). The number of parameters and particles studied by the Lidar system also depend of the scattering type. ASA76 is very important to determine the Rayleigh scattering, which is fundamental to determine the molecular parameters that are in nature form in the atmosphere, which are fundamental to continue with the aerosol characterization.

3 Lidar Technique Theory

This Chapter present the mathematical concepts needed to proceed with the aerosol characterization based on Lidar systems. The inversion methods used to determine the different parameters are presented with details and some enhancements on these are include in the developed mathematical methodology based in the fundamental equations presented in previous publications and works. These equations are implemented in algorithms to proceed with the Lidar signal processing for aerosol characterization.

3.1 Lidar Technique and Atmospheric Interaction Processes

The description of the laser beam interaction with atmospheric constituents (molecule, particles or aerosols, clouds, etc.) is based on the fundamental theory of electromagnetic wave propagation. The atmosphere contains a wide range of constituent extending from atoms and molecules, to aerosols, clouds water droplets, and ice crystals.

Mixtures of these components results in a series of complex atmospheric interaction that take place with the laser beam. The intensity of the light resulting from these processes is proportional with the initial intensity I_0, the number density of the active diffusers n, and the differential cross-section σ. If the laser beam is directed to the atmosphere, different processes may take place with different probabilities determined by their correspondent cross-sections. The interaction may lead to elastic (Rayleigh and Mie) and inelastic (Raman)

scattering (discussed in section 2.5), absorption, reflection and diffraction. Based on these processes, various spectroscopic and non-spectroscopic measurements techniques have been developed for monitoring the atmosphere [36]. The interactions may be non-selective, like Rayleigh, Mie or Raman scattering, and more or less important depending on the atmospheric composition. Absorption is a selective process, and depends of the absorption cross section of the laser wavelength. The resonant processes (Rayleigh or Raman) are also selective, meaning that the laser wavelength radiation matches with the specific electronic transitions of molecules.

Two important microscopic scattering properties are the β_{aer} (aerosol backscatter) and α_{aer} (aerosol extinction) coefficients that are used to express atmospheric aerosol interactions, where the dimensionless size parameter, χ, is given by eq. 3.1 and is used in this research to determine the refractive index, m.

$$\chi = \frac{2\pi r\, m}{\lambda} \qquad 3.1$$

Where, r is the radius and is the geometric dimension of the diffuser, m is the refractive index which is compose of n+i*k, and are wavelength depended. The real and the complex part of m provide information about non-absorbing and absorbing aerosol capacity. For $\chi \ll 1$, Rayleigh or molecular scattering prevails, $\chi \sim 1$ Mie-aerosol scattering begins to increase in importance, and for $\chi \gg 1$, scattering is purely geometric reflection by clouds [36].

The molecular and aerosol elastic and inelastic processes involved in the Lidar system detection are the following [36]: The Lidar constituent detection is the following: For molecules (N_2, O_2), the detection for elastic light scattering is for $\lambda \gg r$ (λ is the transmitter wavelength, and r is the molecular radius), the aerosol elastic scattering is for $\lambda \sim r$ (λ is the

33

transmitter wavelength, and r is the aerosol radius), the inelastic molecular scattering for N_2, O_2, and H_2O is for $\lambda >> r$, and the cloud elastic and inelastic scattering is for $\lambda << r$ (r is the droplet/ice crystal geometrical radius).

The principal parameters determinate by Rayleigh scattering are discussed in section 2.6 which are β_{mol} and α_{mol} coefficients estimated using ASA76. These parameters are important to simulate the atmosphere only with the presence of molecules, and are used to simplify the solution of Mie and Raman-parameters such as β_{aer} and α_{aer} coefficients [37].

3.2 Elastic Lidar Technique

The Lidar equation is the fundamental tool to extract the desired information of the scattered light collected by the telescope. In this equation the received energy is related to the emitted energy through the properties of scattering volume and the beam path. The Lidar equation for the elastic return signal due for molecules and particles (aerosols) is given by eq. 3.2 [10].

$$P(R) = \frac{E_0 \eta_0}{R^2} O(R) \beta(R) Exp\left[-2\int_0^R \alpha(r)dr \right] \quad 3.2$$

Where, P(R) is the received power at distance R, R is the altitude of the volume element where the return signal is scattered, E_0 is the transmitted power, η_0 are the efficiencies of the optical and detection units, O(R) is the overlap between the outgoing laser beam and the receiver FOV, $\beta(R)$ is the total backscatter coefficient, and $\alpha(R)$ is the total extinction coefficient. The term R^2 is inserted in the denominator in order to correct the decreasing

34

scattering cone seen by the telescope as the scattering altitude increases the square of the altitudes. The exponential decay is called the two-way transmittance, and is expressed in terms of α coefficient and is integrated twice over the interval from the station altitude to the scattering altitude. The parameters in the equation containing the information about the atmosphere are α and β coefficients. The α coefficient described the extent light emitted by the laser, and the lost on its way up to the scattering object and back down to the telescope. This loss is due to scattering in other directions than the 180 degrees of backscattering direction and to any possible absorption. The differential β coefficient gives the relation between the amount of scattered light in the direction of interest and the incident light. Both, α and β coefficients can be separated into a molecular (α_{mol} and β_{mol}) and particulate (aerosol) contribution (α_{aer} and β_{aer}).

In the experimental received signal there is present a constant, known as background noise. The sources of background are mainly ambient light, especially during daytime, and photomultiplier dark current. If the lengths of the measurements are chosen long, so that the end of it corresponds to altitudes where the laser light has become totally attenuated, any signal represents the background noise. The background noise, N(R), has been added in eq. 3.3, because it represents the first 1-4 km (typically 3km) of the received power.

$$P(R) = \frac{E_0 \eta_0}{R^2} O(R)\beta(R)Exp\left[-2\int_0^R \alpha(r)dr\right] + N(R) \qquad 3.3$$

Taking the average of the receive signal (eq. 3.2) in the first 3km region helps to determinate the background noise. The background contribution can be conveniently removed or done subtracting the full power profile signal with the calculated average value. Since the

35

background generally fluctuates the removal should be done separately for each profile in a set of several consecutive collected profiles. An alternative method for background subtraction is to measure the signal without laser light before and/or after the Lidar measurements. But, this method is not recommended because the sunlight intensity is time varying. The background noise is given by:

$$N(R) = \frac{1}{R} \sum_{i=R-\frac{\Delta Br}{\Delta r}}^{\Delta Br} P(R_i)$$

3.4

Where, Δr is the Lidar vertical resolution in km, ΔBr is the signal altitude for calculating the background noise in km (3km), and R is the range in km.

The most wanted quantities in the Lidar equation (eq. 3.2) are α and β coefficients. They can be solved into their molecular and aerosol origin, respectively, and treated as arising from two different independent scattering contributions, the total β and α coefficients are given by eq. 3.5 & 3.6 [10]. The molecular terms for both coefficients are calculated based on ASA76, presented in section 2.6.

$$\beta(R) = \beta_{aer}(R) + \beta_{mol}(R)$$

3.5

$$\alpha(R) = \alpha_{aer}(R) + \alpha_{mol}(R)$$

3.6

To retrieve profiles of α and β coefficients probably the most widely used strategy for the Lidar equation inversion is to define some analytical relationship between α and β. The Lidar stable solution, when the aerosol scattering contribution dominated, was formulated by Klett [37]. Later, Fernald reformulated the solution for the two atmospheric components case and hence the general form which has gained widespread today [38].

The determination of β_{aer} and α_{aer} are more complex, but as discussed above α and β can be resolved into a molecular and aerosol component. The theoretical value for molecular Lidar ratio ($L_{mol}=\alpha_{mol}/\beta_{mol}$) is equal to $8\pi/3sr$ in the 180° backscattering direction calculated from Rayleigh theory, under the condition of zero molecular absorption. The particulate equivalence is called the aerosol extinction-to-backscatter ratio or aerosol Lidar ratio, $L_{aer}=\alpha_{aer}/\beta_{aer}$. L_{aer} is assumed constant based on Klett methodology. With this assumption the extinction and backscatter components can be determined directly from eq. 3.2, but this equation needs to be range adjusted or corrected to normalize the received signal. Eq. 3.7 show the range adjusted equation, where eq. 3.2 is multiplied by the square range (R^2), and $\beta(R)$ and $\alpha(R)$ are substituting by eq. 3.5 & 3.6.

$$S(R) = E_0\eta_0[\beta_{aer}(R) + \beta_{mol}(R)]Exp\left[-2\int_0^R [\alpha_{aer}(R) + \alpha_{mol}(R)]dr\right] \quad 3.7$$

To facilitate the determination of $\beta_{aer}(R)$ and $\alpha_{aer}(R)$, is introduced an equation the terms of $Y(R)$ which is expressed as a function of $\alpha_{aer}(R)$ using the L_{aer} ratio.

$$Y(R) = L_{aer}[\beta_{aer}(R) + \beta_{mol}(R)] \quad 3.8$$

Then, eq. 3.8 is substituting in the normalized Lidar equation and is given by:

$$S(R)L_{aer}Exp\left[-2[L_{aer} - L_{mol}]\int_0^R \beta_{mol}(R)dr\right] = E_0\eta_0Y(R)Exp\left[-2\int_0^R Y(R)dr\right] \quad 3.9$$

Now, proceed to organize eq. 3.9, regrouping the constants L_{aer} and L_{mol} and substituting $Y(R)$, obtaining the equation of the following form:

$$S(R)L_{aer}Exp\left[-2[L_{aer} - L_{mol}]\int_0^R \beta_{mol}(r)dr\right] = E_0\eta_0Y(R)Exp\left[-2[L_{aer}]\int_0^R \beta_{aer}(r) + \beta_{mol}(r)dr\right] \quad 3.10$$

Then, applying logarithm in both sides of eq. 3.10 and differentiating with respect R, the new equation is given by:

$$\frac{d\left\{S(R)L_{aer}Exp\left[-2[L_{aer}-L_{mol}]\int_0^R \beta_{mol}(r)dr\right]\right\}}{dR} = \frac{1}{[\beta_{aer}(R)+\beta_{mol}(R)]}\frac{d[\beta_{aer}(R)+\beta_{mol}(R)]}{dR} - 2[L_{aer}(\beta_{aer}(R)+\beta_{mol}(R))] \quad 3.11$$

Eq. 3.11 can be solved using the Bernoulli methodology for boundary conditions. The Bernoulli equation is given by eq. 3.12, where R_0 is a reference altitude.

$$Y(R_0) = L_{aer}[\beta_{aer}(R_0) + \beta_{mol}(R_0)] \quad 3.12$$

Then, the total β solution is given by eq. 3.13, see Appendix A for more details about this mathematical concept presented above to obtain this solution:

$$\beta_{aer}(R) + \beta_{mol}(R) = \frac{S(R)Exp\left[-2[L_{aer}-L_{mol}]\int_{R_0}^R \beta_{mol}(r)dr\right]}{\frac{S(R_0)}{\beta_{aer}(R_0)+\beta_{mol}(R_0)} - 2L_{aer}\int_{R_0}^R S(r)Exp\left[(L_{aer}-L_{mol})\int_{R_0}^r \beta_{mol}(z)dz\right]dr} \quad 3.13$$

Finally, α is determinate using the assumed or estimated L_{aer} and is given by eq. 3.14 [11, 12].

$$\alpha_{aer}(R) = L_{aer} \cdot \beta_{aer}(R) \quad 3.14$$

In eq. 3.13, the calibration altitude R_0 somewhere within the range interval is chosen at which the β coefficient is known or assumed. The choice of R_0 at the upper end of the integration interval together with downward integration, responsible for the notation far-end (boundary point) solution, has shown to give a more stable inversion, at least in turbid atmospheres [38]. Furthermore, with this strategy of choose R_0 high enough that aerosols contribution to the backscatter can be considered small and approximated to zero. In this case R_0 coincides with the upper starting altitude where β_{aer} is zero in the first step of the

integration, and left to define before the integration can start at L_{aer}. For aerosols, the relation between β and α depends on the aerosol microphysics (refractive index, shape, and size distribution). In real atmospheres, both β_{aer} and α_{aer} may vary over a wide range, while the L_{aer} varies over a much smaller range, most typically by a factor of 50 to 60 (clouds excluded), and the variations are in addition smooth. The L_{aer} constant assumption is a reasonable good approximation in well mixed region of the atmosphere. The choice of an appropriate value for L_{aer} has been widely discussed and depends on the atmospheric nature question. Actually has been presented values from a wide range of measurements, ranging from 10 up to almost 80sr [39]. However, the importance of the start value decreases with increasing aerosol load and on the limit of the single-component case of Klett no aerosol, L_{aer} is needed [38]. The Klett algorithm is the best suited in cases of high extinction, such as dense or clouds, whereas the Fernald algorithm is better suited for thinner clouds [37, 38].

3.3   Inelastic Lidar Technique

The basic theory used to determine α_{aer} and β_{aer} from the elastic backscatter signals is the Klett inversion method [37]. This procedure, with all its subsequent modifications and improvements, suffers from the fact that two physical quantities, α_{aer} and β_{aer} coefficients, must be determinate from one measured Lidar signal. This is not possible without assumptions about the relation between α_{aer} and β_{aer}, and estimate of a boundary or reference value of the β_{aer}. These data are usually hard to assesses and cause large uncertainties in the

39

α_{aer} coefficients that are determinate. The inelastic (Raman) backscatter signal or the Lidar system is affected by α_{aer} but not by β_{aer} [4]. Therefore, analysis of Raman Lidar technique applied to β_{aer}, visual range, and optical depth, but until now a general formalism for determining range-resolved α_{aer} coefficients from Raman Lidar signals has not given [40].

Let the Raman Lidar equation given by eq 3.15 [4].

$$P(R,\lambda_0,\lambda_R) = \frac{E_0\eta_0}{R^2}O(R)\beta(R,\lambda_0,\lambda_R)Exp\left[-2\int_0^R[\alpha(r,\lambda_0)+\alpha(r,\lambda_R)]dr\right] \quad 3.15$$

Where, P is the received power from distance R at the Raman wavelength λ_R if the laser pulse is transmitted at λ_0, R represents the altitude or range, O(R) is the overlap function between the laser beam and the telescope FOV, α is the depth-depended total extinction coefficient at wavelengths λ_0 and λ_R, and β contains all dept- independent parameters. The backscatter coefficients, β, is linked to the differential Raman backscatter cross section $\left(\dfrac{d\sigma}{d\Omega}\right)$ of a gas molecule number density (N) by the relation in the following equation:

$$\beta(R,\lambda_0,\lambda_R) = N(R)\frac{d\sigma(\lambda_0,\lambda_R,\pi)}{d\Omega} \quad 3.16$$

The profiles of both nitrogen and oxygen can be used since their number densities are well known. With $P(R)=P(R,\lambda_0,\lambda_R)$, it follows:

$$\alpha(\lambda_0,R)+\alpha(\lambda_R,R) = \frac{d}{dR}\left[\ln\frac{O(R)N(R)}{R^2P(R)}\right] \quad 3.17$$

Where, O(R) is equal to unity if the path of the transmitted laser beam is entirely within the FOV of the receiver, which is the case above a certain minimum height R_{min}. The two α coefficients may be written as:

$$\alpha(\lambda_{0,R}, R) = \alpha_{mol}(\lambda_{0,R}, R) + \alpha_{aer}(\lambda_{0,R}, R) \quad 3.18$$

Where, α_{mol} and α_{aer} are the extinction coefficients due to absorption and Rayleigh scattering by atmospheric gases, and aerosol scattering and absorption, respectively.

$$\alpha_{aer}(\lambda_0, R) + \alpha_{aer}(\lambda_R, R) = \frac{d}{dR}\left[\ln\frac{N(R)}{R^2 P(R)}\right] - \alpha_{mol}(\lambda_0, R) + \alpha_{mol}(\lambda_R, R) \quad 3.19$$

Assuming a wavelength dependence of the aerosol extinction such as:

$$\frac{\alpha_{aer}(\lambda_0, R)}{\alpha_{aer}(\lambda_R, R)} = \frac{\lambda_R}{\lambda_0} \quad 3.20$$

Combining eq. 3.19 & 3.20, the unknown extinction coefficient profile is given by:

$$\alpha_{aer}(\lambda_0, R) = \frac{\frac{d}{dR}\left[\ln\frac{N(R)}{R^2 P(R)}\right] - \alpha_{mol}(\lambda_0, R) + \alpha_{mol}(\lambda_R, R)}{1 + \frac{\lambda_R}{\lambda_0}} \quad 3.21$$

This result holds for altitudes $R > R_{min}$ for which the Raman Lidar overlap function $O(R) \equiv 1$.

For an estimate of $\frac{d}{dR}\left[\ln N(R)\right]$ and $\alpha_{mol}(\lambda_{0,R}, R)$, the air density profile must be known. Height profiles of the atmospheric density can be assessed by available ASA76 (see section 2.6) with measured values of the ground temperature and pressure, or they can be directly measured with *radiosound*. Light extinction by ozone can also be taken into account.

The β_{aer} coefficients, $\beta(R, \lambda_0)$, now explicitly written as a function of the laser wavelength λ_0, can be determined using the total (molecular + aerosol) and pure β_{mol} signals. Two measured signals pairs $P(R, \lambda_0)$ and $P(R, \lambda_R)$ at R and R_0 are needed. From two Lidar $P(R, \lambda_0)$ and $P(R_0, \lambda_0)$ from total β (eq. 3.5) and two more Lidar signals $P(R, \lambda_R)$ and $P(R_0,$

λ_R) from β_{mol} alone, a solution for the β coefficient ($\beta(R,\lambda_0)$) is obtained by forming the ratio in eq. 3.22 [41].

$$\frac{P(R_0, \lambda_R)P(R, \lambda_0)}{P(R_0, \lambda_0)P(R, \lambda_R)} \qquad 3.22$$

Then, inserting the perspective Lidar equations for the four signals, and rearranging the resulting equation, the solution is given by the following equation:

$$\beta_{aer}(R, \lambda_0) + \beta_{mol}(R, \lambda_0) = [\beta_{aer}(R_0, \lambda_0) + \beta_{mol}(R_0, \lambda_0)]\frac{P(R_0, \lambda_R)P(R, \lambda_0)N_R(R)}{P(R_0, \lambda_0)P(R, \lambda_R)N_R(R_0)}$$

$$\times \frac{\exp\left\{-\int\limits_{R_0}^{R}[\alpha_{aer}(r, \lambda_R) + \alpha_{mol}(r, \lambda_R)]dr\right\}}{\exp\left\{-\int\limits_{R_0}^{R}[\alpha_{aer}(r, \lambda_0) + \alpha_{mol}(r, \lambda_0)]dr\right\}} \qquad 3.23$$

If the two signal channels are properly aligned so that $O(R,\lambda_R) = O(R,\lambda_0)$, then overlap effects cancel out because the backscatter profile is determined from the signal ratio profile $\frac{P(R, \lambda_0)}{P(R, \lambda_R)}$.

As is the Klett procedure, a reference value for aerosol backscattering at R_0 must be estimated. To reduce the effect of the uncertainty in this estimate on the solution, it is recommended to choose the reference height in the upper troposphere where aerosol scattering is typically negligible compared to Rayleigh scattering [37]. Then only the air density, the β_{mol}, and atmosphere extinction properties must be assumed to solve eq. 3.23. Again, meteorological profiles or ASA76 data are used to calculate air density and β_{mol} terms. The aerosol transmission ratio for the height range between R_0 and R is estimated

from the measured α_{aer} profile with the assumption on the wavelength dependence as used to determine the L_{aer} profile presented by eq. 3.24.

$$L_{aer}(R) = \frac{\alpha_{aer}(R, \lambda_0)}{\beta_{aer}(R, \lambda_0)} \quad 3.24$$

3.4 Aerosol Optical Depth (AOD)

The optical depth is a measure of transparency, and is defined as the negative Logarithmic of the fraction of light that is absorbed on a path [10].

$$AOD = \int_{R_{min}}^{R} \alpha_{aer}(r)dr \quad 3.25$$

Where $\alpha_{aer}(r)$ is the aerosol extinction coefficient. The AOD is present in the receive power equation, inside of the exponential part. The AOD can be obtained using a Sun-photometer and AERONET. If the AOD is obtained from one of the mentioned source, it can be substitute in eq. 3.2 and obtain the following equation:

$$P(R) = \frac{E_0\eta_0}{R^2} O(R)\beta(R)Exp\left\{-2\left[AOD + \int_0^R \alpha_{mol}(r)dr\right]\right\} \quad 3.26$$

Using the equation above, the β_{aer} can be obtained without problem. Note: the AOD is also known as Aerosol Optical Thickness (AOT).

3.5 Angstrom (Å) Coefficient and Dependency Law

Å coefficient describes the reliance of aerosol optical depth on wavelength. If the vertical stratified structures were cloud particles, the Å coefficient would be nearly close to cero and independent of the cloud optical depth since clouds are always made up of large particles modes. On the other hand, smoke plumes can be made of very small absorbing particles, which would have a high angstrom coefficient [42, 43].

$$angstrom = \frac{\ln\left(\frac{\beta_{aer}\lambda_2}{\beta_{aer}\lambda_1}\right)}{\ln\left(\frac{\lambda_1}{\lambda_2}\right)} \qquad 3.27$$

Where, β_{aer} is the aerosol backscatter coefficient at the respective wavelength. The Å coefficient can be determined also using the extinction coefficient at two different wavelengths.

The Å dependency law is a useful tool in the moment to estimate the desired parameter at other wavelengths. This law is presented in eq. 3.28 and is the same that eq. 3.27. The Å dependency law is used to calculate a known parameter at other wavelength.

$$\frac{xparameter}{yparameter} = \left(\frac{x\lambda}{y\lambda}\right)^{\text{Å}} \qquad 3.28$$

3.6   Aerosol Microphysical Properties

The range of the ASD for atmospheric aerosols varies from 0.05nm to 10µm radius. The aerosols studied in this research has been assumed spherical, this assumption has based on Mie theory to determine the efficiencies for α and β coefficients.

3.6.1 Aerosol Size Distribution (ASD)

The relation between α_{aer} and β_{aer} coefficient with the size distribution of spherical particles can be obtained by eq. 3.29, known as Fredholm equation [10].

$$g_p = \int_{r\,min}^{r\,max} k_p(r,m)v(r)dr + e_p^{exp} \qquad 3.29$$

Where, g_p represent the optical data such as α_{aer} or β_{aer}, the subscript p being the number of available optical coefficient at the specific range and wavelength. V(r) represents the volume size distribution. k_p is the volume kernel function for the specific data type and depends on the Mie-efficiencies for spherical particles, the refractive index m, and the radius r [10] (see appendix B, eq. B.5).   m is the refractive index and is a complex number, where the imaginary part represents absorption. e_p^{exp} is the equivalent experimental error at the specific optical data.

Volume size distribution $v(r)$ in eq. 3.29 is typically modeled by logarithmic normal or binomial density function which itself is approximated by a linear combination of B-spline functions $B_j(r)$, of the first type (see Appendix C), Eq. 3.30, where w_j [10] are the coefficients, and e^{math} is the mathematical error due to the approximation

45

$$v(r) = \sum_j w_j B_j(r) + e^{math}(r) \qquad\qquad 3.30$$

By substituting eq. 4.30 into eq. 4.29, swapping the integration and summation eq. 3.31 is formed as follow:

$$g_p = \sum_j w_j \int_{r\min}^{r\max} k_p(r,m)v(r)dr + e_p^{\exp} \qquad\qquad 3.31$$

The integral inside of 3.31 represents the weight matrix and is known as A_{pj}.

$$A_{pj}(m) = \int_{r\min}^{r\max} k_p(r,m)B_j(r) \; dr \qquad\qquad 3.32$$

Substituting in eq. 3.31 the A_{pj} integral and changing it into a matrix form will result in the following equation:

$$g = Aw + e \qquad 3.33$$

Where g is the optical data, $\mathbf{A}=[A_{pj}]$ is a weight matrix, w=$[w_j]$ is the weight vector, and e is the combined errors (mathematical and experimental). w_j can be obtained from $g = Aw + e$ by eq. 3.33, which presents the solution for a square matrix A :

$$w = A^{-1}g_p \qquad\qquad 3.34$$

The Regularization method (see Appendix D) will be used for smoothening of the errors in the calculations of the coefficients of the B-spline functions. Eq. 3.35 represents the weights solution with regularization.

$$w = (A^T A + \gamma H)^{-1} A^T g_p \qquad\qquad 3.35$$

Where γ denotes the Lagrange multiplier, $\mathbf{H}$ is smoothing matrix, g_p is the optical data, and $\mathbf{A}$ is the weight matrix.

To determine the size distribution in terms of surface-area concentration is required to use the kernel functions in terms of surface area also (see appendix B). That means that the procedure to calculate it is the same, only is needed to change the respective kernel function for surface-area concentration, and the term v(r) need to be changed by s(r). A basic explication of the developed algorithm is explained in Appendix D.

3.6.2 Microphysical Properties

The mean and integral properties of the aerosol ensemble that are calculated from the inverted ASD are the effects on radius or surface-area weighted mean radius (r_{eff}), total surface-area concentration (a_t), the total volume concentration (v_t), and the total number concentration (n_t). The effective radius is the mid-size radius in the distribution, usually in this point is present the maximum concentration [4].

$$r_{eff} = \frac{\int n(r)r^3 dr}{\int n(r)r^2 dr} \qquad 3.36$$

$$a_t = 4\pi \int n(r)r^2 dr = \int s(r)dr \qquad 3.37$$

$$v_t = \frac{4\pi}{3} \int n(r)r^3 dr = \int v(r)dr \qquad 3.38$$

$$n_t = \int n(r)dr \qquad 3.39$$

3.7   Single Scattering Albedo (SSA)

The SSA, w, is defined as the ratio of the scattering coefficient to α coefficient, and measures the ratio of α by scattering, Q_{sca}, to total α during a single interaction of a photon beam with a particle [42, 43]. SSA represents the fraction of scattered light with the respect to the total light.   The SSA depends of the Mie-efficiencies for spherical shapes.   The efficiencies depend of the refractive index m, the wavelength λ, and the particles radii r.   α efficiency is the scattering and absorption efficiencies sum. Eq. 3.40 and 3.41 shows the scattering and absorption efficiencies [7].

$$Q_{sca.} = \frac{128\pi^4 r^4}{3\lambda^4} \left| \frac{m^2 - 1}{m^2 + 2} \right|^2 \quad 3.40$$

$$Q_{abs} = \frac{8\pi r}{\lambda} \operatorname{Im}\left\{ \frac{m^2 - 1}{m^2 + 2} \right\} \left[1 - \frac{32\pi^3 r^3}{\lambda^3} \operatorname{Im}\left\{ \frac{m^2 - 1}{m^2 + 2} \right\}^2 \right] \quad 3.41$$

The ratio of the scattering coefficient to the sum of the scattering and absorption coefficients is then calculated to yield the scattering albedo. The SSA, then, indicates the percentage of atmospheric α due to scattering and that due to absorption [43]. An important point to be noted here is that the SSA provides a useful quantity as long as the scattering by aerosols is not very high.   As the particles scattering reaches higher values, multiple scattering comes into play.   Multiple scattering has been found to be small for visible wavelength Lidar scattering from clean air or haze, but a large component in the presence of the fog or clouds [42, 43].

$$w_0(\lambda) = \frac{Q_{sca}}{Q_{sca} + Q_{abs}} = \frac{Q_{sca}}{Q_{ext}} = \frac{\alpha_{sca}}{\alpha_{ext}} \qquad 3.42$$

3.8 Water Vapor Mixing Ratio (q_{H2O})

Atmospheric water vapor (WV) is very important greenhouse gas and is the agent of the hydrological cycle. Atmospheric WV is highly variable, and its quantification is still complex and is inducing huge uncertainties into the global climate models calculation and weather predictions [44]. New measurement techniques are currently being developed with the goal of reducing the lack of GDMN (Global Distributed Measurement Networks) [44].

This section addresses the implementation of the WV Raman Lidar technique at the CCNY Lidar laboratory. The WV at 407nm and the Nitrogen at 387nm are inelastic (Raman) channels of 355nm, radiation emitted by a Nd:YAG laser. The WV Raman Lidar technique uses the ratio of the rotational-vibrational Raman scattering intensities from WV and Nitrogen molecules, which are direct measurements of the atmospheric q_{H20}. The WV and Nitrogen Raman signals are given by eq. 3.43 [44].

$$P_{\lambda_R}(R) = \frac{K_s(\lambda_R, R)}{R^2} n_R(R) \frac{{}^\pi d\sigma(\lambda_0, \lambda_R, R)}{d\Omega} * \exp\left[-\int_0^z (\alpha_{\lambda_0}(r) + \alpha_{\lambda_R}(r)) dr\right] + N_{\lambda_R}(R) \qquad 3.43$$

Where, $P_{\lambda R}$ is the received Raman Lidar backscatter signal corresponding to nitrogen (λr= 387nm) or WV (λr= 407nm), K_s is function of the system detection, efficiency, overlap function, and the FOV of the telescope. n_R is the number density of Raman active molecule, $\frac{{}^\pi d\sigma(\lambda_L, \lambda_R, z)}{d\Omega}$ is the differential Raman backscatter cross-section, α is the extinction coefficient and N is the background (noise) signal.

By taking the ratio of the two signals one can obtain the q_{H2O} profile in eq. 3.44. Meanwhile, eq. 3.45 presents a simplified solution of the q_{H2O} [44].

$$\frac{P_{407}(R)}{P_{387}(R)} = \frac{\frac{K_s(\lambda_{407},R)}{R^2} n_{407}(R) \frac{\pi d\sigma(\lambda_{355},\lambda_{407},R)}{d\Omega} * \exp\left[-\int_0^z (\alpha_{355}(r)+\alpha_{407}(r))dr\right] + b_{407}(R)}{\frac{K_s(\lambda_{387},R)}{R^2} n_{387}(R) \frac{\pi d\sigma(\lambda_{355},\lambda_{387},R)}{d\Omega} * \exp\left[-\int_0^z (\alpha_{355}(r)+\alpha_{387}(r))dr\right] + b_{387}(R)} \qquad 3.44$$

$$\frac{P_{H_2O}(R)}{P_{N_2}(R)} = \left[\frac{K_{H_2O}}{K_{N_2}} \left[\frac{\left(\frac{d\sigma}{d\Omega}\right)_{H_2O}}{\left(\frac{d\sigma}{d\Omega}\right)_{N_2}}\right] \frac{T_{H_2O}}{T_{N_2}}\right] * q_{H_2O}(R) \frac{M_{air}}{M_{H_2O}} \qquad 3.45$$

Where T is the transmission for the two wavelengths through the atmosphere and M represents the mass of WV in atmosphere and dry air P_{H_2O} and P_{N_2} are the WV and nitrogen Raman signals, q_{H20} is the water vapor mixing ratio in [Kg water/Kg dry air] or in [ppmv], and the term $\Gamma = \frac{T_{H_2O}}{T_{N_2}} \cong 1$. Finally, the water vapor profile is given by the following equation:

$$q_{H_2O}(z) = \frac{K_{N_2}}{K_{H_2O}} \frac{\left(\frac{d\sigma}{d\Omega}\right)_{N_2}}{\left(\frac{d\sigma}{d\Omega}\right)_{H_2O}} \frac{M_{H_2O}}{M_{N_2O}} \frac{P_{H_2O}}{P_{N_2}} \qquad 3.46$$

In some publications is presented eq. 3.46 in terms of a calibration constant C. This constant is use to manipulate the q_{H20} using other instruments such as AERONET column WV product and *radiosound*. The calibration constant, C, is equal to:

$$C = \frac{K_{N_2}}{K_{H_2O}} \frac{\left(\frac{d\sigma}{d\Omega}\right)_{N_2}}{\left(\frac{d\sigma}{d\Omega}\right)_{H_2O}} \frac{M_{H_2O}}{M_{N_2O}} \qquad 3.47$$

Calculate the calibration constant from 3.47 is difficult because determined the k constant for nitrogen and WV is very hard. So, for this reason this constant is estimated using the dry air

density profiles and external equipment that reports the WV. There have been many calibration techniques proposed and used a long time [45-40]. Some methods suggest an approximate external calibration, a one point *in situ* value, or a calibration based on horizontal Lidar measurements. Two techniques of calibration are presented in [44] and were implemented in the developed algorithm presented in Chapter 5 with more details.

Finally, the corrected water vapor mixing ratio is given by:

$$q_{H_2O}(z) = C * \frac{P_{H_2O}}{P_{N_2}} \qquad 3.47$$

3.9 Relative Humidity (RH)

The study of RH is an important parameter to study the interaction of aerosol with the formation of cloud, and the formation of new aerosols that have negative impact in different atmospheric processes [44-50]. q_{H2O} is proportional to the water vapor mixing ratio, after the application of this is given by eq. 3.48, which depends on the Magnus formula. The Magnus formula is very used in meteorology for temperatures between -50 to 50 ^{o}C to determine the saturation pressure (P_{sat}), eq. 3.49 [49].

$$RH = \frac{q_{H_2O} \times P_{air}}{P_{sat}\left(6.22 + 0.01 \times q_{H_2O}\right)} \qquad 3.48$$

Where, P_{air} (hPa) is the dry air pressure determinate from ASA76 or a *radiosound*, q_{H2O} (g H_2O/Kg air dry) is the water vapor mixing ratio, and P_{sat} (hPa) is given by:

$$P_{sat} = 6.1086 \times \exp\left\{\frac{17.856T}{245.52 + T}\right\} \qquad 3.49$$

Where, T is the temperature profile in ^{o}C.

3.10 Conclusion

The Lidar equations involved in multiple wavelengths Lidar systems are organized in a user friendly format to simplify the algorithm development. The mathematical methods have been presented for Rayleigh, Mie (Elastic) and Raman (Inelastic) scattering theories. The optical characterization of the atmospheric aerosol can be performed just using the properties of the interaction between the laser beam radiation and the Atmosphere. Moreover, this chapter also shows that the Lidar technique is a powerful tool to measure and monitor the atmospheric optical parameters with high spatial and temporal evolution.

4 UPRM Lidar Laboratory for Remote Sensing Applications

In the last 2 years the UPRM NOAA-CREST troposphere research group has been studying the atmosphere using data from CCNY-Lidar while the UPRM-Lidar system was under assemble. Today, the UPRM-Lidar lab is completed and is an outstanding research facility capable of monitoring many atmospheric parameters, including: molecules, aerosol, clouds, and other events caused by the human activity. The measurements of the mentioned atmospheric parameters are obtained using Lidar systems technique and La Parguera AERONET station, and will be presented in Chapter 5. Both instruments are *in situ* and are very powerful in the determination of aerosol properties.

 AERONET is an aerosol network web which reports some aerosols properties using CIMEL photometer with 7 wavelengths. This is a passive system that uses sunlight to determine some aerosol properties in the total atmospheric column. The UPRM-Lidar, CCNY-Lidar and Calipso satellite have Lidar systems, using a Nd:YAG laser to scan vertically the atmosphere for the study of some atmospheric properties. Lidar systems are active systems because they use an artificial light source to study the atmosphere.

The atmospheric properties under study depend on the transmitted and received light wavelength. There are different types of Lidar systems defined based on the transmitted and received wavelengths. If the received wavelengths are the same as the transmitted it is known as an Elastic Lidar or Mie-Lidar, and when the wavelengths are different it is called

Inelastic Lidar or Raman-Lidar. The UPRM Lidar System is an Elastic Lidar because only reports products for the same transmitted wavelengths, in the same way as Calipso satellite. Section 2.5 elaborates on the details of Elastic and Inelastic scattering. Appendix F, G, H, and I, explain the UPRM Lidar specifications, CCNY-Lidar system, Calipso satellite, and AERONET, respectively.

Lidar has advantages over passive systems because it is sunlight independent. Lidar system can operate at night but not under rain. This system can be used to obtain some products used to study the atmosphere, for example images of the PBL, clouds, dust layers, or aerosol layers. Obtaining images and products as a function of height is one of the major advantages over the passive remote sensing systems.

In this chapter example of UPRM-Lidar signal detection capability is presented.

4.1   UPRM Signal Detection Capability

The UPRM-Lidar system as described above performs vertical observations acquiring elastic signals at the three fundamental wavelengths (355, 532, and 1064nm). Since December 2008, pure signals have been recorded as a result of the vertical scanning of the atmosphere. Fig. 4-1 shows the logarithmic range corrected (or adjusted) signals images at the three Mie-channels with a vertical resolution of 7.5m. These images show the PBL, aerosol layers, and clouds at different altitudes on March 24th, 2009. The 355nm channel detects small particles suspended in the Atmosphere, the 1064nm detects larger particles meanwhile the 532nm detects a mix of particles of different sizes. Comparing the scenario

between the three channels based on the detection of particles, the 355nm shows with more

detail the PBL because there are a high concentration of small particles (molecules) and the

clouds at 9km are detected also, the 532nm channel show the PBL with less intensity but on

the top of it shows an aerosol layer in form of cirrus cloud and in altitudes of 9km and 13km

illustrate the presence of clouds. The 1064nm channel only detects larger particles such as

clouds, dust, smoke and other events. In this case this channel shows the clouds suspended at

the top of the PBL, and at 9km. The clouds at 13km appear blur (the same is true for 355nm)

because the signal was attenuated by the presence of Oxygen and Nitrogen (Rayleigh

scattering), and aerosols at lower altitudes.

a)
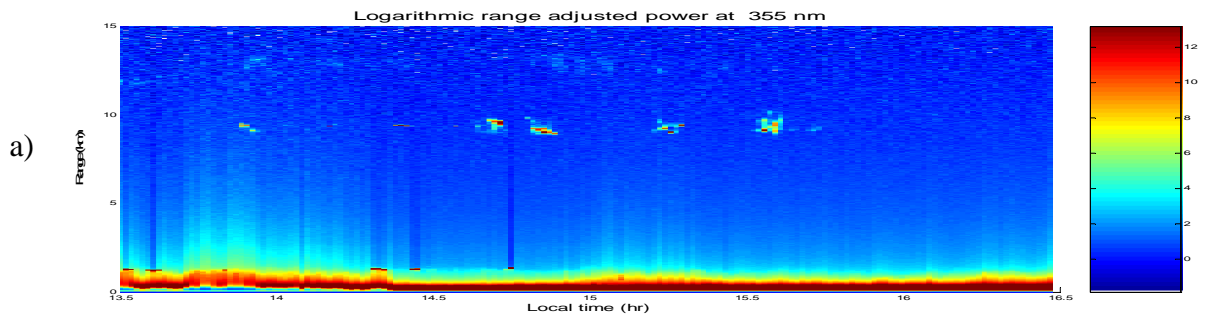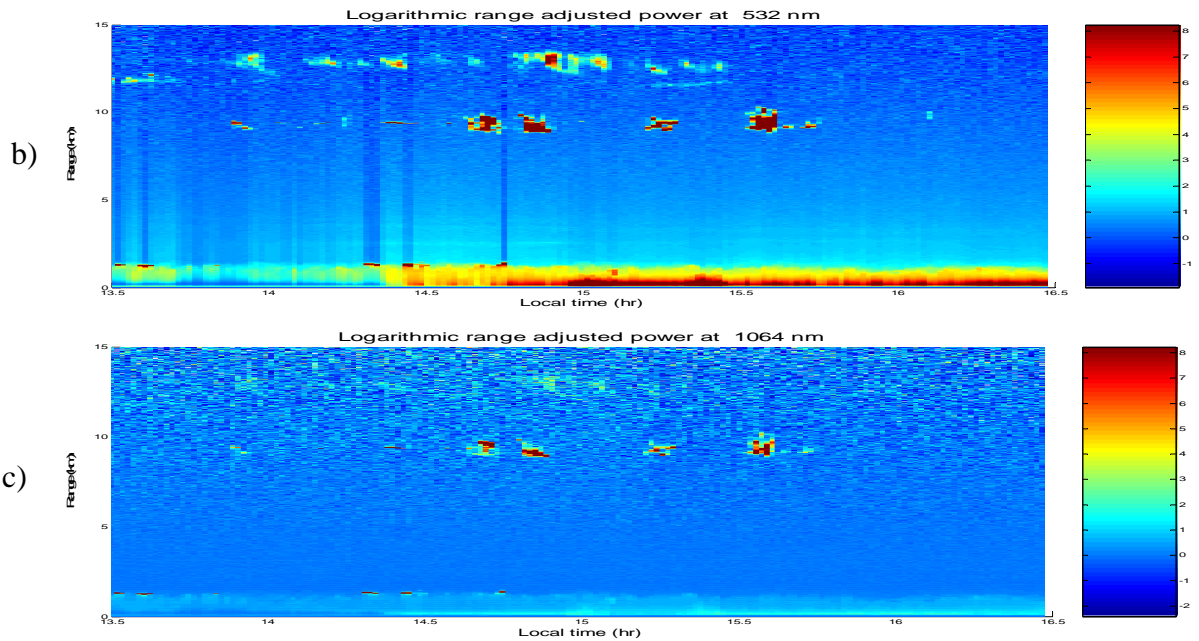
Figure 4-1 UPRM-Lidar logarithmic range adjusted power images at 355nm (a), 532nm (b), and 1064nm (c).

The Lidar data models are analyzed using statistics. The statistics of remote sensing data are influenced by the atmospheric and weather conditions in the scanned region. The atmospheric effect tends to correlate the data between the different wavelengths of the Electromagnetic Spectrum along a straight line through the origin of the reflectance scattergram. Also, the collected data is influenced by the sensor's spectral passband locations and widths, and noise characteristics. Random, spatially uncorrelated sensor noise increase within class variance of all atmospheric particles and aerosols suspended equally. Spatial and spectral statistics of the data are influenced by the sensor's spectral response function, which increase the spectral correlation length, reduces within class variance, and creates mixed spectral vectors [45].

An example of the scatterplot for the three Mie-channels images is obtained for the data exposed in Fig. 4-1 and is presented in Fig. 4-2. Each mark represents one or more pixels. Based on this figure, the 532nm channel detects more scattered beams than the other two channels, which indicates that 532nm is reflected from more particles than the other two channels. The detection depends on the laser transmitted power and the attenuation caused by Rayleigh scattering. The 355nm channel is more sensitive to be attenuate by the Rayleigh scattering occasioned by oxygen, ozone, and other natural molecules.

The image histogram describes the statistical distribution in terms of intensity in each received laser beam count. The histogram is a useful tool for contrast- enhancement. Fig. 4-3 shows the histogram of the three Mie-channels where the 532nm has more contrast because the intensity is more distributed as the other two channels, and is useful to determine the correlation between each channel. The correlation is very important to study the detection between each sensor. The correlation between each dual combination of 355 and 532nm, 532 and 1064nm, and 355 and 1064nm is presented in Fig. 4-4, where the correlation matrix of each channel combination is given by:

$$r_{355/532} = \begin{bmatrix} 1 & 0.6330 \\ 0.6330 & 1 \end{bmatrix} \quad r_{532/1064} = \begin{bmatrix} 1 & 0.8938 \\ 0.8938 & 1 \end{bmatrix} \quad r_{355/1064} = \begin{bmatrix} 1 & 0.4868 \\ 0.4868 & 1 \end{bmatrix}$$

The 355 and 532nm channel correlation is 0.6330, confirming the presence of small particles such are aerosols present in the PBL and the free-Troposphere region. The correlation of the 532 and 1064nm channels is 0.8938 which represents a high correlation with the visible and

near infrared particles. This correlation is causing by particles scattering presented in clouds that were detected by both channels. The correlation between 355 and 1064nm channels is 0.4868. This correlation value confirms that the detection of both channels is different because the 355nm detects small particles meanwhile the 1064nm detects larger particle such as sea-salt particles, dust, smoke, etc., suspended in the PBL and clouds. In general, the correlation between the three channels are moderate because are more than 0.48. Also, these correlation values show that the sensor's alignment is very important to make good atmospheric retrievals and obtain high quality images.
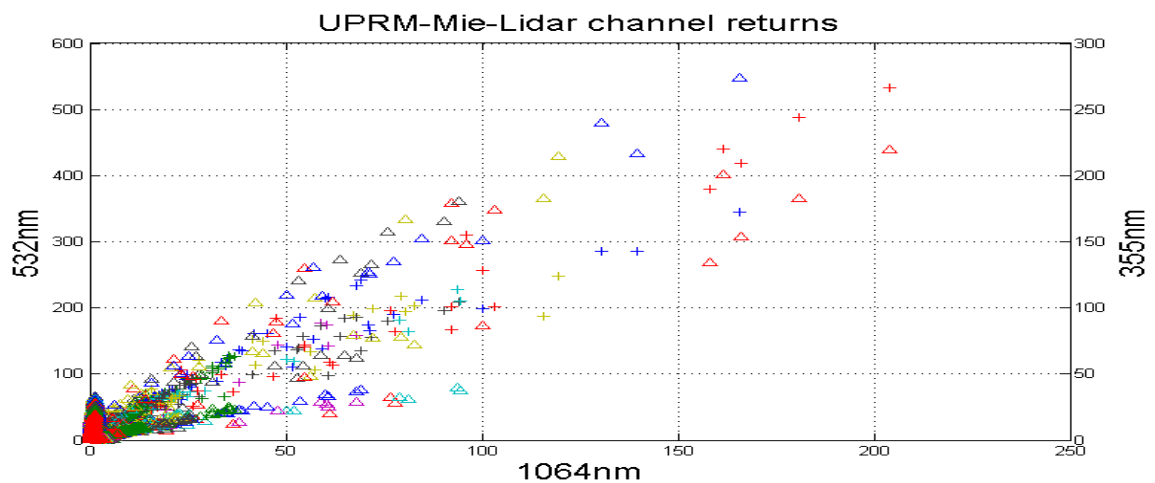
Figure 4-2 UPRM-Lidar Mie channel received signals scatterplot.
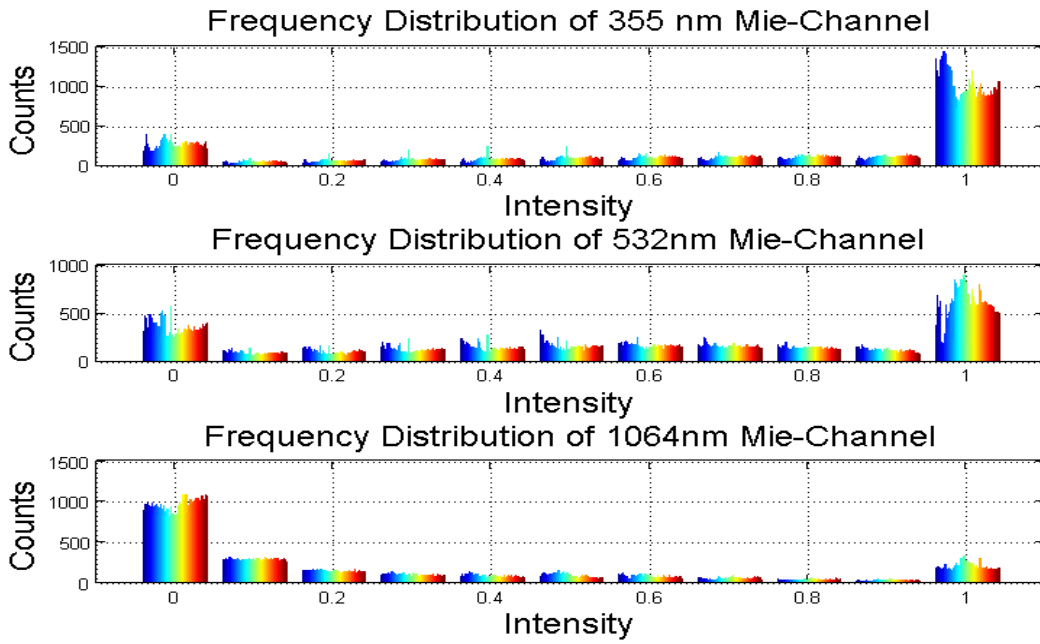
Figure 4-3 UPRM-Lidar Mie channel histogram.
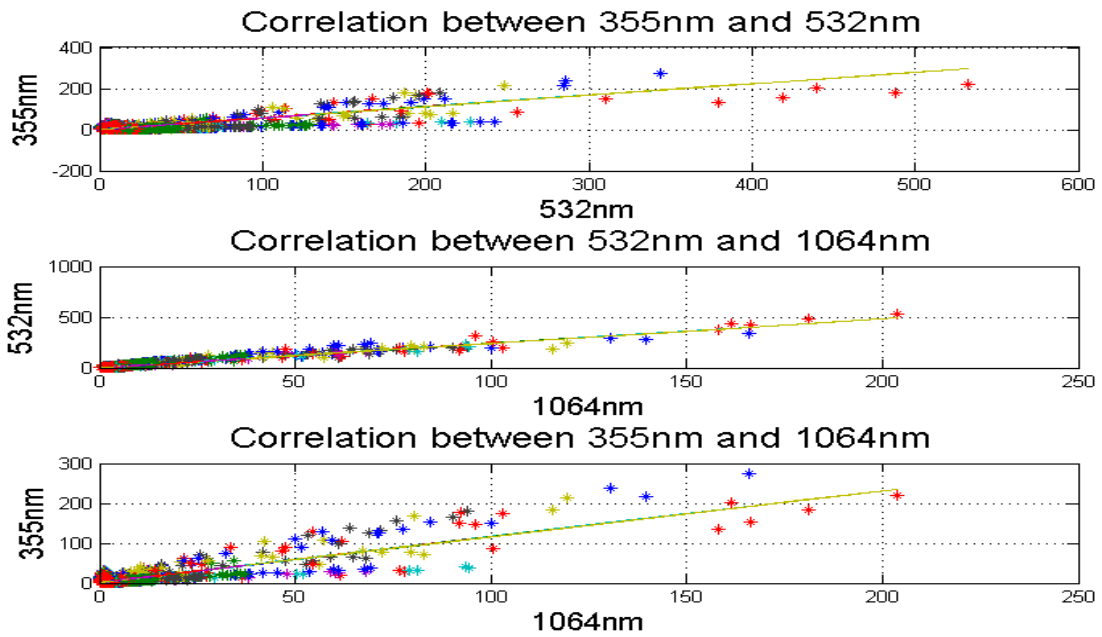
Figure 4-4 UPRM-Lidar Mie channel correlation.

The acquisition 1200 shots per file with 7.5m of vertical resolution permit the atmospheric analysis per minute of the collected data up to the Stratosphere. Fig. 4-5 shows the backscatter returns signals of one single file at March 24th, 2009 at 2:41Pm, where the images in the order from top to bottom represent the received signal, background filtered signal, and range adjusted signal, respectively. The range background and range adjusted signals show a cloud at 9km and thin cloud at 13km. The intensities of the backscatter signals are different in the upper troposphere (below the clouds) due to the laser attenuation caused via molecules and particles scattering in different wavelengths. In lower altitudes the received intensity is different for each channel because the molecules presence cause the attenuation occasioned by Rayleigh scattering. The study of aerosols and clouds will be discussed with more details in Chapter 5.
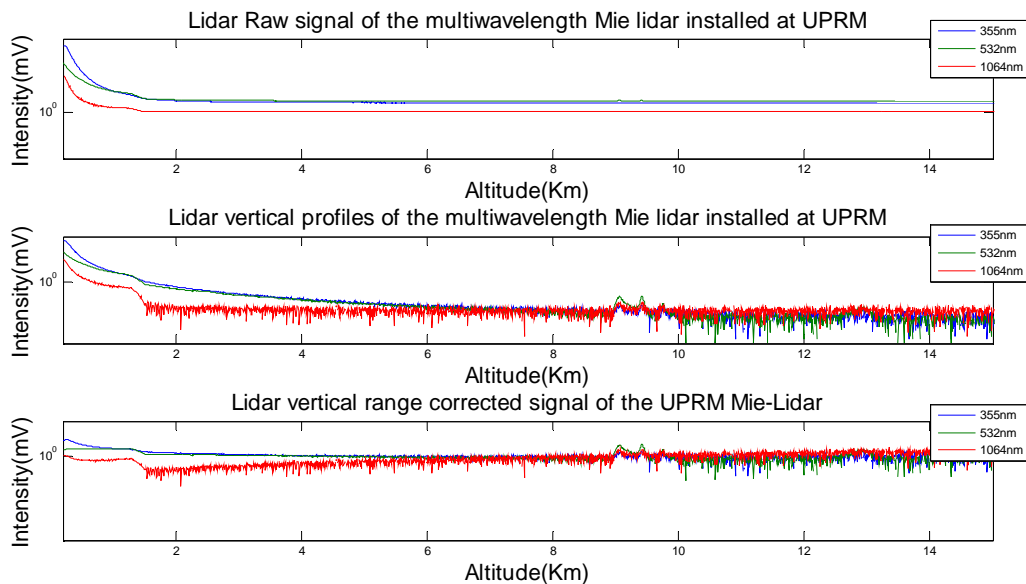
Figure 4-5 UPRM-Lidar signal filtering processing and range correction at 2:41Pm.

4.2   Conclusion

The remote sensing tools presented in this chapter are usefully for atmospheric studies. The combination of these systems is used to determine different optical parameters that are fundamental to continue with the aerosol characterization and clouds studies. The UPRM-Lidar was presented as the main system presenting high spectral, spatial and temporal resolution that permits the detection of different particles that can be visible only in different region of the electromagnetic spectrum that cannot be seen in the visible region or vice versa.

5 DATA PROCESSING AND RESULTS

Real data collected using the UPRM-Lidar and CCNY-Lidar systems are used to run the developed algorithms. High spatial and temporal resolution data at 355, 387, 407, 532, and 1064nm are processed to make studies about different aerosol parameters that ultimately play an important role on climate change.

5.1 Optical properties of aerosols and cirrus clouds

The study of aerosols and cirrus clouds is very complex, because their distribution over time and space is extremely variable by nature of physical and chemical properties. There are laboratories that measure their chemical and physical properties, for example: the Colorado State University has a laboratory of this type on Fort Collins that studies the properties of different aerosols suspended in the Atmosphere. Climate models require measurements of ASD and optical properties (extinction and backscatter coefficients) for their radiative budget calculations [22]. The aerosols interaction with light can be quantified by a set of measured or estimated parameters: α_{aer} , β_{aer}, L_{aer}, AOD, ASD, SSA, α_{abs}, α_{scat}, WV, RH, and the complex refractive index (m) (Chapter III presented more details and definitions of the mentioned parameters). The cloud's *albedo* depends on their AOD, the droplet effective radius (r_{eff}) and the geometrical thickness [18]. The wavelength dependence

of these parameters is critical, and generally known as Angstrom (Å) coefficient, described in Chapter 3.

The above mentioned parameters are measured and estimated via the incorporation of two *in-situ* ground systems such as Lidar and AERONET systems. Also, the Lidar satellite CALIPSO can provide α_{aer}, β_{aer}, and AOD products. The calculations and models simulations of these parameters are based on measured optical properties. The ASD and number distribution based on Mie theory using regularization inversion method was obtained as can be seen in reference [10].

5.2 Algorithms for Atmospheric Parameters Determination

The UPRM-Lidar system measurements obtained for the elastic channels of 355, 532, and 1064nm, and the CCNY-Lidar system measurements obtained for the same elastic channels and two additional Raman channels of 387nm and 407nm were considered for this project. The Lidar signal processing algorithm used in the determination of the β_{aer} and α_{aer} coefficients, and L_{aer} is shown in Fig. 5-1.
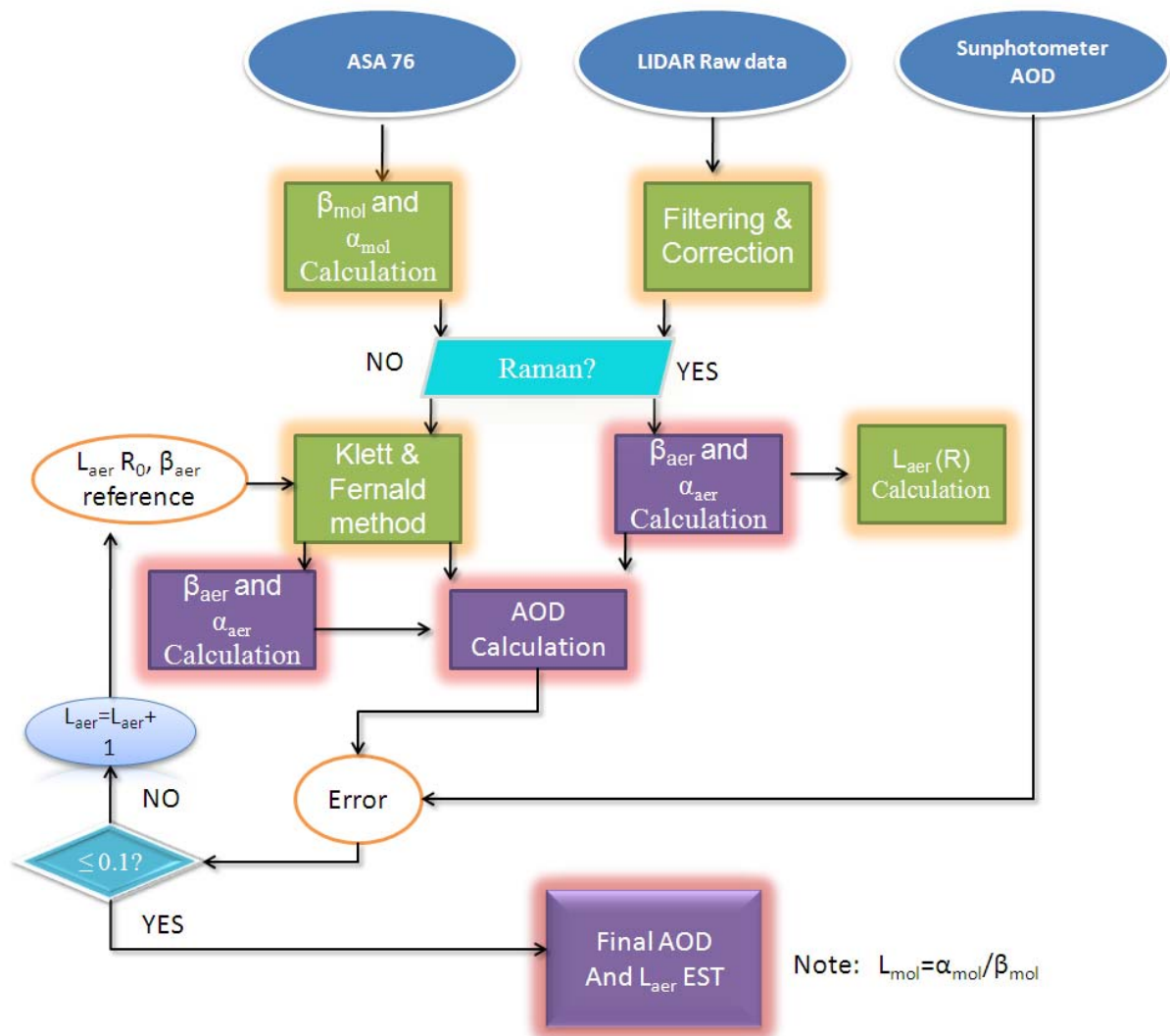
Figure 5-1 Block diagram of the combined Elastic and Inelastic signals algorithm for the determination of L_{aer} coefficients, and L_{aer} estimation.

The algorithm above takes into account both elastic (Mie) and inelastic (Raman) received signals and is complementary with the ASA76. The ASA76 can be substituted by the local meteorological and regional *radio-sounding* data. The Mie or elastic scattering technique allows the molecular extinction (α_{mol}) and backscatter (β_{mol}) results to be

introduced to the *a priori* L_{aer} in the Klett & Fernald inversion method, in order to obtain a high resolution β_{aer} coefficient. Using the relation between the L_{aer}, β_{aer} and α_{aer} coefficients, the α_{aer} coefficient can be estimated. With the estimated α_{aer} coefficient the AOD can be calculated and compared with the AOD given by AERONET or a portable sun-photometer [51]. For the elastic data, the *a priori* L_{aer} needs to be changed until the AOD values are close between the two systems, resulting in the estimated L_{aer}.

Another important issue here is the determination of the *a priori* β_{aer} at the reference altitude R_0 ($\beta_{aer}(R_0)$). In this algorithm the reference altitude, R_0, is considered at higher altitudes where the aerosol concentrations are negligible and the molecules concentrations are considered. The $\beta_{aer}(R_0)$ is determined using the color ratio function, which is given by:

$$CR(R) = \frac{\beta_{mol}(R)}{\beta_{mol}(R)} + \frac{\beta_{aerl}(R)}{\beta_{mol}(R)} = 1 + \frac{\beta_{aerl}(R)}{\beta_{mol}(R)} \qquad 5.1$$

Assuming the condition of $CR(R) < 1.1$ and the reference altitude R_0, the $\beta_{aer}(R_0)$ value can be estimated because the $\beta_{mol}(R_0)$ is estimated from the ASA76 or a *radiosound*. These assumptions are based on Klett and Fernald methodology.

The Raman or inelastic scattering technique permits a preliminary estimation of α_{aer} coefficient. The β_{aer} is then calculated separately. This result is a more precise determination of L_{aer}, which can then be used as more realistic approximation of the atmospheric conditions.

5.2.1 UPRM-Lidar Algorithm Results & Discussion

Regular observations taken since December 2008 were used to determine the β_a and α_a coefficients based on the elastic signals of the UPRM-Lidar system. The principal limitation of this system and the developed algorithm is the use of *a priori* L_{aer} values, but these can be estimated using an external equipment that reports the AOD such as AERONET station in La Parguera and a portable sun-photometer. An example of logarithmic range adjusted power intensity image at the 532nm elastic channel on March 24th, 2009 is illustrated in Fig. 5-2 for an upper troposphere loaded with aerosol layers and cirrus clouds. The same methodology was implemented for 355 and 1064nm.
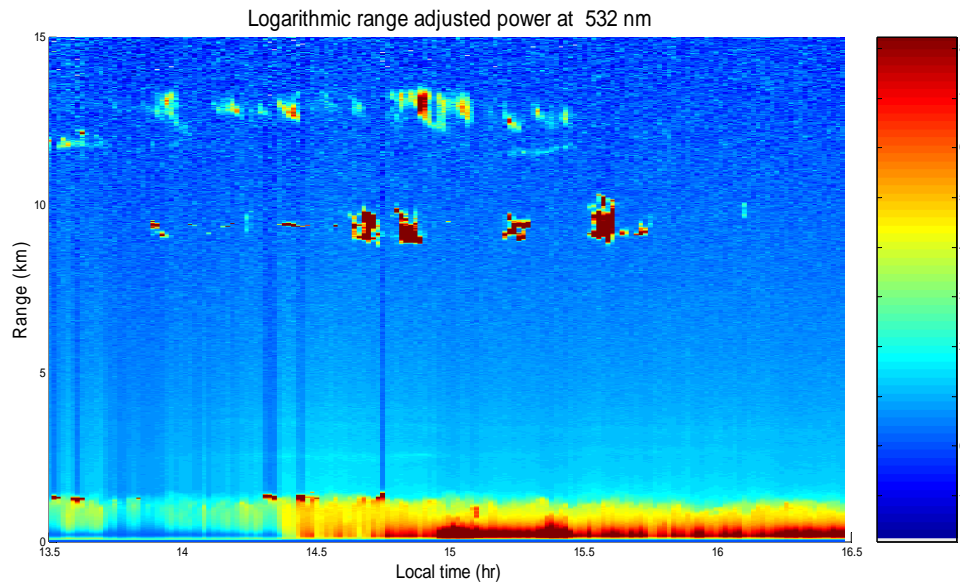
Figure 5-2 UPRM logarithmic range corrected power image at 532nm on March 24th, 2009 in the time interval of 1:30PM to 4:30PM.

5.2.1.1 PBL

The PBL can be observed to have an extension up to 1.5km as shown in Fig. 5-2, where the vertical distribution and time evolution of the regional atmospheric space scenario is presented. The 1200 shot file collected at 2:41Pm is used to study the PBL region. The PBL altitude can be estimated using the relations between the Lidar ranges corrected signals, presented in Fig. 5-3. The PBL altitude is the point where the signal attenuation has nearly ended. This attenuation is caused by Rayleigh scattering caused by the presence of nitrogen and oxygen molecules. In Fig. 5-3 the PBL altitude is about 1.5km because at this altitude the signal has reached its limit in attenuation. Up to 1.3km, the attenuation is caused by high backscattering of light due to a high particle concentration, see Fig. 5-2.
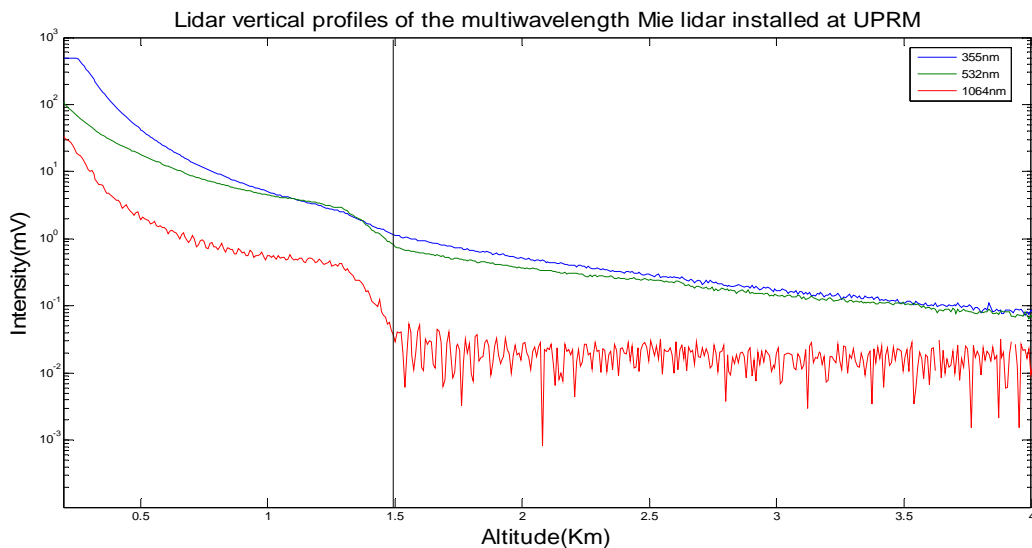
Figure 5-3 UPRM-Lidar raw signals at 355, 532, and 1064nm wavelengths on 24 of March 2009 at 2:41 PM.

Table 5-1 shows the PBL optical properties calculated and estimated at the three operational wavelengths. The AOD and Extinction values can be seen to decrease as the

wavelengths increase, a theoretically proven pattern. Usually the number of small particles in the PBL is higher than the number of larger particles, except for specific circumstances such as the presence of desert dust, smoke, etc.

PBL optical properties			
Wavelength (nm)	**355**	**532**	**1064**
AOD	0.045	0.021	0.006
α_{aer}	0.21	0.19	0.1
β_{aer}	0.008	0.0065	0.02

Table 5-1 PBL optical properties.

Using these results the aerosol microphysical properties (Table 5-2) were determined for each particle type: *Aitken nuclei mode* (<<0.1μm), *Accumulation mode* (0.1-2.5μm), and *Coarse mode* (2.5-10μm). The preliminary calculations of the PBL microphysical properties were done based on the regularization method used in previous calculations, published in [10]. The results presented in Fig. 5-4 show the ASD in terms of surface-area for the three aerosol classes.

PBL				
	n_t (cm^{-3})	r_{eff} (μm)	a_t (μm^2/cm^3)	v_t (μm^3/cm^3)
Aitken nuclei	23	0.06	27.9	53.7
Accumulation Mode	17	1.25	37.2	15.6
Coarse Mode	6	5.8	0.23	0.45

Table 5-2 PBL Microphysical parameters.
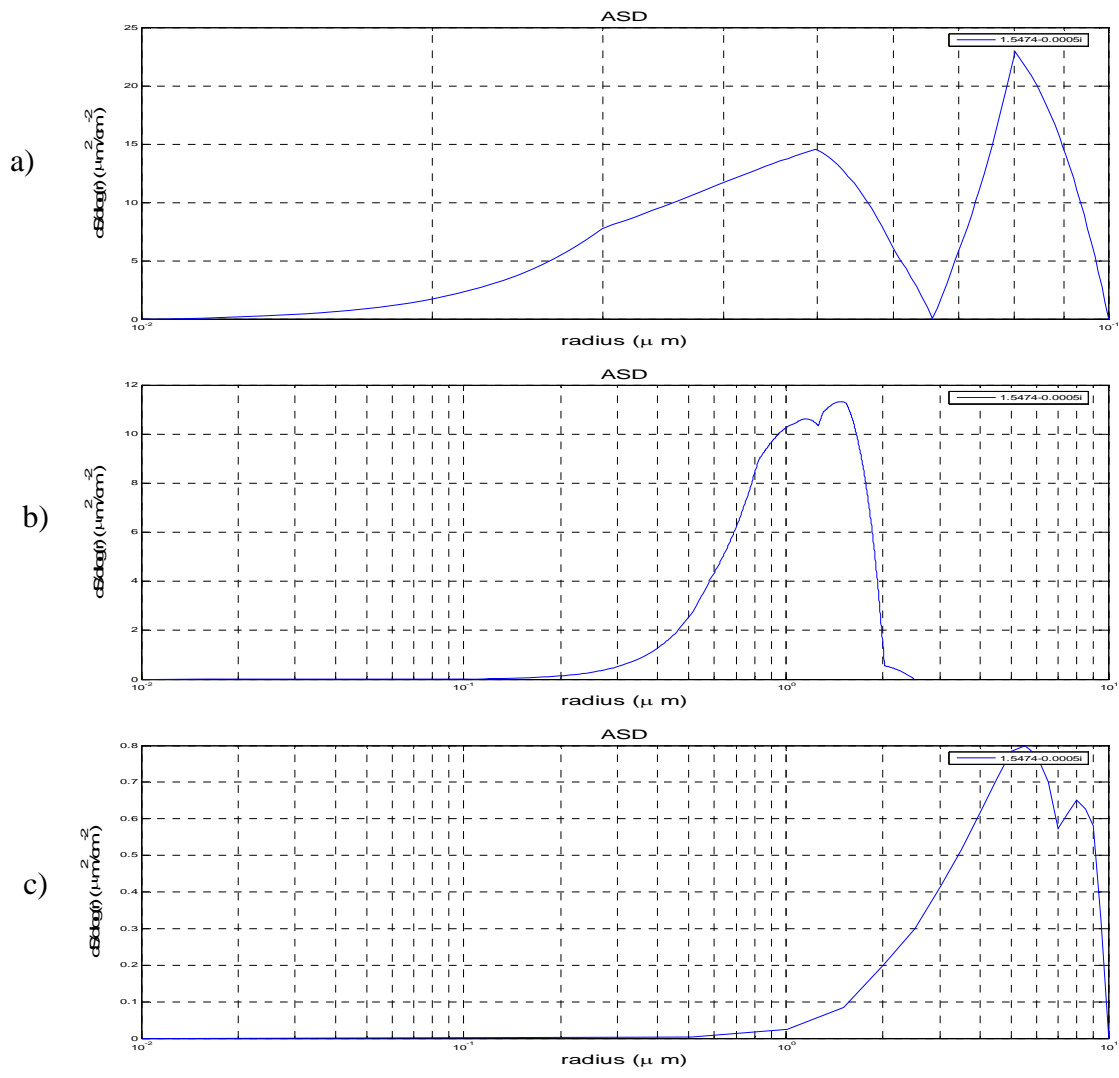
Figure 5-4 *Aitken* (a)*, Accumulation* (b)*, and Coarse* (c) *mode* ASD in terms of surface-area

distributions on the PBL region. Aitken (a) particles in the PBL region are not in spherical

shape because this type of particles come from combustion process typically and are mixed

with other particles, forming ne particles usually have larger sizes.

The results for the day (March 24, 2009) clearly show that small particles dominate

the PBL region. These particles play an important role in the formation of clouds, through

interaction with other particles in the PBL, changing their composition and shape to form larger particles which in turn lead to cloud formation.

Another important parameter to study in the PBL region is the particle matter (PM2.5). These particles, in increased concentrations in the PBL, have negative consequences on human health due to easy inhalation. This parameter is estimated using the AOD product calculated using the α_{aer} coefficient [52]. The PM2.5 is estimated using the Infusing Satellite Data into Environmental Applications (IDEA) product for the north-east part of America, where it is assumed that 1AOD is approximated to $60\mu g/m^3$ of PM2.5. Most publications compare the estimated PM2.5 obtained using the AOD values obtained by Lidar systems with the results obtained by TOEM, equipment that measures the PM2.5 and is generally used to measure air quality [52]. Based on this assumption, the estimated PM2.5 concentration at 2:41PM on the region of UPRM is approximately $1.26\mu g/m^3$ indicating good air quality with an index of 4, which is calculated using EPA's calculator presented in [53]. The air quality standard index varies depending upon the country of interest. In USA the air quality is classified as follow: 0-50 good, 51 to 100 moderate, and larger than 101 are considered unhealthy [54], see Appendix J for more details. The air quality index value depends on the traffic flux, the emission emitted by industries, sea-salt, etc.

5.2.1.2 Tropospheric aerosols

Fig. 5-5 a & b shows the α_{aer} and β_{aer} coefficient at 2:41 PM of the same mentioned date. These coefficients are fundamental to proceed with the aerosol characterization. Both coefficients present at altitudes less than 1.5km the respectively values for the PBL region, from 1.5km to 8.2km shows oscillations which represents aerosols that can be sea-salt

70

particle4s (marine aerosols) based on the estimated L_{aer} values. From altitudes larger are

present clouds, these clouds are presents at 9km and 13km, the oscillations between

clouds are the presence of aerosols or particles which play an important role in cloud

formation.
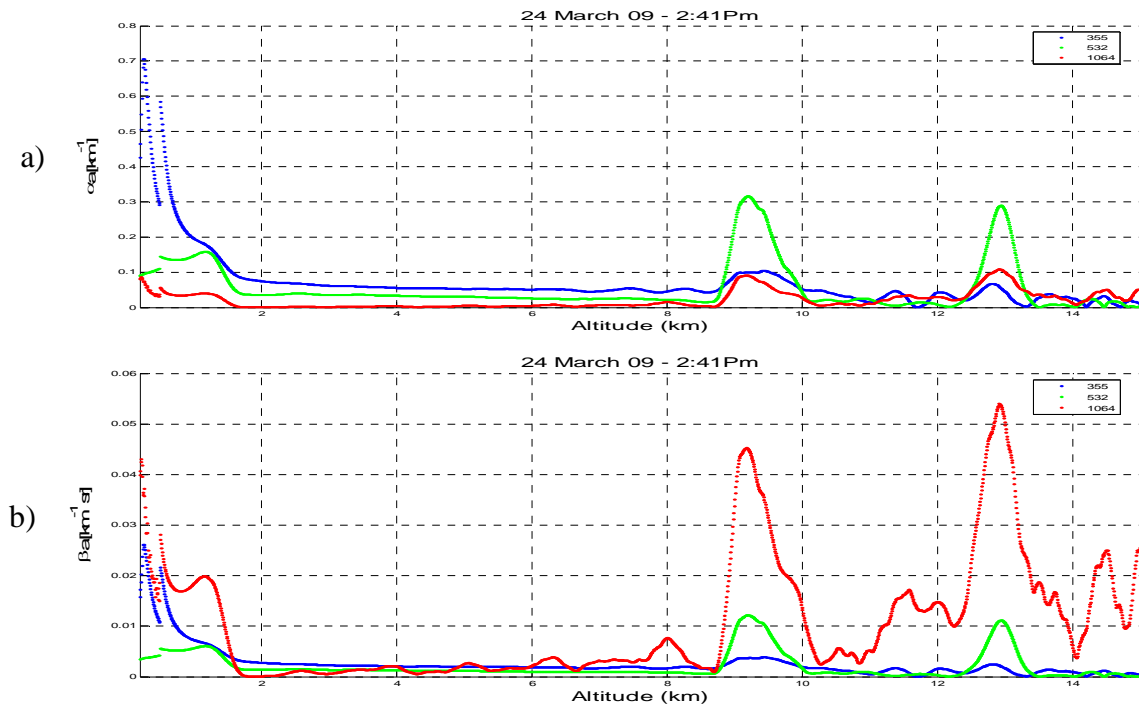
Figure 5-5 α_{aer} (a) and βaer (b) coefficients at the three wavelengths (Blue-355nm, Green-532nm, and Red-1064nm) using the Klett & Fernald inversion method with an estimate L_{aer}=27sr for 355 and 532nm, and L_{aer}=10sr for 1064nm at the column of up to 15km.

The AOD plots calculated from the α_{aer} coefficient profile at 355, 532, and 1064 nm

are presented in Fig. 5-6. The valid altitude for the UPRM-Lidar station measurement is in

the range from 200m to 15 Km. In order to avoid cloud interference at 9km, the simulation is

run from 200m to 8.2km (Fig. 5-6 a &b). In Fig. 5-6 a) the AOD plots changes drastically at

71

9km and 10km by the presence of clouds. For this reason in Fig. 5-6 b) shows the AOD plots up to 8.2km with the purpose to avoid the clouds and proceed with the aerosol characterization.
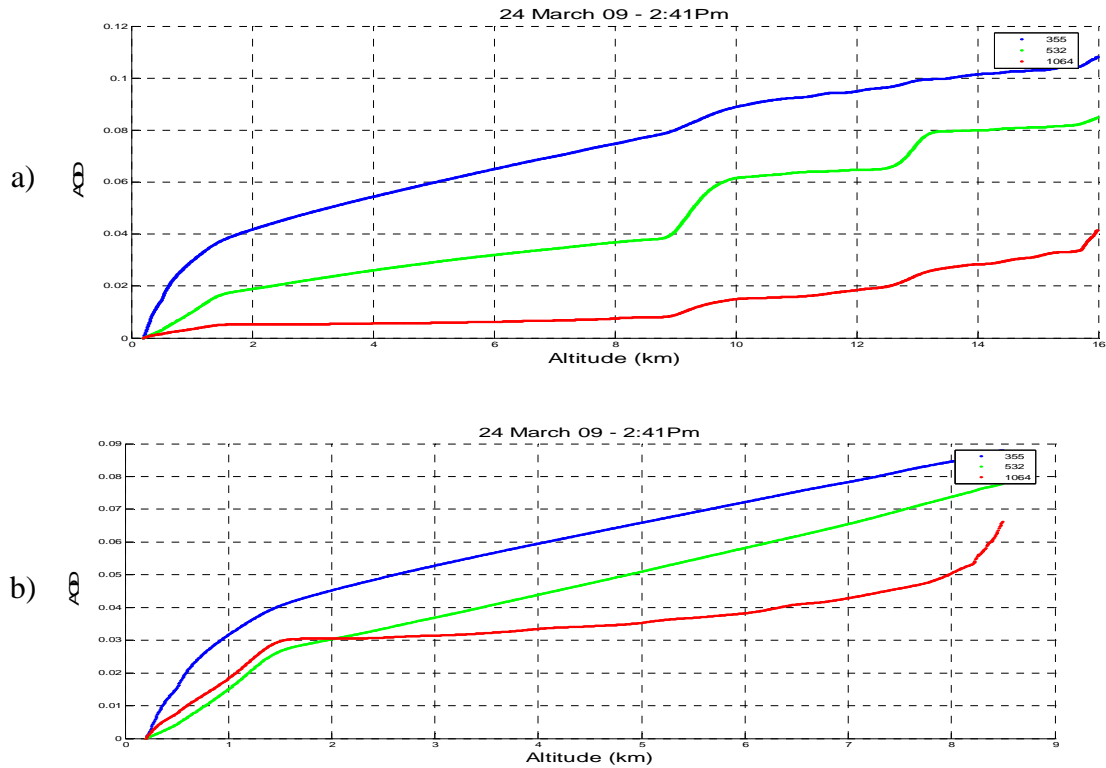
Figure 5-6 AOD at the three wavelengths (355(blue), 532(green), and 1064(red)), taken March 24th, 2009, AOD values up to 15km column (a) and up to 8.2km column to avoid the clouds present at 9km (b).

The resulting statistics obtained from the Mayagüez Lidar optical parameters are given in Table 5-3. These statistics are determined using the 8.2km column to avoid the presence of clouds at an altitude of 9km. The total column and averaged AOD decrease with the wavelength. AERONET reports the AOD corresponding to the total Atmospheric

column at 340, 380, 440, 500, 675, 870, and 1020nm. The AOD data measured by AERONET was recalculated at the UPRM-Lidar wavelengths of 355, 532, and 1064nm using a wavelength dependency law (Å exponent), determined from AERONET data taken at the same time as the UPRM-Lidar measurements. The AOD median of the complete Lidar column at 4:00 PM where the Troposphere was clear has been used to estimate L_{aer} using the AERONET AOD values. Table 5-4 shows the used AOD values from AERONET and the AOD values obtained by the UPRM-Lidar to estimate the L_{aer} values at the three operational wavelengths using the AOD matching method. The minimum errors obtained via the AOD matching method are close to 4.5% for 355nm, 0.38% at 532nm, and 5.0% at 1064nm.

Optical properties statistic									
	α 355	α532	α1064	β 355	β 532	β 1064	AOD 355	AOD 532	AOD 1064
Max.	0.75	0.27	1.1	0.025	0.0060	0.079	0.088	0.080	0.070
Min.	0.0040	0.0040	0.0010	1.2e-4	8.1e-5	8.0e-5	0	0	0
Mean	0.12	0.094	0.080	0.0035	0.0021	0.0060	0.060	0.045	0.034
StDev	0.11	0.052	0.12	0.0040	0.0012	0.0080	0.020	0.020	0.010

Table 5-3 Statistics of the Lidar extinction and backscatter coefficients, and AOD from March 24th, 2009 at 2:41 PM.

AOD matching method results for aerosol lidar ratio estimation

Wavelength	355nm	532nm	1064nm
$AOD_{AERONET}$	0.129	0.103	0.080
AOD_{Lidar}	0.1178	0.1038	0.0885
L_{aer} estimated	30	45	14

Table 5-4 L_{aer} estimated values using the AOD matching method. Based on the estimated L_{aer} values, the 355 and 532nm channels detects marine aerosols presented, meanwhile the 1064nm channels only detect clouds.

In theory, the Å exponent of 1 to 4 indicates that a fraction of aerosols are made of small size particles. The Å exponent values observed in the 8.2km column are in average between 2 and 4, indicating small sized particles. (see Fig. 5-7). The Å coefficient is a measure of distinction between small and large particles. Small values refer to large particles which are for instance cloud constituents, and large Å coefficient represents aerosols.
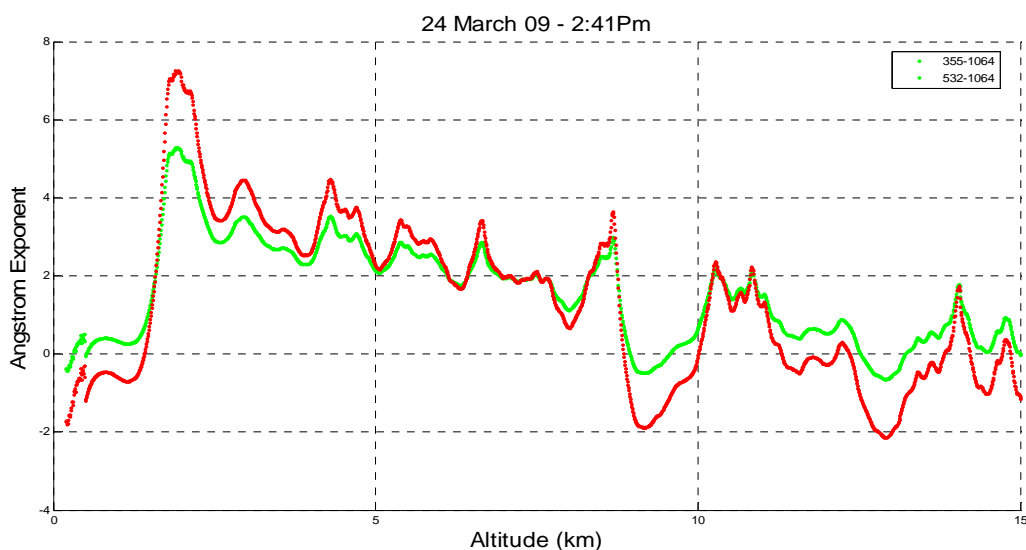
Figure 5-7 Å Coefficient based on the wavelength combinations of 355/1064nm (green), and 532/1064nm (red).

Based on the β_{aer} and α_{aer} coefficient average values at 355, 532, and 1064nm, the microphysics correspondent to the 8.2km column were preliminary calculated using the regularization method described in Chapter 4 and in [10]. The results of the simulations are illustrated by Fig. 5-8 for a maximum radius set at 2.5µm. The estimated r_{eff} =1.25µm, the total number density (n_t) is close to 9 particles per cm^{-3}, the total surface-area concentration a_t=4.12µm^2/cm^{-3}, and the total volume concentration v_t=1.71µm^3/cm^{-3}. The average complex refractive index m=1.55+0.005i indicates an intermediate absorption of the aerosol present in the column of 8.2km (free-troposphere). The SSA measures the light absorption from 0 to 1, where 1 represents 100% of the light is absorbed. In the column under study, the SSA is close to 0.6, which confirms the mid-term light absorption by the column representative aerosols.

The ASD distribution in Fig. 5-8 shows a maximum in number density observed is between 1.2 and 1.6µm, which indicates *accumulation mode*. In terms of surface-area concentration, the maximum is located between 1 and 1.3µm, also signifies *accumulation mode*. Finally the volume concentration also confirms the presence of *accumulation mode* particles suspended in the column of 8.2km. For the above results, the average values could be considered statistically representative for the UPRM-Lidar system and La Parguera AERONET station, but the results depend on the use of *a priori* β_{aer} in a region of free-aerosols, L_{aer} and a reference altitude (R_0), and the estimated L_{aer} values using the AOD matching method (Lidar AOD and AERONET AOD).
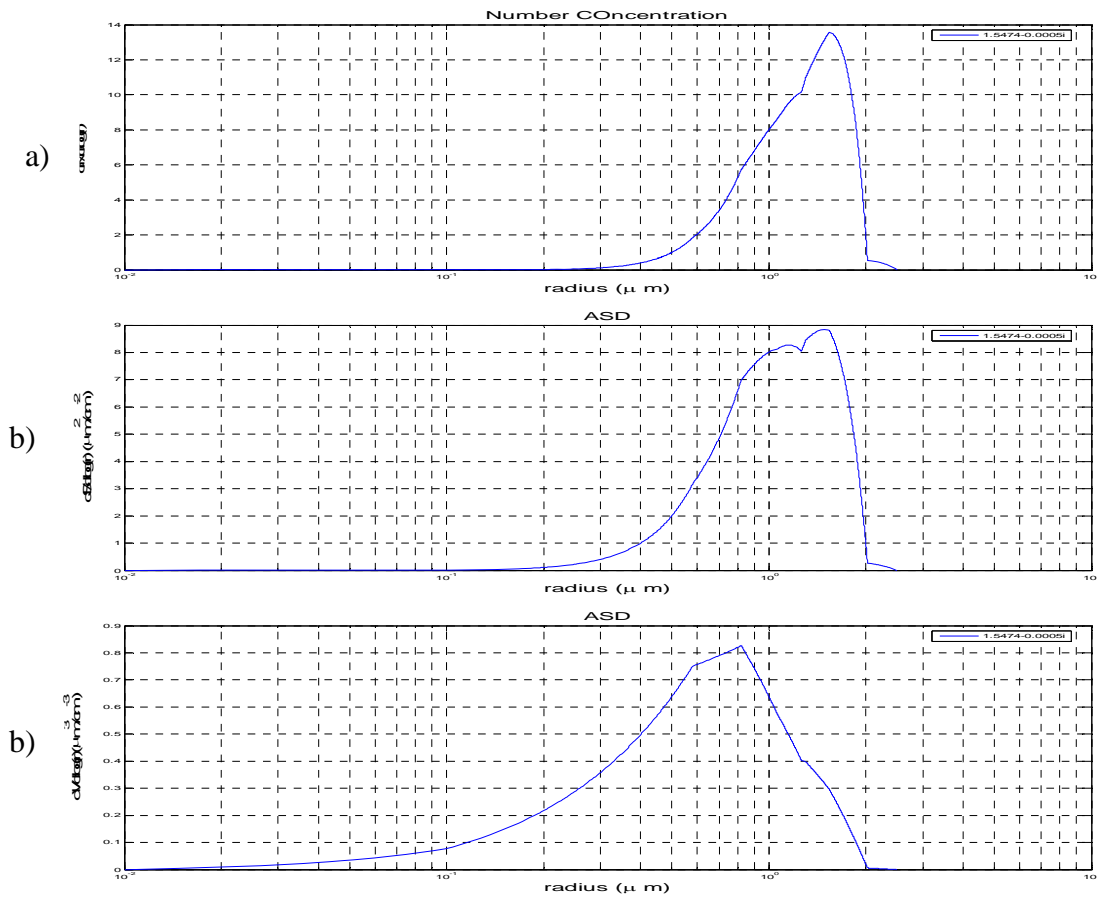
Figure 5-8 ASD plots for number concentration (a), surface-area (b), and volume (c).

76

The Lidar system detects aerosols with high sensitivity in the atmospheric column obtaining a realistic comparison between Lidar and AERONET. The Lidar inversion solution depends on the reference altitude (R_0), initial L_{aer}, and β_{aer}, chosen as reference for the estimation of the presented aerosol properties [10, 38]. The user needs to adjust the reference values in such a way that acceptable plots of β_{aer} and α_{aer} coefficients are obtained which are parameters in the calculation of ASDs. The Lidar is stable and as such has real potential for long-term monitoring of varied tropospheric properties.

5.2.1.3 Cirrus clouds detection

The Lidar methodology presented in this section will be based on Mie approach for determining the three parameters of β_{aer} and α_{aer} coefficients, and ASD for cirrus clouds. The regularization method was used along with these parameters for the estimation of ASD [55, 56]. The cirrus cloud study shown here was based on the UPRM-Lidar data to demonstrate the determination of the optical parameters.

Using the same observation over the region of Mayagüez on the same day as was presented in section 5.2.1, the presence of clouds can be observed at different altitudes from the data taken over a period of 3 hours (see Fig. 5-9). In Fig. 5-9 the PBL region is around 1.5km and is represented by a horizontal black line. On the top of the PBL there are clouds at different time intervals, marked by three circles. The other two larger circles are used to show the cirrus clouds at 9km and 13km of altitudes.
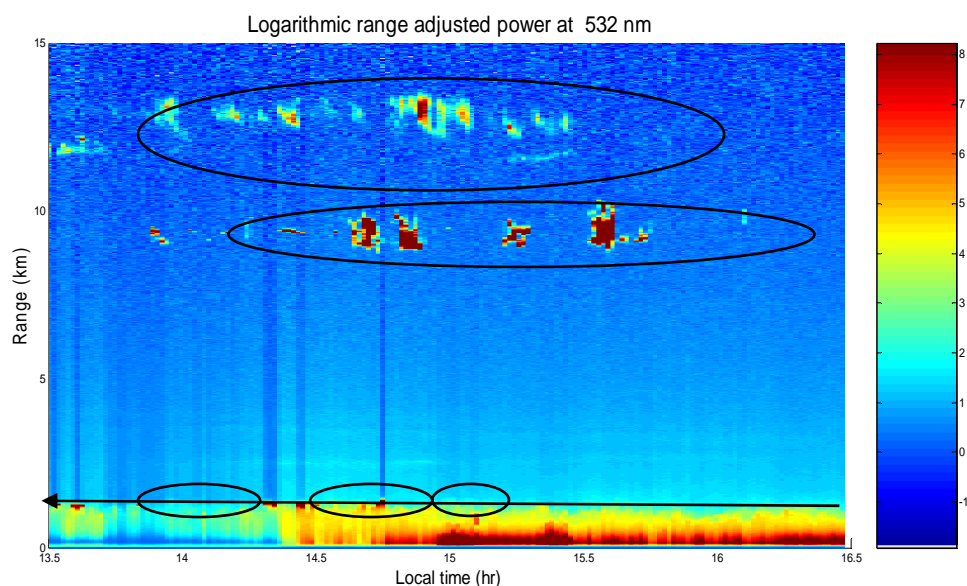
Figure 5-9 UPRM logarithmic range corrected power image at 532nm on 24 of March 2009 in the time interval of 1:30PM to 4:30PM, where the clouds are localized using circle marks.

Cirrus clouds in the upper Troposphere and in the Tropopause region will be studied in this section using the 1200 shot file collected at 2:41PM. Fig. 5-10 shows the optical properties (α and β) of the clouds in the upper tropospheric region. Lidar ratio, L_{aer} values of 10, 15, and 30 sr were used experimentally, however, the best value for all three was selected to be 18 sr, which is in the recommended range of 10 to 20 sr for clouds in general [25]. The Å exponent in the cloud region is less than zero, as shown in Fig. 5-10 c. This corresponds to particles in the region immigrating from *Fine mode* (*Aitken* and *Accumulation mode*) to *Coarse mode*. Between the two clouds the Å is close to 3, indicating the presence of small particles.
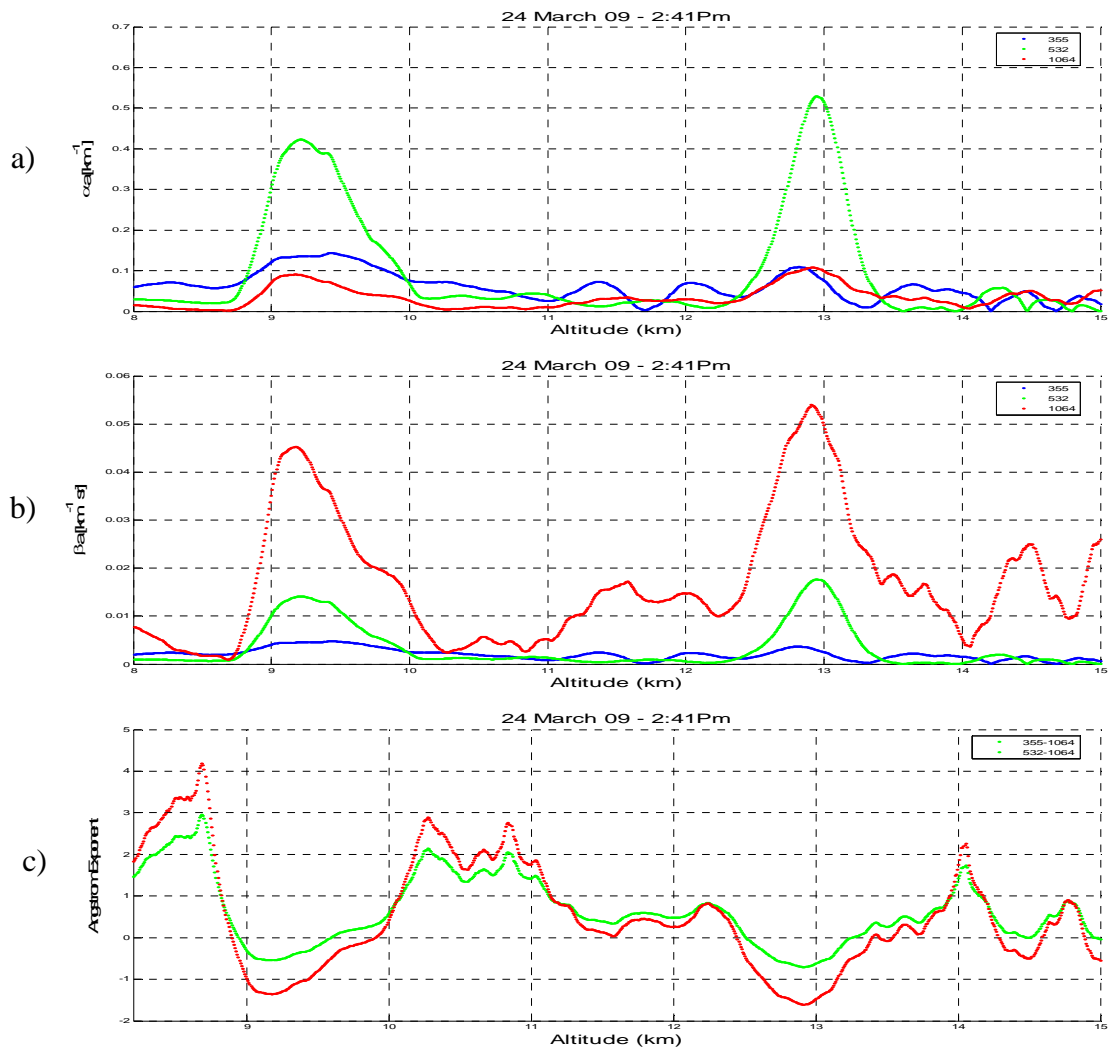
Figure 5-10 α_{aer} (a) and β_{aer} (b) coefficients at the three wavelengths (Blue-355nm, Green-532, and Red-1064nm) using the Klett & Fernald inversion method in the upper troposphere region where cirrus clouds are located, and Å coefficient (c) using the wavelength combination of 355/1064 (green), and 532/1064 (red).

The contrail geometrical depth is estimated around 1.4 km for the cirrus cloud present at 9 km. For the cirrus cloud at 13 km, the contrail depth is close to 1 km. These geometric

depths are in accordance with the cloud formation classification presented in section 2.4: the cirrus clouds close to 9km are classified as Middle Tropospheric, and the cirrus clouds close to 13km are under the Tropopause group.

The microphysical parameter properties based on the regulation inversion methods (see Chapter 3) for spherical particles are determined for the Middle Tropospheric and Tropopause cirrus clouds. In these simulations the particle sizes are defined by *accumulation mode* and *coarse mode*s. The microphysical parameters for the Middle Tropospheric cirrus cloud is presented in Table 5-5 and the ASD distributions for the same are shown in Fig. 5-11 & 5-12. In Fig. 5-11, the maximum number of concentration is for aerosols between 1.4 & 1.8µm (Figure 5-11 a), the maximum surface-area is for aerosols in the range of 0.9-1.6 µm (Figure 5-11 b), and the maximum volume is for aerosols from 0.6 up to 0.9 µm (Figure 5-11 c). In Fig. 5-12, the maximum concentration is for aerosols with radius of 9µm (Figure 5-12 a), the maximum area is for aerosols with a radius of 5.5µm (Figure 5-12 b), and the maximum volume is for aerosol with a radius of 2µm (Figure 5-12 c). In the case of Tropopause cirrus cloud, the microphysical parameters are in the Table 5-6, and the ASDs are shown in Fig. 5-13 & 5-14. Fig. 5-13 a) illustrate aerosol with a radius of 1.55µm with maximum concentration, b) present aerosols in the radius interval of 1.4 to 1.7µm with maximum surface-area, and c) shows aerosols with a radius of 2µm with maximum volume. Finally, Fig. 5-14 a) the maximum concentration is for aerosols with a radius between 1.7 and 1.8µm, b) aerosols between 1.5 and 1.6µm have maximum surface-area, and c) aerosols of 2µm have the maximum volume.

Middle Tropospheric cirrus cloud at 9km				
	n_t (cm-^{3})	r_{eff} (µm)	a_t (µm^2/cm^3)	v_t (µm^3/cm^3)
Accumulation Mode	40	1.3	12.3	5.1
Coarse Mode	410	5.9	37.5	7.4

Table 5-5 Microphysical parameters of the Middle Tropospheric cirrus cloud.

Tropopause cirrus cloud at 13km				
	n_t (cm-^{3})	r_{eff} (µm)	a_t (µm^2/cm^3)	v_t (µm^3/cm^3)
Accumulation Mode	51	1.3	15.7	6.6
Coarse Mode	530	5.9	46.9	9.3

Table 5-6 Microphysical parameters of the Tropopause cirrus cloud.

Comparing the results obtained in both clouds in terms of microphysics it is demonstrated that the particle size tends to increase in clouds. The Å coefficient plot helps us obtain an idea about the sizes of particles present in the Troposphere. Though there are particles of different sizes present in clouds formed by aerosols that immigrate from smaller to larger sizes, the microphysics parameters demonstrate that larger particles dominate in terms of number of particles in clouds.
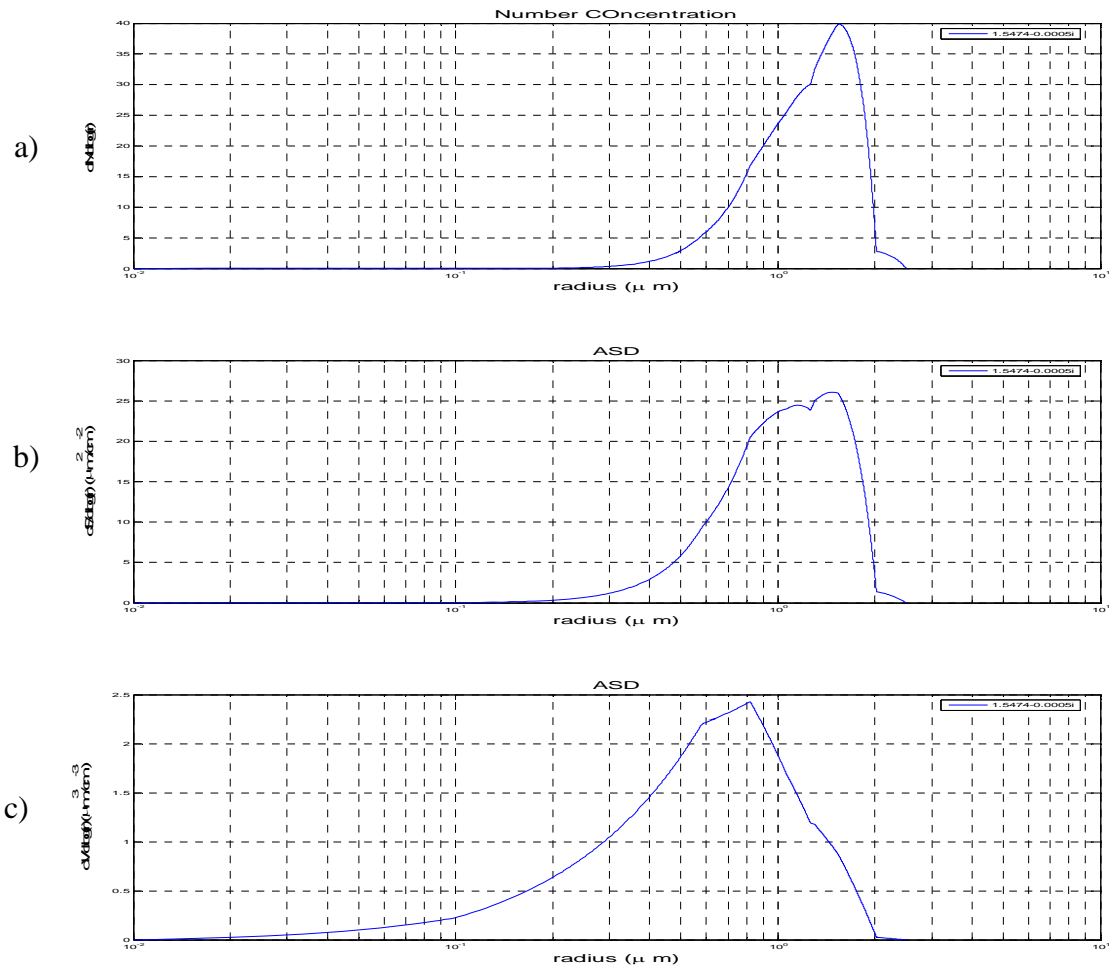
Figure 5-11 Middle Tropospheric cirrus *Accumulation mode* ASD in terms of number concentration (a), surface-area (b), and surface-volume (c).
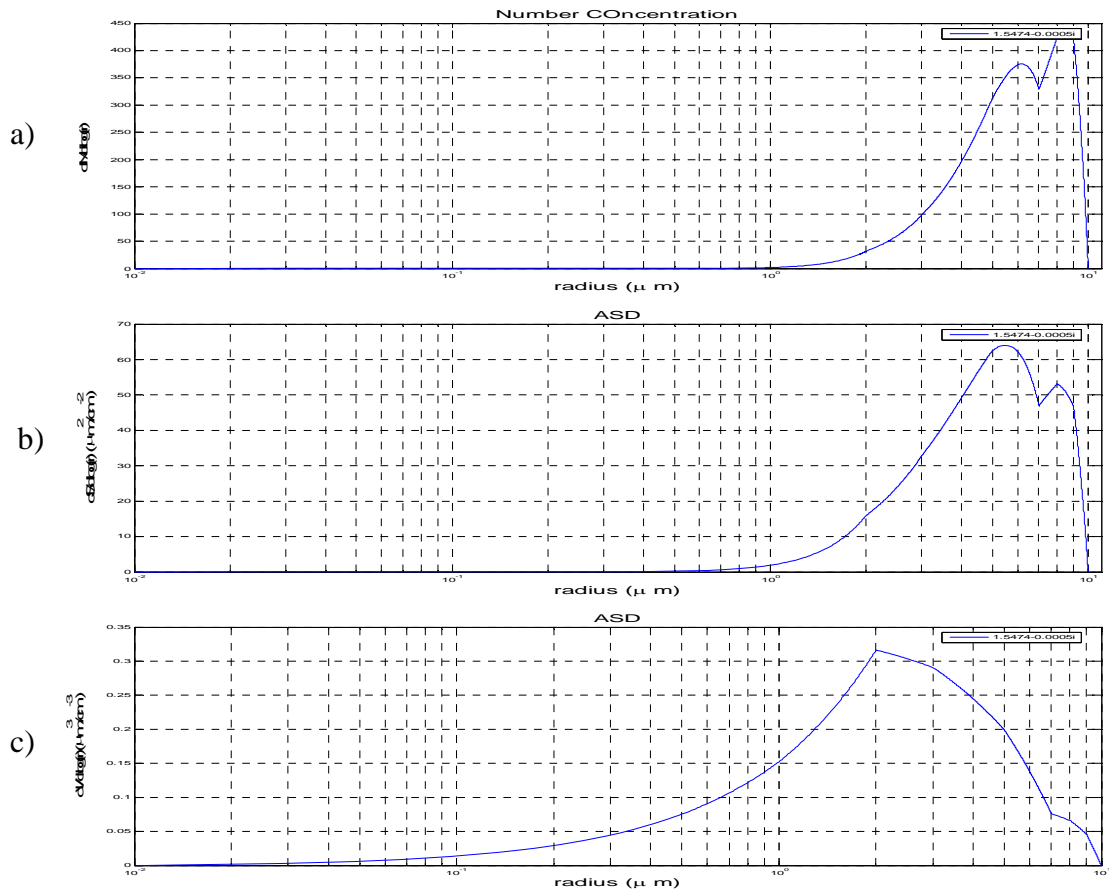
Figure 5-12 Middle Tropospheric cirrus *Coarse mode* ASD in terms of number concentration (a), surface-area (b), and surface-volume (b).

83
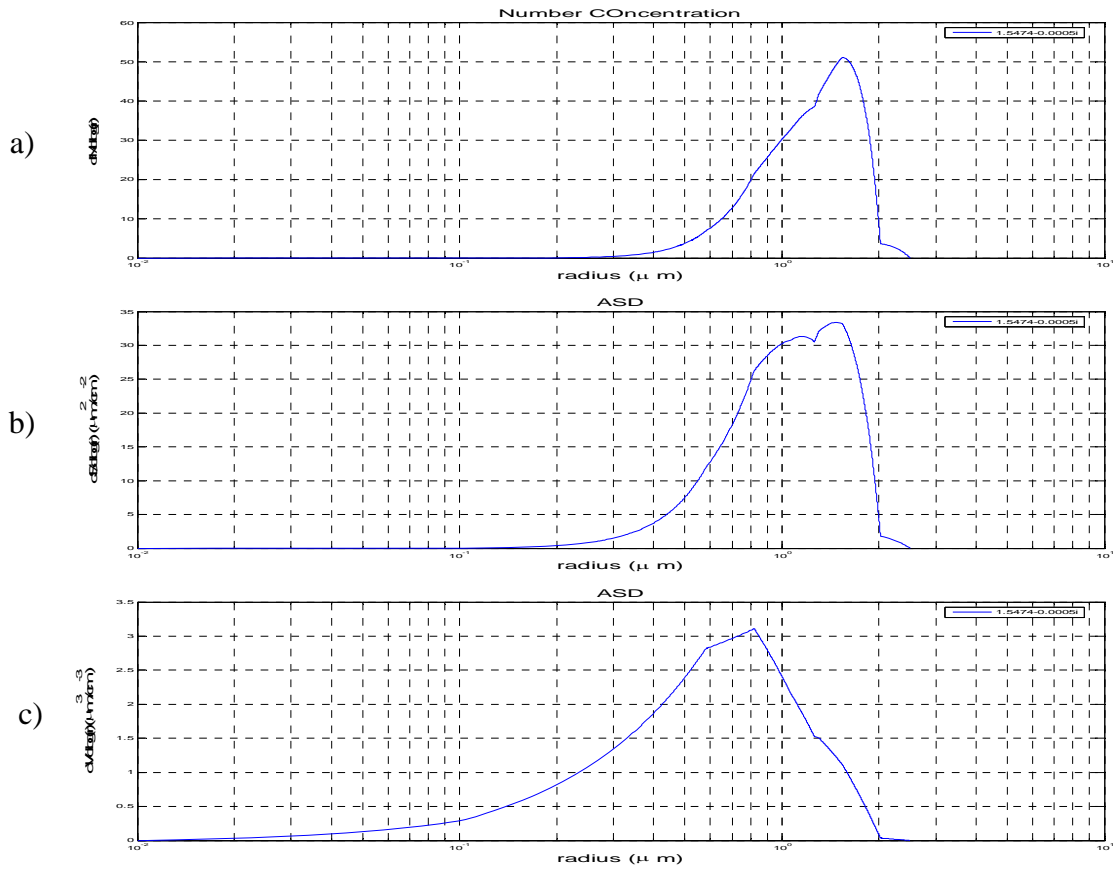
Figure 5-13 Tropopause cirrus clouds *Accumulation mode* ASD in terms of number concentration (a), surface-area (b), and surface-volume (c).
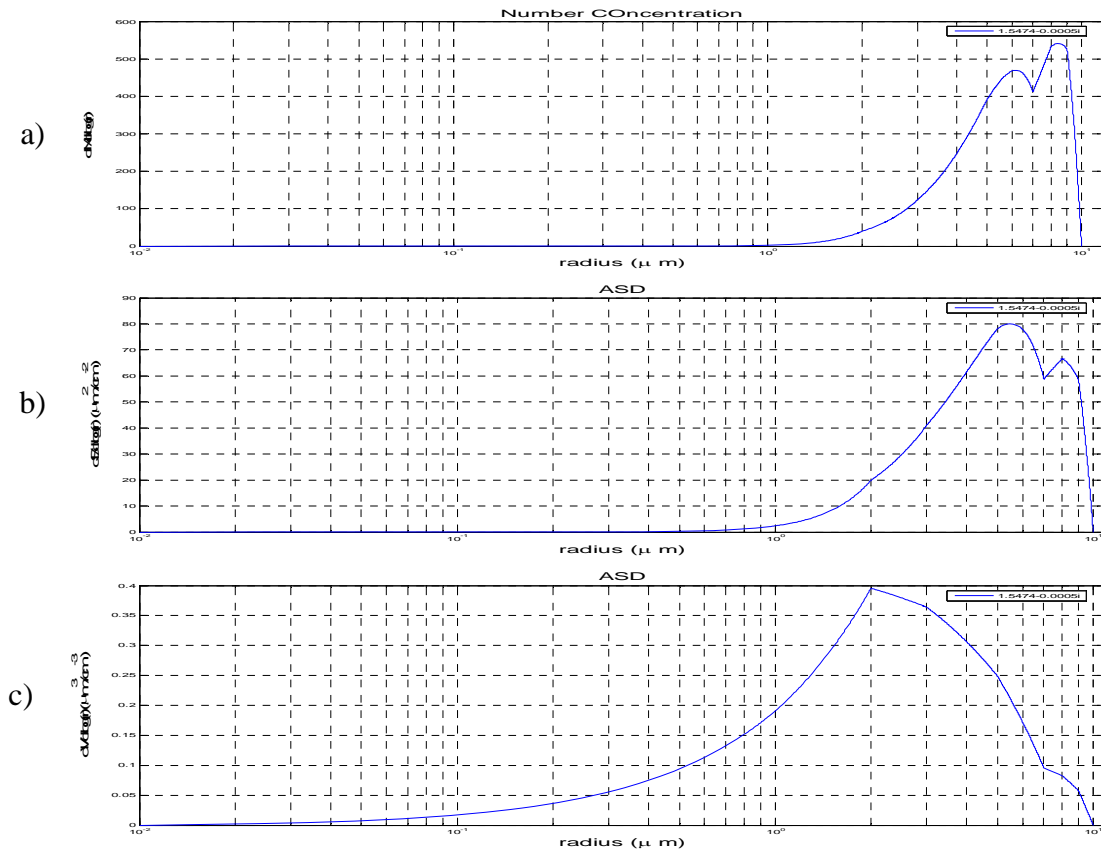
Figure 5-14 Tropopause cirrus clouds *Coarse mode* ASD in terms of number concentration, surface-area, and surface-volume.

In summary, the previous analysis affirms that the analyzed cirrus clouds contain a high amount of relatively bigger particles that can be a combination of water and ice particles. It is important to consider that the values obtained are based on Mie theory for spherical particles. It is known that particles of different sizes are present in the clouds and suspended in the atmosphere, but the shape determination is possible only using depolarization channels. The effect of multiple scattering within the cloud is not considered because it is negligible for the FOV of UPRM and CCNY Lidar telescope. The multiple

scattering is not considered in this research, and this issue not affects our results because our detections units only detect the polarization of 180^0.

5.2.2 CCNY-Lidar Algorithm Results & Discussion

The Lidar methodology presented in this section will be based on Raman approach for determining the parameters of β_{aer} and α_{aer} coefficients, L_{aer} for cirrus clouds, Q_{H2O} (water vapor missing ratio), and RH (relative humidity).

5.2.2.1 Cirrus clouds detection

The cirrus cloud study shown here was based on the CCNY-Lidar data to demonstrate the determination of the optical properties using the combination of 355nm as the fundamental wavelength and 387nm as the Raman wavelength. The 387nm signal is used since it can detect the cirrus clouds while the 407nm was attenuated at lower altitudes in the CCNY Lidar data.

Fig. 5-15 shows the logarithmic range corrected power image at 532nm for 8 hours of data collection in NYC on May 23rd 2007. A cirrus cloud typology may be defined based on the simple analysis of range corrected Lidar signals, which provides information about optical depth, clouds height, and temporal change. The type of clouds can also be classified by observing the range corrected power images.

Logarithmic range adjusted power at 532 nm
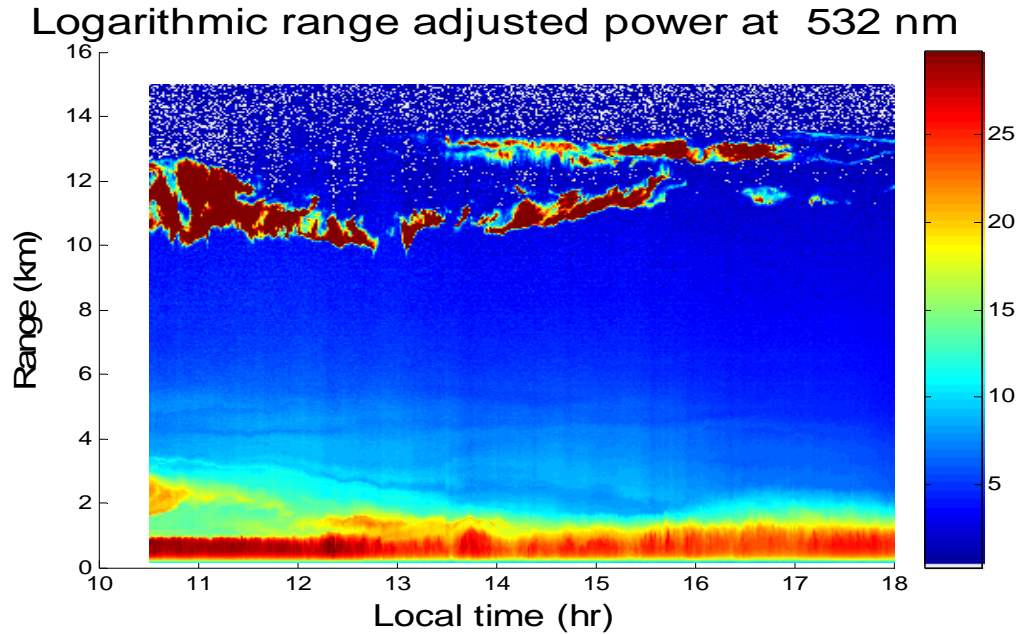
Figure 5-15 Logarithmic range adjusted power image at 532nm. In this image the clouds, aerosol layers, and NYC PBL can be appreciated in the first 3km.

The main advantage of the Raman-Mie combination techniques for cirrus cloud studies is to solve the limitation of the elastic-Lidar inversion technique arising from having to use the *a priori* value of L_{aer}. Instead, the Raman signal is used to estimate α_{aer} coefficient. The α_{aer} coefficient values can be determined using the CCNY-Lidar data at the 387 nm. The mathematic methodology used in this section is discussed in Chapter 3. Only the optical properties at 355nm can be calculated using this methodology, because the two Raman channels installed at CCNY-Lidar are inelastic channels of 355nm. In the case of cirrus clouds, it is assumed that β_a coefficient is wavelength dependent. Thus the β_a may be retrieved without using the L_{aer} assumption. At the same time, this procedure allows the direct determination of the L_{aer}. The L_{aer} values can be used when the Raman signal is not

available for similar cloud or aerosol layers. In Fig. 5-16, an example of the application of the aforementioned methodology at 355nm is presented. In addition, the optical properties (β_{aer} and α_{aer} coefficients) and the L_{aer} coefficient is obtained.

The L_{aer} ranges from 25sr to 20sr in the free cloud region, and from 10 to 20sr in the region occupied by cirrus clouds.
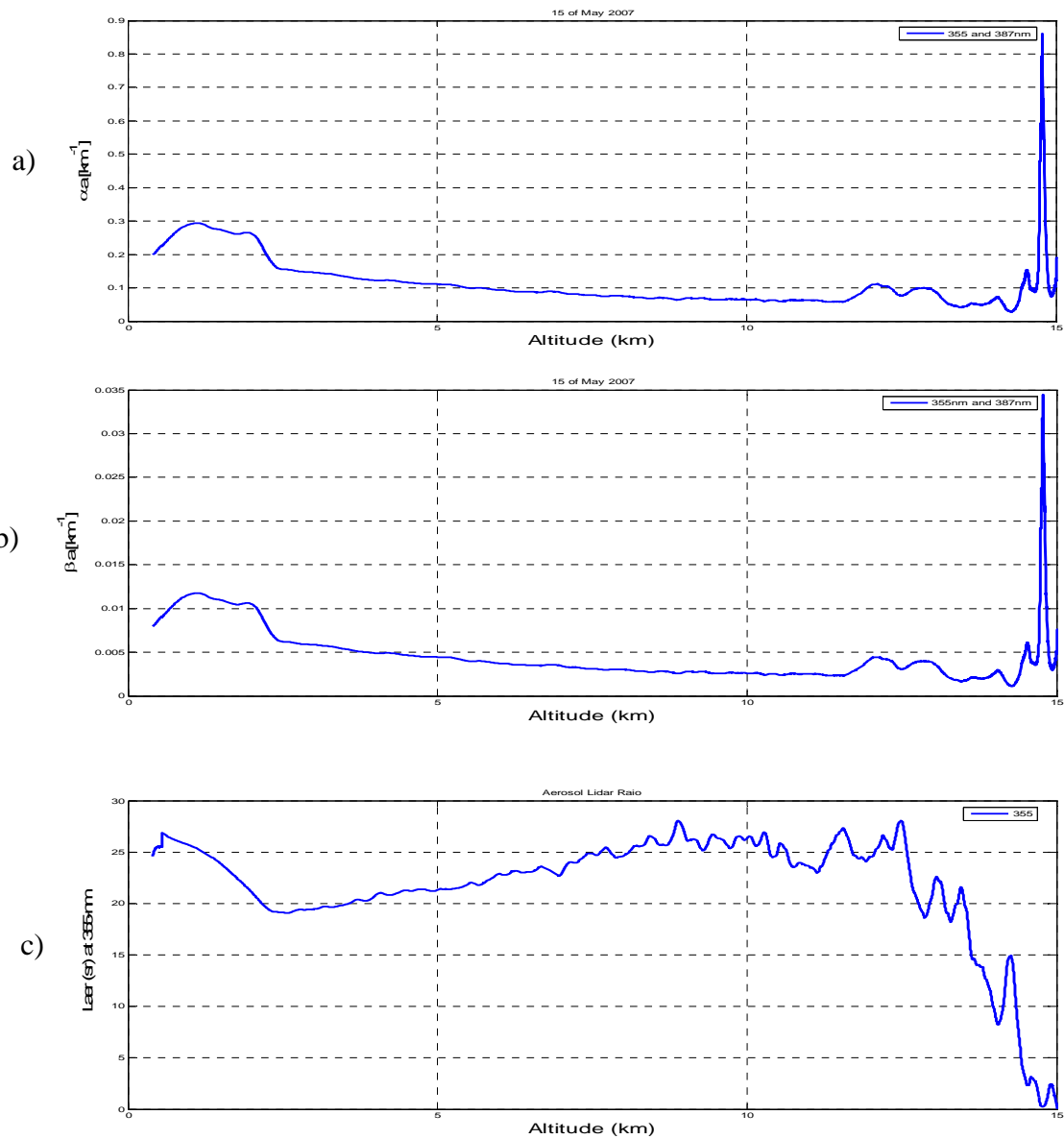
Figure 5-16 α_{aer} (a) and β_{aer} (b) coefficient at 355nm using the combination of 355nm and 387nm wavelengths, and L_{aer} (c) coefficient at 355nm.

The calculation of α_{aer} utilizing the Raman signal involves many sources of error: statistical errors occasioned by signal detection, systematic errors due to the estimation of the temperature and pressure profiles based on ASA76 to determine the β_{mol} and α_{mol} coefficients, multiple-scattering effects, and high smoothing of the Raman raw signals. From the error analysis presented in [57], it can be concluded that the Raman errors are very complex and have significant values. Since [57] the errors occasioned by detection can reach up to 10% at the top of the Troposphere or in the Tropopause altitudes (close to 15km). The advantage of using Raman signals is that the L_{aer} profile can be calculated, while using Mie signals the L_{aer} is a constant which is estimated using the Lidar and AERONET, or a portable sun-photometer, using AOD matching concept.

5.2.2.2 Water vapor mixing ratio (q$_{H2O}$) profile and Results

The implemented algorithm takes the ratio of the two Raman (387 and 407nm) signals to determine the q$_{H2O}$. First, the background noise is eliminated and the signals are range corrected. Then the result is filtered to eliminate the noise occasioned by the detection process and the sensor sensitivity. Finally, the ratio of the q$_{H2O}$ is obtained using the ratio of the two signals (P_{407nm}/P_{387nm}). WV is calculated by $Q_{H2O} = C * (P_{407nm}/P_{387nm})$, where C is the calibration constant, see section 3.8. To estimate the calibration constant dry air density parameter, ρ_{da}, is needed which can be determined using ASA76, or the value retrieved from *radiosound*. The result is integrated over the column and then compared with the column

WV product reported by AERONET to calculate the calibration constant. The block diagram of the implemented algorithm is presented in Fig. 5-17.
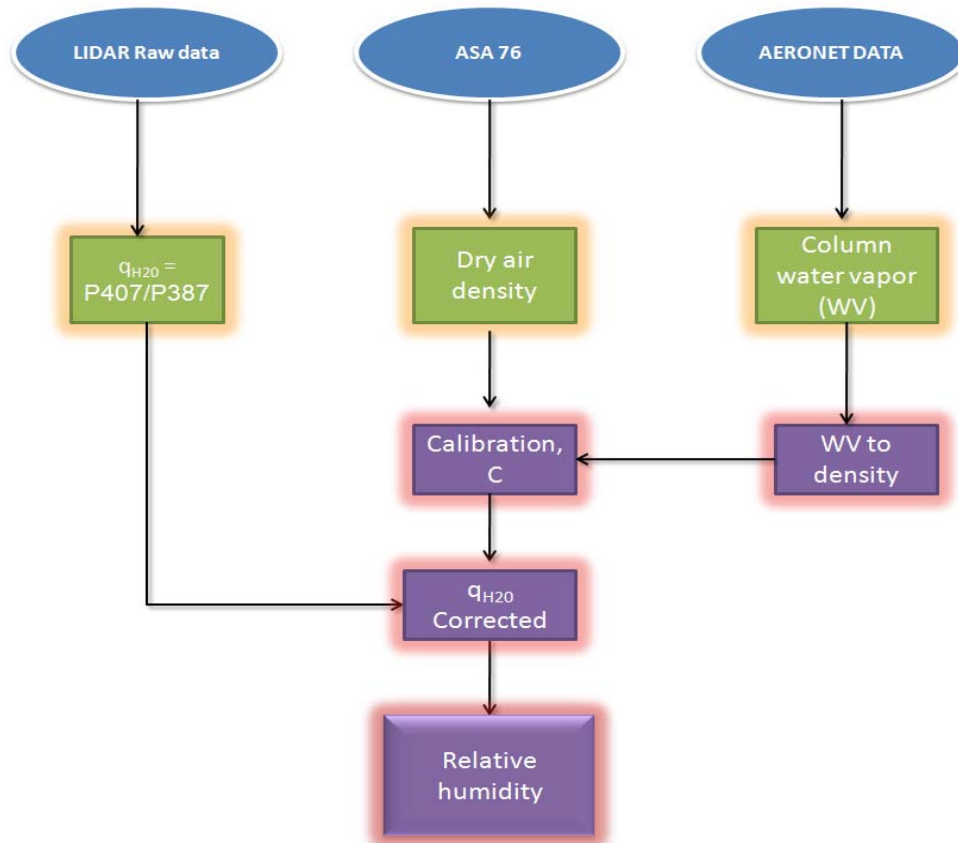
Figure 5-17 Block diagram of the Raman-Lidar technique for the determination of q_{H2O} and RH.

The data from CCNY Raman-Lidar acquired on May 23rd, 2007 are used to obtain q_{H2O} results using the algorithm developed in MatLab. The results obtained directly from the ratio of the two corrected and filtered signals are presented in Fig. 5-18. This WV measurement is obtained using the 9:41PM power profiles with the vertical resolution of

3.75m. The aforementioned calibration constant is calculated using two different methods [44], using, 1) *in situ* column water vapor constant obtained from AERONET and a reference altitude, and 2) a reference altitude interval. The calibration constant depends on the dry air density (ρ_{da}) profile which can be estimated using either the ASA profiles of temperature and pressure or a *radiosond* results. The results obtained from the two mentioned methods are presented in this work to demonstrate the effectiveness of each one.
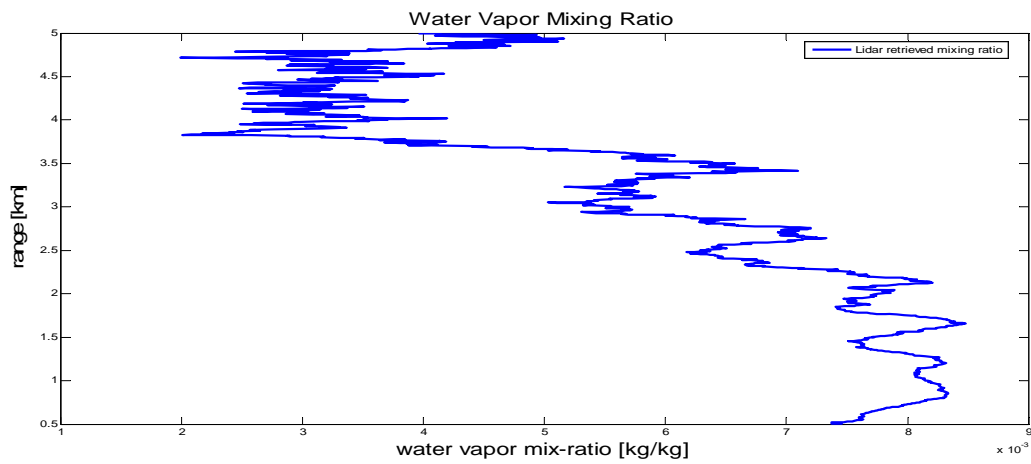
Figure 5-18 q_{H2O} profile based on the ratio of the two signals of 407nm/387nm.

The mathematical concepts of the two methods used to calculate the calibration constants were shown in Chapter 3, where the determinations of few parameters are very complex to calculate. The column WV value taken from AERONET is equal to 2.59cm, this value is converted to water density (kg/m^2) using the conversion factor of 1cm = 9.9226kg/m^2. The q_{H2O} presented in Fig. 5-18 is multiplied by the ρ_{da} calculated using ASA76 or a *radiosound* and then is integrated within the assumed reference altitude obtaining a reference WV (WV_{reff}) and the complete column for WV (W_{tot}). Taking the ratio

91

of W_{reff}/ W_{tot} estimates the fraction of water presented in the column. Then, the calibration constant is obtained by the ratio of the AERONET column water density over the estimated column water fraction. Finally, the Q_{H2O} (corrected q_{H2O}) is given by the multiplication of the calibration constant (C) and the q_{H2O} (not corrected). The mentioned methodology to determine the calibration constant is known as Technique 1 [44].

A second method is used to compute the calibration constant by taking an altitude interval as a reference and computes the average of q_{H2O}. The altitude interval is chosen at lower altitudes where the WV and nitrogen signals have excellent power intensity. Finally, the Q_{H2O} (corrected q_{H2O}) is given by the multiplication of the calibration constant and the q_{H2O} (not corrected). The mentioned methodology to determine the calibration constant is known as Technique 2 [44].

Fig. 5-19 shows the results obtained using Technique 1 &2 (blue and green plots) and are compared with the results reported by a *radiosound* launched at 8:00Pm. The Fig 5-19 (a) illustrate water vapor ratio results when the ASA76 profiles of temperature and pressure were used to estimate the profile of ρ_{da}, meanwhile Fig 5-19 (b) calculates the Q_{H2O} profile using the *radiosound* profiles of temperature and pressure to determine the ρ_{da}.
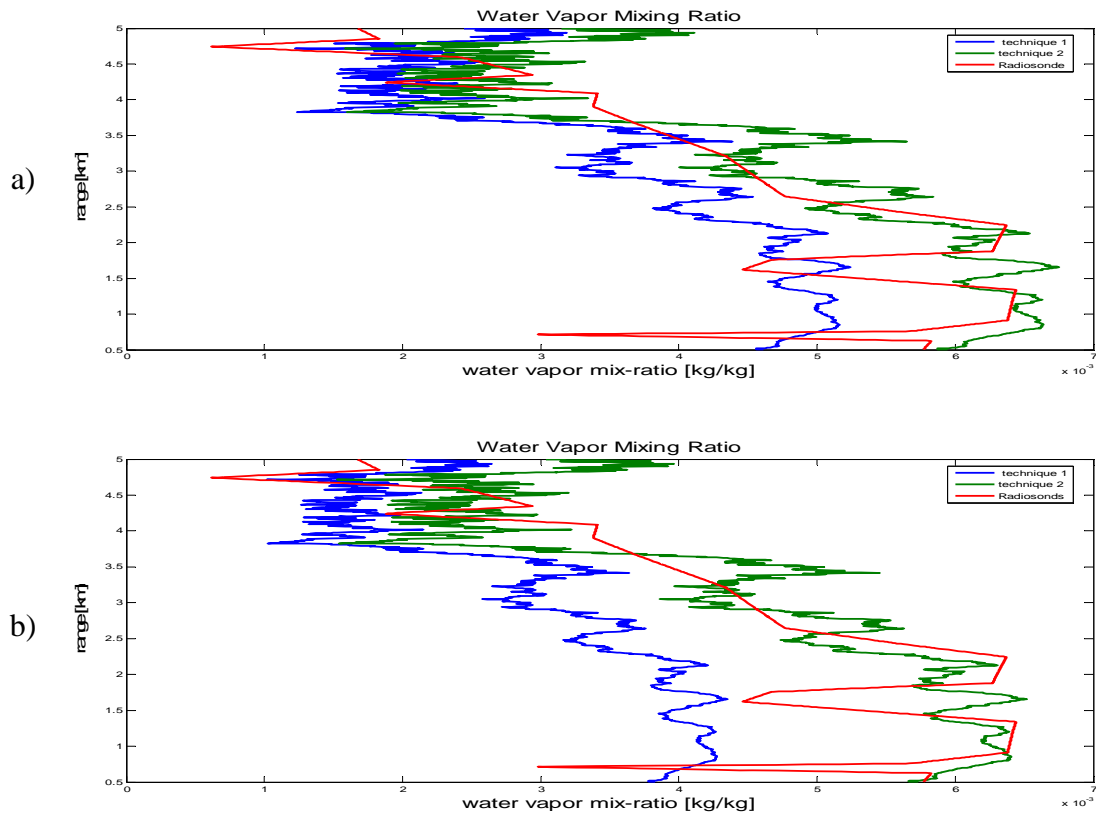
Figure 5-19 Q_{H2O} profile based on Technique 1 (blue) and Technique 2 (green). The red plot is the water vapor mixing ratio given by a *radiosound*.

5.2.2.3 Relative Humidity (RH) estimation

To estimate the RH using the Raman-Lidar signals is needed the Q_{H2O}, the saturation vapor pressure (P_{sv}) in hPa, and vapor partial pressure (P_{vp}). The calculation of the P_{sv} was bases on Magnus formula [58] which is very common used in meteorology. The temperature and pressure profiles can be used from ASA76 or *radiosound* to determine the estimation of the P_{sv} and P_{vp}. The mathematical concepts of RH calculation are presented in Chapter 3.

Fig 5-20 shows the results obtained using the Q_{H2O} presented in Fig. 5-19 to estimate the RH. Based on the obtained results, the estimation of pressure and temperature profile

using ASA76 (Fig. 5-20 a) generates error in the estimation of RH in comparison with the results obtained using the *radiosound* temperature and pressure profiles (Fig. 5-20 b). The results in Fig. 5-20 b) are very close to the RH reported by the radiosound. Determine the correct result here is very difficult because the radiosounds have problem in the data collection caused by the wind direction. In the other hand, the ASA76 also generates errors because the cold/warm air currents are not considered. Also, the Lidar system and the local radiosound are few km apart. Fig. 5-21 shows the difference in temperature profiles obtained by ASA76 and a radiosund. To determine the correct result here is recommended determine the temperature profiles using the Lidar itself. The problem is that the required filter to measure temperature in Lidar systems is very expensive.

The results obtained using the Technique 2 to compute the calibration constant (C) is more approximate to the results obtained by Technique 1.

a)

b)
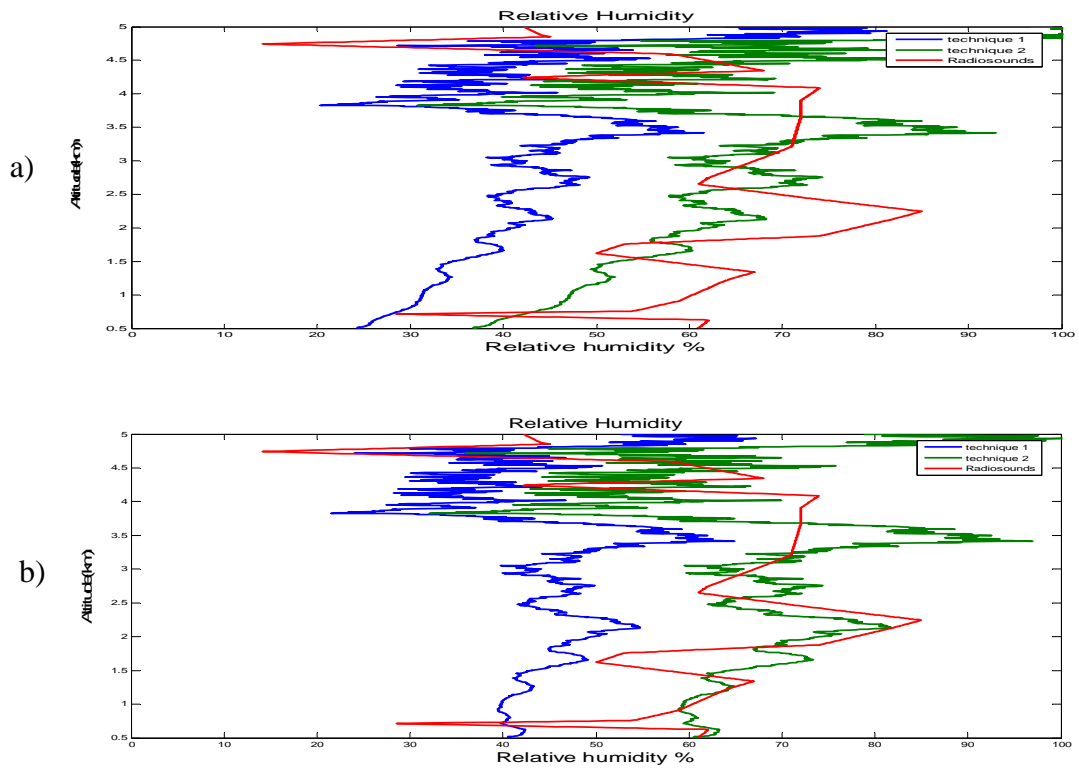
Figure 5-20 RH profile based on Technique 1 (blue) and Technique 2 (green). The red plot

is the RH profile given from a local *radiosound*.
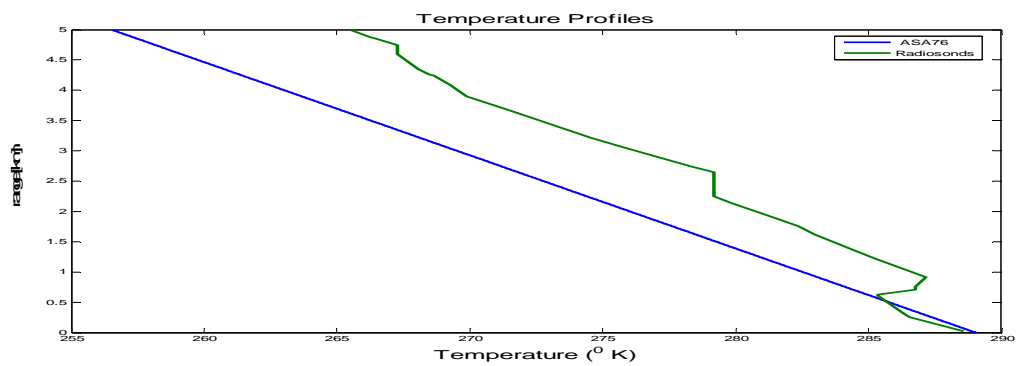
Figure 5-21 Temperature profiles based on ASA76 (blue) and Radiosound (green).

5.3   Algorithm Validation and Recommendations

This section present the α_{aer} and β_{aer} coefficients and AOD solutions based on the Elastic channel of 532nm. The Lidar data used in this validation is from CCNY-Lidar system collected on Sept. 6, 2007. This data was processed by Yonghua Wu from CCNY-Lidar staff and their result has given in numerical form. The same data was processed using the developed algorithm in this research and has been compared with Wu's results, Fig. 5-22 shows the results obtained at UPRM (blue plots) and CCNY (green plots).
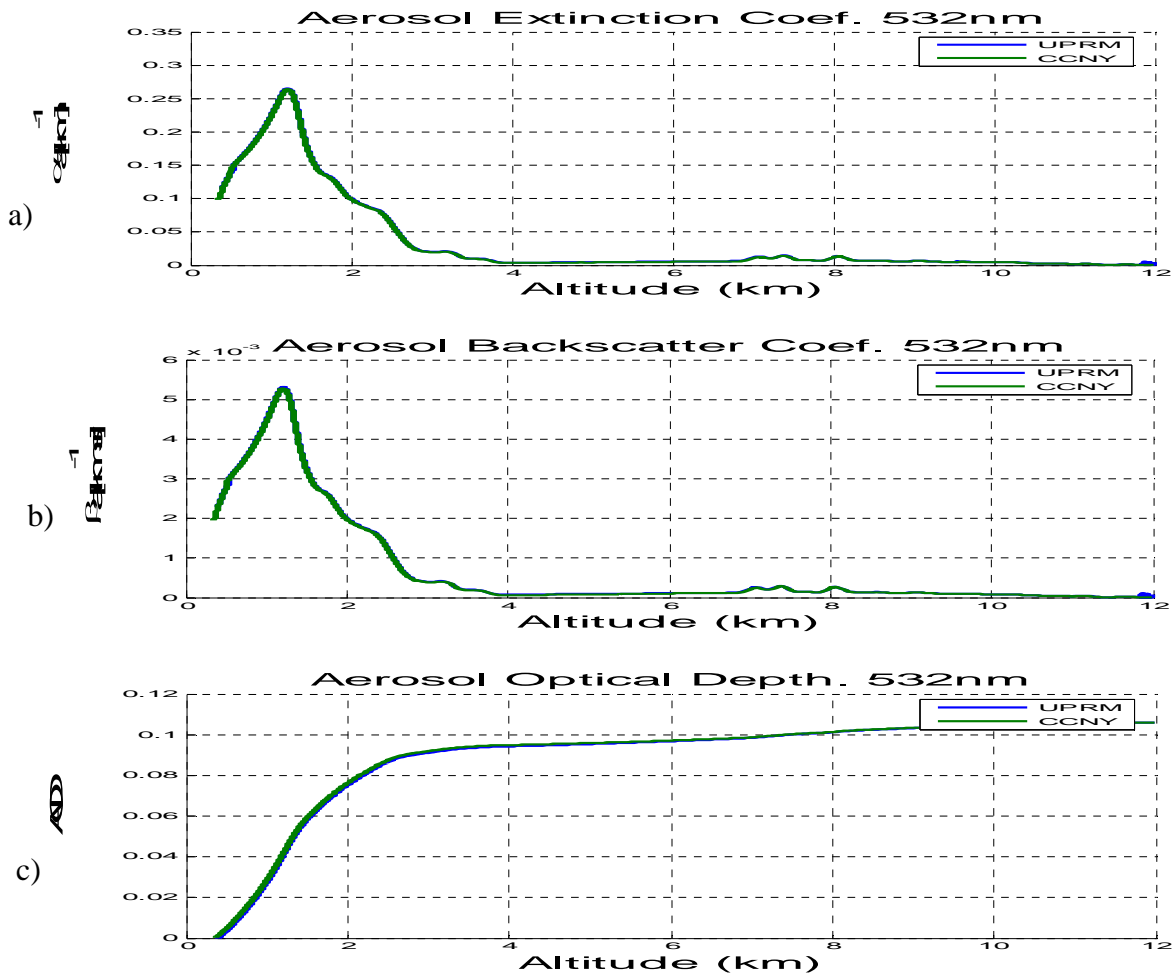
Figure 5-22 α_{aer} and β_{aer} coefficients, and AOD at the 532nm.

The results presented in previous Fig. are calculated using L_{aer} = 50sr, where the presence of aerosol is considered. The maximum percentages of error obtained in this comparison are given in Table 5-7, where the maximum error is 5% in the α_{aer} calculation. Table 5-8 shows the total column AOD values comparison, where the percent of error is very acceptable.

Errors at 532nm with L_a =50sr	
α_a	5.0
β_a	4.33
AOD	0.503

Table 5-7 UPRM and CCNY results comparison for α_{aer} and β_{aer} coefficient, and AOD plots.

Total column AOD at 532nm		
UPRM	**CCNY**	**Error**
0.1057	0.1060	0.3

Table 5-8 UPRM and CCNY total column AOD comparison.

In this research is assumed that the CCNY results are correct based on their Lidar experience and their algorithm has been validate with Hampton University algorithms.

The developed algorithms in this research were based on Klett and Fernald assumptions for elastic and inelastic lidar signals. Two different algorithms have been created for Elastic and Inelastic signals. The UPRM-Lidar system only operates for elastics signals, where the received wavelengths are the same as the transmitted wavelengths (355, 532, and 1064nm). The elastic Lidar equation inversion solution depends of *a priori* values, for example, L_{aer} and a reference altitude (R_0). The problem with the used *a priori* values is in the L_{aer}, which is assumed constant. In a real atmosphere, this value depends on the

atmospheric conditions and the presented events (Saharan dust, volcano ash, etc.). With this assumption, the Elastic-Lidar inversion algorithm generates errors in the α_{aer} coefficient calculation. These errors are considered theoretically less than 15%, because in some occasions L_{aer} varies between one numbers during clear days. High percent of errors are in high turbid atmospheres where are: different aerosol, smoke, dust, ash, and etc, layers which are not considered and L_{aer} is used as *a priori* values. The determination of β_{aer} has percent of error less than 5%, because this parameter only depends on R_0. In the Elastic inversion algorithm, R_0 is choosing at high altitudes where aerosols are not considered and molecules are considered.

The Inelastic inversion method depends on the transmitted and received signals wavelengths. This methodology is based on the rotational-vibrational wavelength shift. In common Lidar systems are used the Raman channels of nitrogen and WV to determine the q_{H2O} and aerosol optical parameters (α_{aer} and β_{aer} coefficients). To determine the aerosol optical data at the same wavelengths (nitrogen and WV) as the UPRM-Lidar systems is needed the implementation of Raman channels at 355 and 532nm. The most Raman channels used for 355nm are the 387 (nitrogen) and 407nm (WV), and the most used for 532nm is the 407 (nitrogen). The solutions for the aerosol optical parameters depend on the received intensity at the Raman channels. This inversion method has problem with the estimation of β_{aer} coefficient, because it depends of few assumptions needed to obtain the solution of it. Eq. 3.23 shows the inversion solution of β_{aer}, where the number density (N) is very complex to estimate for WV or nitrogen. The N estimation in this solution can generate errors larger than 20% (theoretically).

The calculation of α_{aer} using the inelastic methodology generates errors considered theoretically less than 5%. For this reason is recommended the combination of Elastic-Inelastic signals to proceed with the aerosol characterization process. Decrease the percent of error in the Lidar inversion solutions is very important to obtain the most wanted results about the aerosol and other atmospheric constituents. Other works use the combination of β_{aer} at the three fundamental wavelengths (Elastic signals) and α_{aer} at the two operational wavelengths that has Raman channel (typically 355 and 532nm) to determine the ASD parameter. This combination generated errors less that 5% in the calculation of ASD and aerosol microphysical parameters.

5.4   Conclusion

Two state of the art Lidar systems are installed in UPRM and in CCNY with the capacity to determine atmospheric optical properties. A statistical analysis of the measurements of one day in UPRM- Lidar was presented in this work, also the comparisons of AOD values between UPRM-Lidar and AERONET in La Parguera show a good and realistic agreement in both systems that permit us study the particles suspended in the atmosphere. The aerosol and cloud microphysics parameters were calculated based on the α_a and β_a coefficient over the 1200shot file per minute to reveals the sizes distributions in terms of number concentration, surface-area, and volume as well the SSA coefficient of the aerosol present in the troposphere.

A Lidar characterization of cirrus clouds was presented with examples of application of Mie-Raman combined techniques and Mie technique for the determination of cirrus optical properties. The effort to monitoring clouds, aerosols, smoke, dust, etc at the UPRM-Lidar laboratory may be continued in the future obtaining more conclusions and predictions based on different measurement made during years.

In this project the ratio of the Raman wavelength at 407nm for WV and 387nm for nitrogen, are used to derive the troposphere q_{H2O} as a direct measurements. The implementation of the WV retrieval procedure presented in [47] using the CCNY-Lidar system, AERONET station, and NYC local *radiosound* were fundamental issues to obtain the presented results of the developed algorithm. The Raman-Lidar is the only equipment that is able to give a high resolution water vapor during the night. The temperature and pressure profiles are very important and necessary in the calculation of calibration constant and RH. Also, the results obtained by a Lidar system can be compare with the *radiosound* because this system give the profiles of temperature, pressure, number density, q_{H2O}, and RH.

The presented results demonstrate that the Lidar is capable and viable to make statistical analysis of different parameters that may be valuable for global models and atmospheric studies in many places.

6   Conclusions and Future Work

This chapter presents the conclusions obtained from the UPRM-Lidar system to make remote sensing and from the developed algorithms based on the experimental results, and presents future work recommendations.

6.1   Conclusions

The main purpose of the presented work is the implementation of an operational multi-wavelength Lidar system at the UPRM and the analysis of the Troposphere Lidar-based measurements.   These high spatial and temporal resolution measurements concern aerosol optical properties.

The UPRM-Lidar system was designated based on CCNY-Lidar system.   The transmitter of the UPRM-Lidar is based on a Nd:YAG laser emitting at 355, 532, and 1064nm and operating repetition rate of 20Hz and energies up to 700mJ at 1064nm.   The UPRM-Lidar receiver is based on a Cassegrain 20" diameter telescope.   The receiver was designated to detect the backscatter light emitted by the laser at the same emitted wavelengths.   The corresponding Lidar signals are stored both in analog and photon-counting models via transient recorders within typically 1200 shots and 20MHz corresponding to 7.5m of vertical resolution acquisition sampling rate.

The main achieved performances of the UPRM-Lidar configuration are: good stability in operation, acceptable SNR up to the lower Stratosphere in clear days with a single acquisition file of 1200 shots, 20Hz and 700mJ at 1064nm for the elastic backscatters signals

using the 20" Cassegrain telescope, and demonstration of long-term operation capacity with some measurements since December 2008.

Based on the inversion of the Lidar elastic signals, the tropospheric aerosol backscatter and extinction coefficients were regularly determinate. A statistical and analysis of data taken in March 24th, 2009 shows good and realistic agreement, in terms of aerosol optical depth (AOD) when the aerosol lidar ratio was estimated using the AERONET station in La Parguera. A combined method based on elastic-inelastic signal is proposed, which allows the determination of the real aerosol lidar ratio without any assumption. The retrieval of contrails optical properties and preliminary calculations of its microphysics based on Mie-theory in the approximation of spherical particles is considered in this research. Typical profiles of tropospheric aerosol and cirrus clouds optical properties were obtained for one minute integration time, and 7.5m vertical resolution was also operational and it was proven its worth in distinguishing between different clouds types and aerosols layers.

The night-time water vapor mixing ratio profiles were derived using the ratio of the Lidar signals corresponding to Raman rotational-vibrational backscatter at 407nm from WV and at 387nm for Nitrogen molecules using the CCNY-Lidar data. A complete procedure including corrections and a method for calibration is implemented. The integrated profiles are in good agreement with *in situ* measurements obtained from AERONET instrument. The typical vertical profiling of the tropospheric night-time q_{H2O} ration is obtained within one minute integrated time and 200m up to 5km. The use of simultaneous temperature and pressure profiles from models and measurements makes it possible to estimate the relative humidity and in particular to identify the tropospheric super statured regions [45].

102

6.2   Future Work

As a future work is recommended:

- Implement a vertical radar system for airplanes and helicopters detection.

- Add three additional rotational-vibrational Raman Channels of 407nm (water vapor) and 387nm (nitrogen) for the transmitted signal of 355nm, and other Raman Channel of 607nm (nitrogen) for the transmitter signal of 532nm.

- Measure temperature profiles using the Lidar.

- Add depolarization channels almost for 532nm.

- Implemented the algorithms in GUI form.

- Apply image processing in the logarithmic range adjusted image for particle classification purposes.

- Continue with algorithm development to calculate other parameters that are very important to study the aerosols and their positive and negative impact with the different atmospheric processes.

- Continue with the Calipso satellite validation.

APPENDIX A   Aerosol Backscatter and Extinction

This Appendix shows the β and α coefficient solution, starting from the Elastic Lidar equation presented in Chapter 3, eq. 3.2. To simplify the determination of $\beta_{aer}(R)$ and $\alpha_{aer}(R)$, we will assume L_{aer} as a constant [37]. Now, we can write the lidar equation in terms of the range adjusted power signal ($S(R) = R^2 P(R)$). The complete range adjusted or range corrected is given by eq. A.1.

$$S(R) = E_0 \eta_0 [\beta_{aer}(R) + \beta_{mol}(R)] Exp\left[-2\int_0^R [\alpha_{aer}(R) + \alpha_{mol}(R)]dr \right] \quad \text{A.1}$$

Where, α and β are composed of molecules and aerosols, eq. A.2 & A.3.

$$\beta(R) = \beta_{aer}(R) + \beta_{mol}(R) \qquad \text{A.2}$$

$$\alpha(R) = \alpha_{aer}(R) + \alpha_{mol}(R) \qquad \text{A.3}$$

Now, let introduce the L_a equation given by eq. A.4.

$$L_{aer} = \frac{\alpha_{aer}(R)}{\beta_{aer}(R)} \quad \text{A.4}$$

 Using this relation between α and β presented in the previous equation, eq. A.1 can be rewrite in terms of β. But, first we need to work in the expression inside of the integral part. Eq. A.5 shows α coefficient in terms of β. This combination helps us to obtain one equation and one unknown variable, because originally the equation depends of two unknown variables.

$$\alpha_{aer}(R) + \alpha_{mol}(R) = L_{aer}\beta_{aer}(R) + L_{mol}\beta_{mol}(R) \quad \text{A.5}$$

Then, eq. A.5 can be substituted into eq. A.1, obtaining the following (eq. A.6).

$$S(R) = E_0\eta_0[\beta_{aer}(R) + \beta_{mol}(R)]Exp\left[-2\int_0^R [L_{aer}\beta_{aer}(R) + L_{mol}\beta_{mol}(R)]dr\right] \quad \text{A.6}$$

Adding the term $L_{aer}\beta_{mol}(R) - L_{aer}\beta_{mol}(R)$ inside of the integral in the exponential function

of eq. A.6 is obtained the following equation, which is used to simplify the Elastic Lidar

inversion solution presented with Klett.

$$S(R) = E_0\eta_0[\beta_{aer}(R) + \beta_{mol}(R)]Exp\left[-2\int_0^R [L_{aer}\beta_{aer}(R) + L_{mol}\beta_{mol}(R) + L_{aer}\beta_{mol}(R) + L_{aer}\beta_{mol}(R)]dr\right]$$

A.7

Then, the factorization of the terms inside of the exponential function is manipulate to obtain

the function Y(R) given by eq. A.8, and the terms that do not form part of Y(R) can be

passed to the left side of the equation A.7, see eq. A.9.

$$Y(R) = L_{aer}[\beta_{aer}(R) + \beta_{mol}(R)] \quad \text{A.8}$$

$$S(R)Exp\left[-2\int_0^R \beta_{mol}(R)[L_{aer} - L_{mol}]dr\right] = E_0\eta_0[\beta_{aer}(R) + \beta_{mol}(R)]Exp\left[-2\int_0^R L_{aer}[\beta_{aer}(R) + \beta_{mol}(R)]dr\right]$$

A.9

Substituting Y(r) and multiplying in both sides by L_{aer} in eq. A.9, A.10 is obtained.

$$S(R)L_{aer}Exp\left[-2\int_0^R \beta_{mol}(R)[L_{aer} - L_{mol}]dr\right] = E_0\eta_0Y(R)Exp\left[-2\int_0^R Y(r)dr\right] \quad \text{A.10}$$

Since, L_{aer} and L_{mol} are constants, eq. A.10 can be expressed by the following equation

where the mentioned terms can be rewrite outside of the integral.

$$S(R)L_{aer}Exp\left[-2[L_{aer}-L_{mol}]\int_0^R \beta_{mol}(R)dr\right]=E_0\eta_0 Y(R)Exp\left[-2\int_0^R Y(R)dr\right]$$

A.11

Then, is applied the natural logarithm in both sides of eq. A.11, and leads to eqs. A.15 & A.16:

$$\ln\left\{S(R)L_{aer}Exp\left[-2[L_{aer}+L_{mol}]\int_0^R \beta_{mol}(r)dr\right]\right\}=\ln\left\{E_0\eta_0 Y(R)Exp\left[-2\int_0^R Y(r)dr\right]\right\}$$

A.15

$$\ln\{S(R)\}+\ln\{L_{aer}\}-2[L_{aer}-L_{mol}]\int_0^R \beta_{mol}(R)dr=\ln\{E_0\}+\ln\{\eta_0\}+\ln\{Y(R)\}-2\int_0^R Y(R)dr$$

A.16

Then, the derivative of eq. A.16 with respect to Range (R) is shown in eq. A.17, and a simplified version is given by eq. A.18 where the constant derivative are equal to zero. The purpose of this is to convert this equation into a differential equation.

$$\frac{d}{dr}\ln\{S(R)\}+\frac{d}{dr}\ln\{L_{aer}\}-2[L_{aer}-L_{mol}]\frac{d}{dr}\int_0^R \beta_{mol}(R)dr=\frac{d}{dr}\ln\{E_0\}+\frac{d}{dr}\ln\{\eta_0\}+\frac{d}{dr}\ln\{Y(R)\}-2\frac{d}{dr}\int_0^R Y(R)dr$$

A.16

$$\frac{1}{S(R)}\frac{d}{dr}S(R)-2[L_{aer}-L_{mol}]\beta_{mol}(R)=\frac{1}{Y(R)}\frac{d}{dr}Y(R)-2Y(R)$$

A.17

Substituting, Y(R) by its respective terms in the eq. A.17, producing eq. A.18.

$$\frac{1}{S(R)}\frac{d}{dr}S(R)-2[L_{aer}-L_{mol}]\beta_{mol}(R)=\frac{1}{[\beta_{aer}(R)+\beta_{mol}(R)]}\frac{d}{dr}[\beta_{aer}(R)+\beta_{mol}(R)]-2L_{aer}[\beta_{aer}(R)+\beta_{mol}(R)]$$

A.18

Eq. A.18 is known as Bernoulli differential equation. This equation can be solved using the Bernoulli equation for boundary conditions, which is Y(R$_0$) [37,38].

106

$$Y(R_0) = L_{aer} [\beta_{aer}(R_0) + \beta_{mol}(R_0)] \qquad \text{A.19}$$

Therefore, the solution of the eq. A.18 for total backscatter is given by:

$$\beta_{aer}(R) + \beta_{mol}(R) = \cfrac{S(R)Exp\left[-2[L_{aer} - L_{mol}]\int_{R_0}^{R}\beta_{mol}(r)dr\right]}{\cfrac{S(R_0)}{\beta_{aer}(R_0) + \beta_{mol}(R_0)} - 2L_{aer}\int_{R_0}^{R}S(r)Exp\left[(L_{aer} - L_{mol})\int_{R_0}^{r}\beta_{mol}(z)dz\right]dr} \qquad \text{A.20}$$

Consequently, the aerosol extinction coefficient can be obtained from the aerosol lidar ratio.

$$L_{aer} = \frac{\alpha_{aer}(R)}{\beta_{aer}(R)} \qquad \text{A.21}$$

The aerosol lidar ratio in this work is assumed constant and its value depends on the aerosol type. Its value can be determinate from reference [4], or estimated from AERONET, or Sun-photometer.

"The total backscattering cross section at range R can be expressed as a function of the scattering properties at the calibration range and those of the intervening atmosphere between the ranges R_0 and R" [37,38].

The following equation is used to replace the part in the exponential.

$$A(I, I+1) = [L_{aer} - L_{mol}][\beta_{mol}(I) + \beta_{mol}(I+1)] \qquad \text{A.22}$$

Now, the total backscatter cross section at range $R(I+1)$ is:

$$\beta_{aer}(I+1) + \beta_{mol}(I+1) = \cfrac{S(I+1)Exp[-A(I, I+1)]}{\cfrac{S(I)}{\beta_{aer}(I) + \beta_{mol}(I)} - L_{aer}\{S(I) + S(I+1)Exp[-A(I, I+1)]\}\Delta R} \qquad \text{A.23}$$

Now, the total backscattering cross section at $R(I-1)$ is:

$$\beta_{aer}(I-1) + \beta_{mol}(I-1) = \cfrac{S(I-1)Exp[A(I-1, I)]}{\cfrac{S(I)}{\beta_{aer}(I) + \beta_{mol}(I)} + L_{aer}\{S(I) + S(I-1)Exp[A(I-1, I)]\}\Delta R} \qquad \text{A.24}$$

Finally, applying the Klett's conclusions for highly turbid atmosphere, we have [37, 38]:

$$\beta_{aer}(I-1) = \frac{S(I-1)}{\dfrac{S(I)}{\beta_{aer}(I)} + L_{aer}\left\{S(I) + S(I-1)\right\}\Delta R} \qquad \text{A.25}$$

APPENDIX B Kernel function for Mie Efficiencies and Spherical Particles

The Kernel function depends on the Mie efficiencies for spherical shapes. The efficiencies depend on the refractive index m, the wavelength λ, and the particles radii r. The refractive index is a complex number where the imaginary part means absorption. The Extinction efficiency is the sum of scattering and absorption efficiencies. Eq. B.1 and B.2 show the scattering and absorption efficiencies [10].

$$Q_{sca} = \frac{128\pi^4 r^4}{3\lambda^4} \left| \frac{m^2-1}{m^2+2} \right|^2 \qquad \text{B.1}$$

$$Q_{abs} = \frac{8\pi r}{\lambda} \text{Im}\left\{ \frac{m^2-1}{m^2+2} \right\} \left[1 - \frac{32\pi^3 r^3}{\lambda^3} \text{Im}\left\{ \frac{m^2-1}{m^2+2} \right\}^2 \right] \qquad \text{B.2}$$

The backscatter efficiency is given by eq. B.3.

$$Q_{back} = \frac{64\pi^4 r^4}{\lambda^4} \left| \frac{m^2-1}{m^2+2} \right|^2 \qquad \text{B.3}$$

Finally, the kernel function can be calculated in terms of surface area (eq. B.4) or volume concentration (eq. B.5 [10], where the subscript i represents either of the two data types (extinction or backscatter) at the specific wavelength.

$$K_S = \pi r^2 Q_i \qquad \text{B.4}$$

$$K_V = \frac{3Q_i}{4r} \qquad \text{B.5}$$

APPENDIX C   B-Spline Modeling for ASD Calculation

In this research, base functions are used to stabilize the inversion process. The B-splines functions used are of first degree equidistant triangles. This function permits easy reconstruction of the volume size distribution for monomial and binomial distributions [10, 40]. In this case each B-spline (triangle) has 113 data points. The six B-splines presented in Fig. 13 are fixes in a 6x113 array.
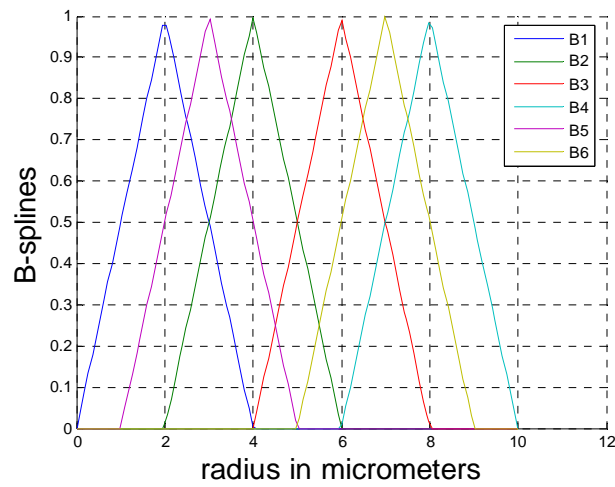
Figure C-1 First order B-splines results.

APPENDIX D   Regularization   Method   for   ASD

Calculation

The simplest solution of w presented in eq. 3.34 does not provide restorable results, because it is highly oscillatory. The oscillation provides errors in the solution of the microphysical properties even though the optical data can be reproduced with high accuracies. The regularization method suppresses the oscillations by applying certain mathematical and physical constraints [10, 38, 43].

The error e introduced in $g = Aw + e$ is needed to determine the microphysical properties. This is because it is not possible to reproduce the exact optical data [10, 38]. The method of maximum distance defined by Euclidian norm has been applied to the error which is presented by eq. D.1.

$$e^2 \geq \left\| Aw - g \right\|^2 + \gamma \Gamma(v) \qquad \text{D.1}$$

The constraint of smoothness is included in the nonnegative scalar $\Gamma(v)$, and it can be written as [10, 43]:

$$\Gamma(v) = w^T H w \qquad \text{D.2}$$

This measures the deviation of the inverted particle size distribution v(r) from the requested smoothness [10, 43]. The smoothness is the second derivative of the reconstructed particle size distribution. The mathematical formulation of the smoothing matrix H is obtained in eq. D.3 [10, 43].

$$H = \begin{bmatrix} 1 & -2 & 1 & 0 & 0 & 0 \\ -2 & 5 & -4 & 1 & 0 & 0 \\ 1 & -4 & 6 & -4 & 1 & 0 \\ 0 & 1 & -4 & 6 & -4 & 1 \\ 0 & 0 & -2 & 5 & -4 & 1 \\ 0 & 0 & 0 & 1 & -2 & 1 \end{bmatrix} \quad \text{D.3}$$

The solution of the minimization concept is obtained through substituting eq. D.3 in

eq. D.2. The solution of the weights factors is given by eq. 3.35. The scalar γ is the Lagrange

multiplier. It varies from a low value to a high value. With $\gamma=0$, no smoothing can take place,

and the solution of w is given by eq. 3.34. For high values of γ, the solution is over

smoothed, and the derivatives solutions cannot reproduce the input data. That means the

input data can be negligible. γ must be chosen such that the complete penalty eq. 3.35

becomes a minimum [38].

APPENDIX E   Aerosol size distribution algorithm (ASD)

The algorithm developed in this research for the calculation of ASD uses a flow chart as depicted in Fig. E.1. In this algorithm, the B-spline function matrix is of size 6x113, Kernel matrix k = 6x113, where there are 3β+3α optical data, and a radius vector of 113 different sizes. Matrix A which is determined by eq. 3.32, and W determined by eq. 3.32 are of sizes 6x6 and 1x6, respectively. And the final result, volume size distribution of eq. 3.30, is of size 1x113.
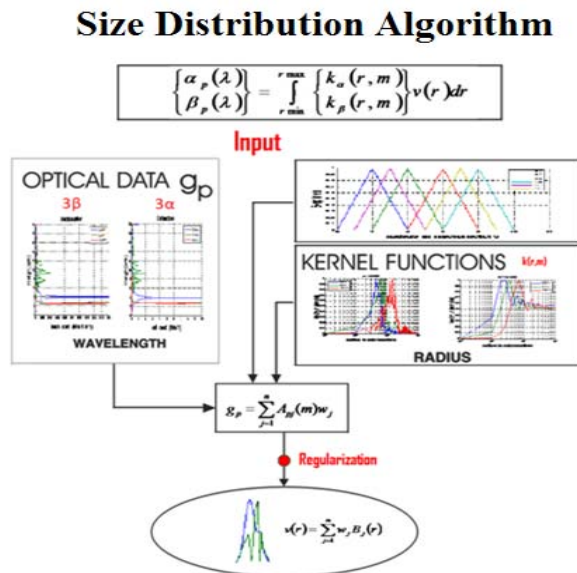
Figure E-1 ASD algorithm block diagram.

APPENDIX F   UPRM-Lidar Laboratory

In December 2008, a new laboratory was developed at the UPRM for atmospheric researches. A multi-wavelength Lidar system was installed at the UPRM ECE department. This lab was designated for atmospheric remote sensing studies where the user can be involved with the data acquisition process and data processing available in four workstations. It was installed at the first floor of Stephanie building in Room F-105-FI. The UPRM-Lidar laboratory ($18^0 12'4N$, $67^0 08'24W$, and elevation of 13m above the sea level) is located in the Western part of PR (Puerto Rico), see Fig. F-1. The lab consist in an advanced atmospheric research systems in a 16' x 16' room with an opening chimney that pass over the second floor until permit the sky access with a 20 inch optical telescope. The goal to develop this laboratory is to provide atmospheric profiles of aerosol-cirrus-dust optical properties with high temporal and spatial resolution scanning the sky over the UPRM campus, and join to the global Lidar network in the future.

Figure F-1 Geographical location of the UPRM Lidar laboratory.

F.1 UPRM-Lidar System

The UPRM-Lidar is a stationary system where the laser beam is transmitted into the atmosphere coaxially with the telescope, eliminating the overlap problem between the reflected spot and the telescope FOV (field of view). There are three guide mirrors installed at 45 degrees on the exterior part of the telescope which guide the laser beam up to the atmosphere and coaxial to the center of the telescope.

A very weak light beam is received by the telescope and is focused on a focal point of a lens (f=30mm) which transmits a parallel beam of 8mm diameter. The beam is split twice by two bi-directional selectors positioned at 45 degrees to the incident beam (See Fig. F-2). The results are three 8mm beams of wavelengths approximately to: $\lambda 1 < 400nm$, $400nm < \lambda 2 < 900nm$, and $900nm < \lambda 3$. These beams after passing through attenuators are submitted to three interference filters which allow only the pass of 355, 532, and 1064nm wavelengths. Three extremely sensitive sensors have been acquired to collect the signal at the three mentioned wavelength.
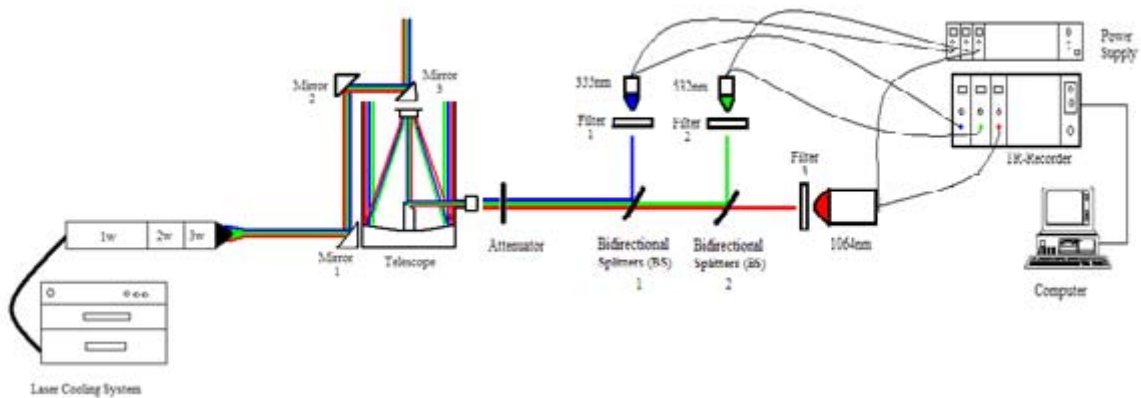
Figure F-2 UPRM Lidar Systems, where the beam expander is optional.

115

The transmitter system is composed of the laser unit, the guide mirrors and the beam expander (optional). Fig. F-3 shows the transmitter system installed in the UPRM-Lidar lab, the laser transmits the light beam and then it is guided to the atmosphere by the three guide mirrors. The laser transmits a light beam at the three wavelengths of 355, 532, and 1064nm, which are represented by 3w, 2w, and 1w. The guide mirrors (*dichroic mirrors)* are special mirrors that support the laser power for each generated wavelength.
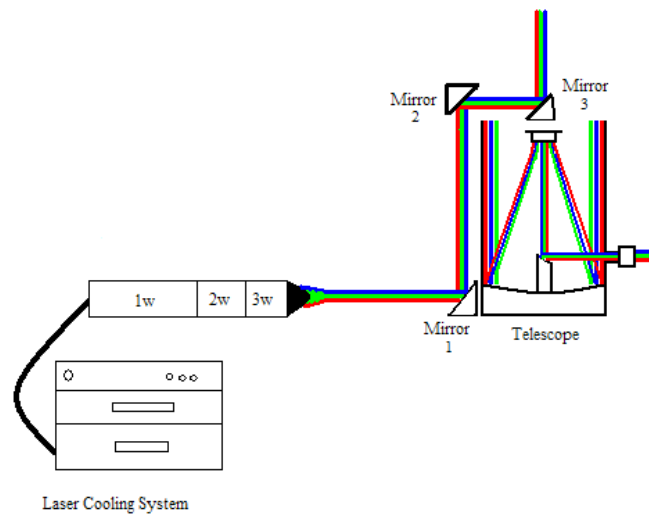
Figure F-3 UPRM-Lidar complete transmitter system.

The laser system is a Nd:YAG type which is a coherent collimated monochromatic light source. An excited medium may be brought back to its fundamental state by emitting photons in a spontaneous and non coherent manner as in natural light sources. The laser transmits the 2nd and 3rd harmonics of a 1064nm Nd:YAG laser, 532nm and 355nm respectively, see Table F-1 for laser specifications.

UPRM-Laser specifications	
Laser	Brilliant B Nd:YAG
Pulse frequency	20Hz
Pulse duration	4.8ns
Fundamental power at 1064nm	700mJ
Power output at 532nm	300mJ
Power output at 355nm	120mJ
Beam diameter	8mm
Divergence angle	0.7mrad

Table F-1 UPRM-Lidar transmitter characteristics.

The output energy of the laser is not eye-safe and several safety precautions are taken during operation. The users need to have special goggles, and a PVC tube is used to cover the laser light beam. Radar with a vertical cone around the laser beam is needed to be installed to detect aircraft and send a signal to shut off or block the laser beam if detection occurs.

The laser consists of two major subassemblies: the optical head, and the power supply and cooling system (Fig. F-4). They are connected together by cables and hoses, running through an umbilical. The optical head contains all the necessary components for generating the infrared laser beam, and the optional 2nd (2ω) and 3rd (3ω) harmonics, including a wavelength separation package. The power supply in addition to energizing the optical head provides all logical functions necessary to operate the laser and the cooling capability to dissipate the heat generated in the optical head by the operation of the flash lamps [33].

Additional safety and flexibility in operating the laser is provided by a remote control box and a RS232 computer interface.

Figure F-4 UPRM Lidar laser unit (laser unit-left and power supply and cooling unit-right).

The power supply unit consists of four subassemblies packaged in the electronics cabinet (Power supply and Cooling Cabinet - PCC) shown in Fig. F-4 for Brilliant B, are packaged in a 19" rack (MPS). Inside of this cabinet are the following [59]:

- Power board: to charge the capacitor bank storing energy for the flash lamps discharge.

- Simmer board: to maintain a low "simmer" current between the pulses in order to decrease the E.M.I. noise and improve the lifetime of the lamps.

- Harmonic generators power supply: to perform crystal cells temperature regulation. This option comes with the 2ω module.

- Control board: to control the timing of charge and fire orders, to operate the laser in Manual, Automatic or External mode, to monitor security interlocks (switch the laser off when a malfunction is detected).

The dichroic mirrors used to guide the laser beam into the atmosphere are of one inch diameter, and the coating wavelengths are at 355, 532, and 1064nm with an angle of 45 degrees. The receiver system collects the return signal at the three transmitted wavelengths measured after spectral separation and isolation using high sensitive sensors. Fig. F-5, presents the complete UPRM-Lidar receiver system in which the scattered light is collected by the telescope and then is separated at the respective wavelengths in which are connected the respective sensors. The sensors are connected to the power supply and to the transient recorder, where the transient recorder convert the analog signal to digital, and then each signal is processed and collected by the computer.
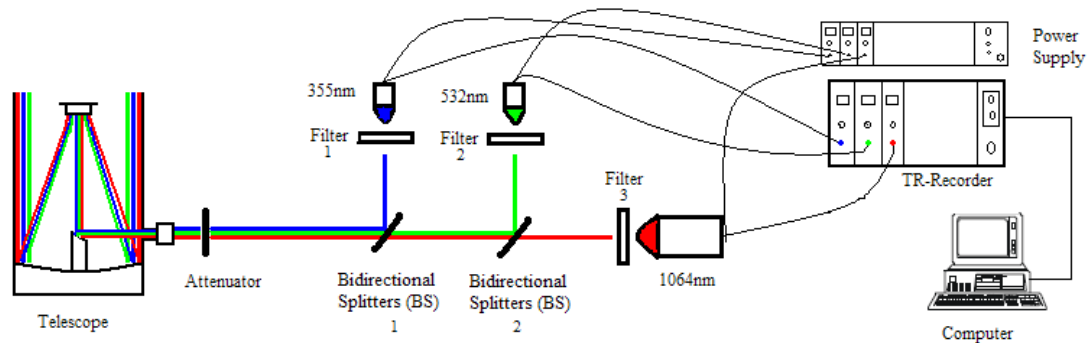

Figure F-5 UPRM Lidar completes receiver system.

A Dall-Kirkam Cassegrain telescope is used for the backscatter light collection. This telescope has a clear aperture of 19.5", 8" of back focus, and an amplification of 2.67X, see Table F-2 for the telescope specifications. Fig. F-6: a) shows one side of the telescope, b) shows a top view, and c) shows the light collection description.

UPRM-Telescope specifications	
Optical Ssystem	Dall-Kirkam Cassegrain
Clear aperture	19.5" with F/4 (80" focal length)
Primary mirror	Radius of 59" concave ellipsoidal with F/1.5
Secondary mirror	Radius of 32.3" convex spherical
Mirror separation	18.9"
Amplification	2.67X
Output beam diameter	8mm

Table F-2 UPRM-Lidar telescope specifications.

a)   b)   c)
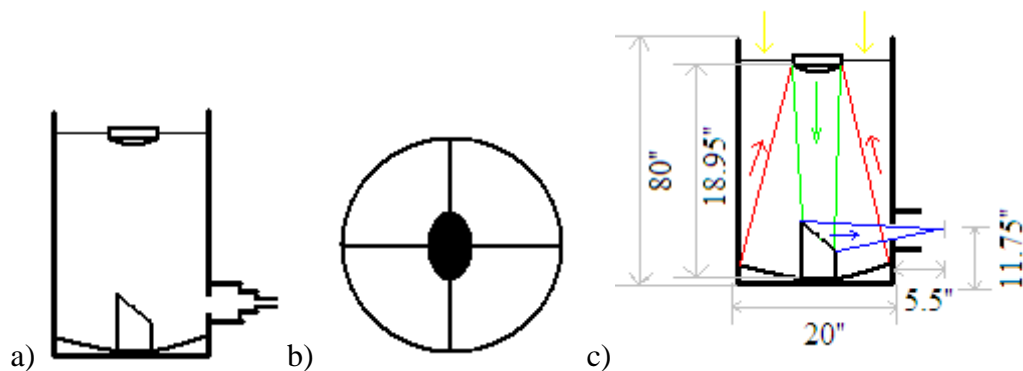
Figure F-6 UPRM Lidar Telescope descriptions.

Basically, this telescope collects the backscattered light from the atmosphere (yellow lines in Fig. F-6 c). This light is reflected from the primary to the secondary mirror (red cone in Fig. F-6 c), then the light scattered from the secondary mirror (green cone) is guide to the outside of the telescope by a third mirror (blue cone). These mirrors are adjusted to obtain a specific focal point at a distance of 5.5" from the outside of the telescope at 11.75" of height.

Outside of the telescope, at the focal point, is present an attenuator (see Fig. F-4). The attenuator is used to attenuate the light intensity with the purpose to protect the sensors and reduce the background noise occasioned by external source of light such as the Sun, Moon, etc... The backscattered light collected by the telescope have different wavelength, for this reason the BS (Bidirectional Splitters) mirrors are used to separate the light at the desired wavelengths intervals, Table F-3 shows the BS specifications. Based on the manufacturer test, the BS generates the following experimental wavelengths intervals: $\lambda_1 < 400$ (blue), $400 < \lambda_2 < 900$ (green) and $900 < \lambda_3$ (red) located in the front part of the sensors presented in Fig. F-5.

UPRM-Beam Splitter specifications	
BS (Beam Splitter)	Dichroric BS from CVI
Diameter & width	2" & 0.25"
BS 1	355R/488T
Polarization transmission	Unpolarized average transmission >85% at $\lambda > 488nm$
Polarization reflectance	Unpolarized average reflectance >99.5% at 355nm
BS 2	532R/830T
Polarization transmission	Unpolarized average transmission >85% at $\lambda > 830nm$
Polarization reflectance	Unpolarized average reflectance >99.5% at 532nm

Table F-3 UPRM-Lidar BS specifications.

In the λ_1 range is desired to collect the 355nm signal, in λ_2 range 532nm, and in λ_3 range 1064nm. To make safe the pass only of the desired wavelength, an interference filter is

used. The filter specifications are presented in Table F-4. With the interference filters, the experimental wavelength intervals are closest to the desired wavelength. Now, 354.7nm$<$ $\lambda1<355.3$nm, 531.7nm$<$ $\lambda2<532.3$nm, and 1061nm$<$ $\lambda3<1067$nm are the new intervals where $\lambda1=355$nm, $\lambda2 =532$nm, and $\lambda3 =1064$nm. To collect the 355 and 532nm signal PMTs (Photo Multiplier Tube) sensors are used, while for 1064nm signal an APD (Avalanche Photo Diode) is used.

UPRM-Interference filter specifications	
Filter types	Narrowband interference filter
Diameter & width	2" & 0.25"
Filter 1(355nm)	3 Angstrom (±0.3nm)
Filter 2 (532nm)	3 Angstrom (±0.3nm)
Filter 3 (1064nm)	± 3nm

Table F-4 UPRM-Lidar interference filters specifications.

The PMTs (Fig. F-7) are used to obtain high dynamic range detection for analog and photon counting signals. This sensor combines a stabilized diode chain for strong light pulses with fast rise times and narrow pulse widths for high single photon count rates. This combination allows high dynamic range measurements by using both analog and photon counting measurements together, thus extending the linear dynamic range to 5 orders of magnitude. Additional advantages are reduced space charge effects and higher light levels that can be measured without suffering from nonlinearities. Table F-5 shows the PMTs manufacturer specifications.

Figure F-7 PMT sensors.

UPRM-PMT specifications	
Detectors	Hamamatsu
PMT: 355nm	HA9626
Wavelength range & peak	185-650nm & 420nm (UV to Visible)
PMT: 532nm	L00280
Wavelength range & peak	300-900nm & 630nm (UV to Near IR)

Table F-5 UPRM-Lidar PMT detectors specifications

The APD sensor consists of low noise-high speed detection for a wavelength interval of 400-1100nm. It also has a TE-cooled detector, a high-speed low-noise preamplifier and a HV supply. Signals can be acquired using analog detection as well as single photon counting mode. Integrate focusing optics and alignment mechanics allow easy integration into the optical setup (Fig. F-8). The increased sensitivity in the near infrared is a major advantage compared to PMTs. Table 4-6 presents the APD manufacturer specifications.
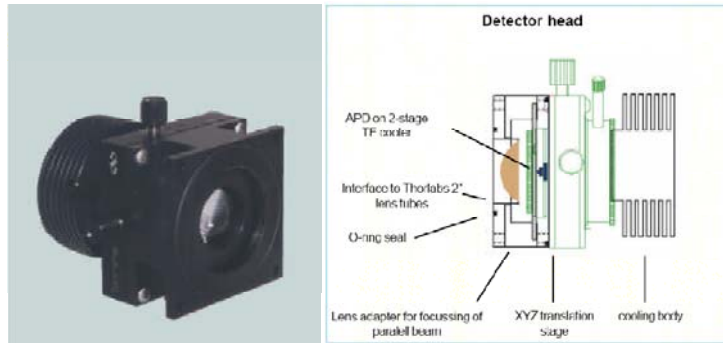
Figure F-8 APD sensors.

UPRM-APD specifications	
Detector	Perkin & Elmer
APD: 1064nm	C30955E-TC
Wavelength range	400 to 1100nm
Efficiency at 1064nm	38%

Table F-6 UPRM-Lidar APD specifications.

The power supply rack is used to excite the sensors (PMT's and APD). Also, the power supply rack has a triggering source which simulates the laser light reflection for pulse synchronization. Fig. F-9 displays the power supply rack, the power supply card in the left is the APD voltage source, and the other two are for 532 and 355nm. The rack has four extra spaces in spare for future sensors, and the card in the right side is the triggering generator. The trigger is fundamental in the data acquisition because it is used to collect the received signal of each light pulses transmitted by the laser. The recommended voltage for each sensor is presented in Table F-7.

Figure F-9 Licel power supply unit.

UPRM-Detectors power	
PMT: 355nm	750-850V
PMT: 532nm	750-850V
APD: 1064nm	261-311V

Table F-7 UPRM-Lidar recommended power for each detector.

The transient recorder is from Licel Company of Germany (Fig. F-10). Licel transient recorder is a data acquisition system used for fast repetitive photomultiplier signals in the voltage range 0 to 500mV. The signal is recorded simultaneously by a 12Bit, 20MHz analog to digital converter and a discriminator which detects voltage pulses above selected threshold in range of 0 to 100mV. This combination of analog and photon counting detection is specially suited to record high dynamic range signals in Lidar applications.

The model used in the UPRM Lidar laboratory is TR 20-160 with three separate channels, each channel contains 2 preamplifiers optimized for high linearity for analog detection and maximum speed and gain for photon counting, a 12 Bit A/D converter with fast

memory for 16k of single shot data, a discriminator with variable threshold, counter and multichannel scale as well as a hardware adder to perform summation up to 4094 shots on board. Data transfer and selection of input ranges and discriminator threshold is realized by a parallel data bus, connected to an Ethernet controller. The transient recorder is controlled by LabView application software. This program converts the electric signal to a text file in which the data is ready to process in Matlab or other programming language.

Figure F-10 Licel transient recorders.

F.2   Data Acquisition

The data acquisition process is making with LabVIEW, which is a National Instrument product. This product is a graphical programming that combines a programming language with a graphical development. It offers an intuitive environment, tightly integrated with measurement hardware, to produce solutions for data acquisition analysis and representation.   All LabVIEW applications execute at compiled speed for optimal performance.

This program is due to the fact that all software development on the transient recorder control, made by Licel, and was made under LabVIEW configuration. It is nowadays, the

best solution in this field of instrument control. Apart the libraries furnished by Licel to drive the transient recorder, specific ones have been made to permit the data acquisition and treatment.

Here after will be shown and discussed only the main part of the UPRM Lidar data acquisition software.
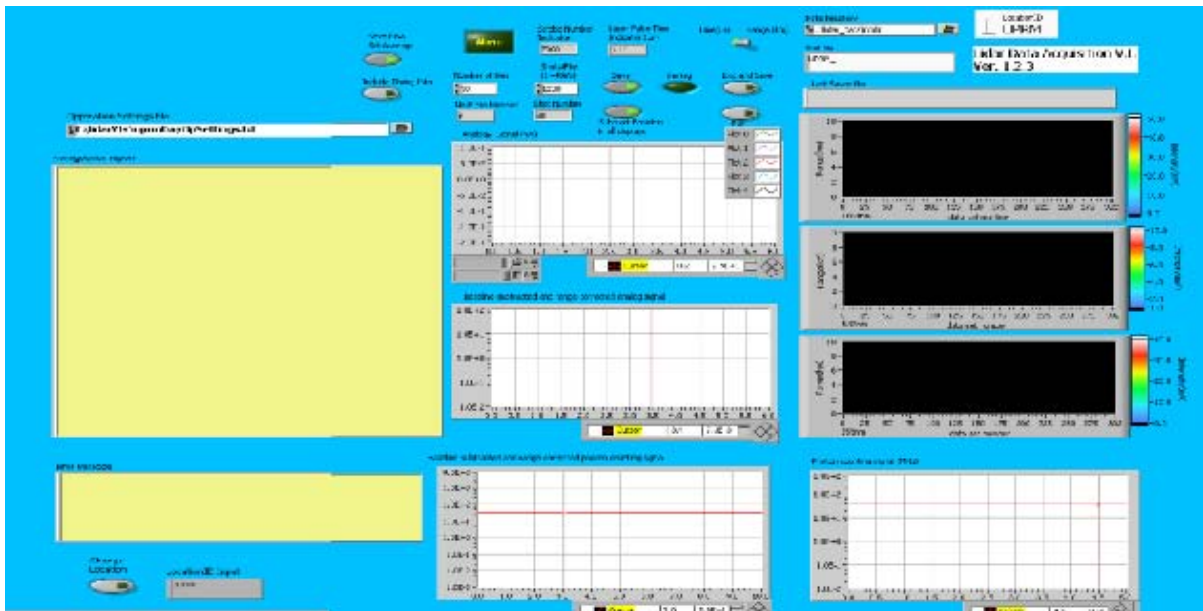

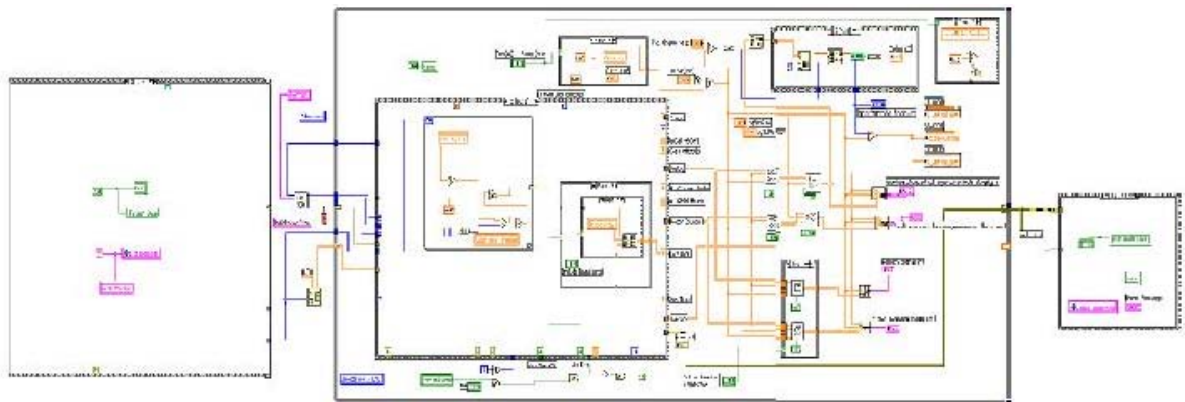**Figure F-11** UPRM Lidar front panel VI for data acquisition.

Figure F-12 UPRM Lidar back panel VI for data acquisition.

The last two figures show the data acquisition front and back panel program used to acquire the Lidar signals. The main characteristics of the Lidar signals can be visualized, such as the raw signal, range corrected signal, and the logarithmic range corrected signals at the three fundamental wavelengths (355, 532, and 1064nm). This program enables to treat a variety of files, like a single 1200 laser beam shots per file and save one file of this each minute. A series of dialog boxes permit to set parameters such as the binning, the minimum and maximum altitudes, the atmospheric conditions, the desired analyzed channels in photon counting or analog, Lidar localization (Latitude, Longitude, and altitude), and others.

The visualization of the received data of the three channels in raw and range corrected forms are available to give the first look to permit to see where is the total overlap height, the PBL, clouds, aerosol layer, and other particles suspended in the atmosphere.

The data treatment procedure is the following: The first step is made with a careful analysis of the 1200 laser beam shots single files with the data treatment programming loading the desired file in Matlab. Each 1200 laser beam shot files are composed of four text columns which are in the order of range, 355, 532, and 1064nm received power profiles. Also, all this files are saved in an averaged time of one minute in an archive with the correct date. Fig. F-13 shows an example of a single 1200 laser beam text file saved on the day of March 17, 2009, meanwhile table 4-8 shows the raw data resolution. During this day the UPRM-Lidar system was collected data around 3hrs, saving a total of 180 text files of 1200 laser beam.
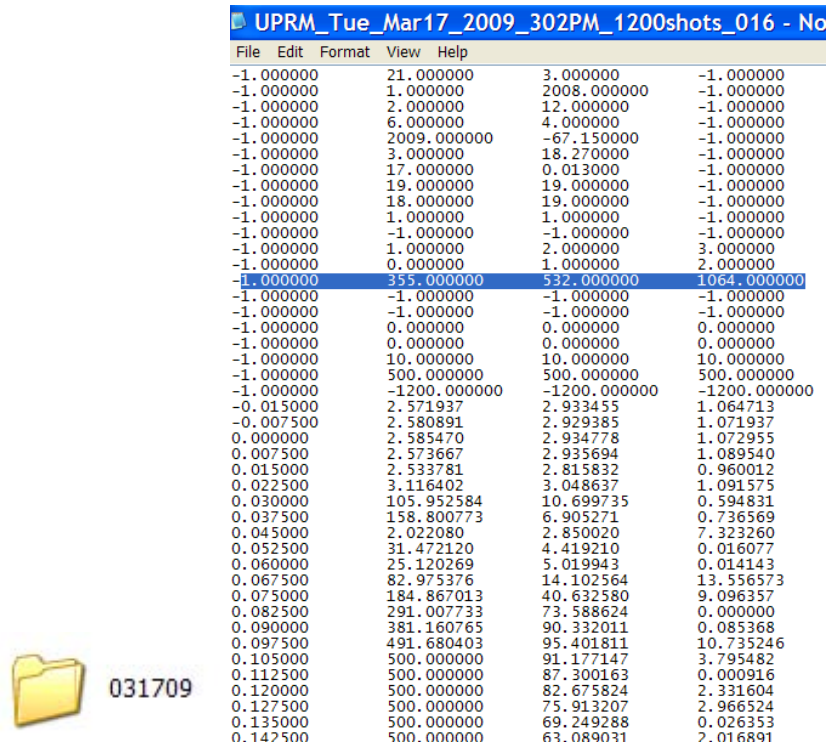
Figure F-13 1200 laser beam shots raw data file example.

UPRM-Lidar resolution	
Vertical	7.5m
Horizontal	1min

Table F-8 UPMR-Lidar data resolution.

APPENDIX G City College of New York (CCNY) Lidar System

The UPRM-Lidar system is based on the same format as the CCNY-Lidar system. The differences between these two systems are in the instrumentation system where the CCNY have two extra receivers for Raman Scattering. This system is considered as Mie-Raman Lidar system. The transmitter is a Nd:YAG laser and the generated beam is on axis to the telescope (same as UPRM), directed by three dichroric mirrors. The following tables present the laser, telescope and detector systems.

CCNY-Laser	
Laser	Quanta-Ray Pro Series Pulsed Nd:YAG
Pulse frequency	30Hz
Pulse duration	6ns
Fundamental power at 1064nm	950Mj
Power output at 532nm	475mJ
Power output at 355nm	300mJ
Beam diameter	8mm
Divergence angle	0.5mrad

Table G-1 CCNY-Lidar laser systems {source: [60]}.

CCNY-Telescope	
Optical Ssystem	Newtonian
Clear aperture	20" with F/3.5
Focal length	70"

Table G-2 CCNY-Lidar telescope systems {source: [60]}.

CCNY-Detectors	
Detectors	Hamamatsu
PMTs	355(UV), 387 (raman), 407(raman), and 532nm (Visible)
APD	1064nm (Near IR)

Table G-3 CCNY-Lidar detectors {source: [60]}.

The digitalizing system is a Lidar Transient Recorder TR 40-160 with 12 bit, 40MHz A/D converter for signals between 10MHz and 200MHz, and 64 level fast discriminator for signals in the high frequency domain above 200MHz. The range resolution is around 500m to 15km [60]. The data acquisition system is configured by the TR 40-160 Transient Recorder modules for all channels in a five channel rack comprising power supplies and interface ports to a PC computer equipped with a National Instrument digital I/O card, DIO-32F [60]. Each channel can be configured and controlled separately by a computer.

A radar interface in a vertical radar emitter and antenna continually search for the presence of aircraft a failsafe interlock for the beam while the laser is in operation [60]. On detection of aircraft, the laser beam is automatically disabled a lidar data acquisition halted.

APPENDIX H Calipso Satellite as a Validation Sensor

Calipso (Cloud-Aerosol Lidar and Infrared Pathfinder Satellite Observations) is joint NASA76-CNES satellite mission designed to provided measurements aimed at improving our understanding of the rile of aerosol and clouds in the climate system [61]. The Cloud-Aerosol LIdar with Orthogonal Polarization (CALIOP) is the primary instrument inside of this satellite system [61]. Calipso is designed to acquire vertical profiles of elastic backscatter at two wavelengths of 1064 and 532nm form a near nadir-viewing geometry during both day and night phases of the orbit. In addition to the total backscatter at the two wavelengths, Calipso provides profiles of linear depolarization at 532nm. Accurate aerosol and cloud heights and the retrieval of extinction coefficient profiles are being derived from the total backscatter measurements. The depolarization measurements enable the discrimination between ice clouds and water clouds and the identification of non-spherical aerosol particles [61]. Additional information, such as estimates of aerosol particles size are obtained from the ratios of the signals obtained at the two wavelengths.
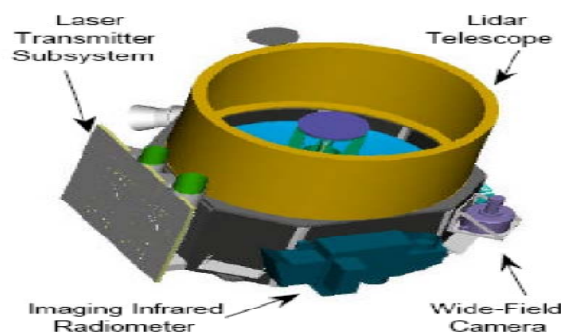

Figure H-1 Schematic of Calipso satellite instrumentation {source: [61]}.

In addition, this satellite has an Imaging Infrared Radiometer (IIR), provided by CNES, with three channels in the infrared region optimized for retrievals of cirrus particle size, and a single channel Wide Field Camera (WFC) [62]. The WFC is a moderate spatial resolution camera operating in the visible regime to provide meteorological context for Calipso and IIR measurements, and as a means of accurately co-registering CALIPSO observations of those form other instruments in the A-Train such as MODIS [61]. WFC data is also combined with data form IIR and Calipso to retrieve cloud properties. The A-Train (Fig. H-2) is a constellation of USA and international Earth science satellites fly together with EOS Aqua to enable coordinated science observations. These satellites have an afternoon crossing time close to the mean local time of the 'lead' satellite, Aqua (1:30Pm); thus, the name , 'A (short for afternoon) Train'. One April 28, 2006, the Calipso satellite was launched to a low earth sun-synchronous at a 705 km altitude, and an inclination of 98.2 degrees [62]. Calipso reports the following products of interest at 532 and 1064nm: AOD, α_a, and β_a. Fig. H-3 shows an example of the received data of Calipso-Lidar in June 2006, where are presented clouds, and aerosol layers.

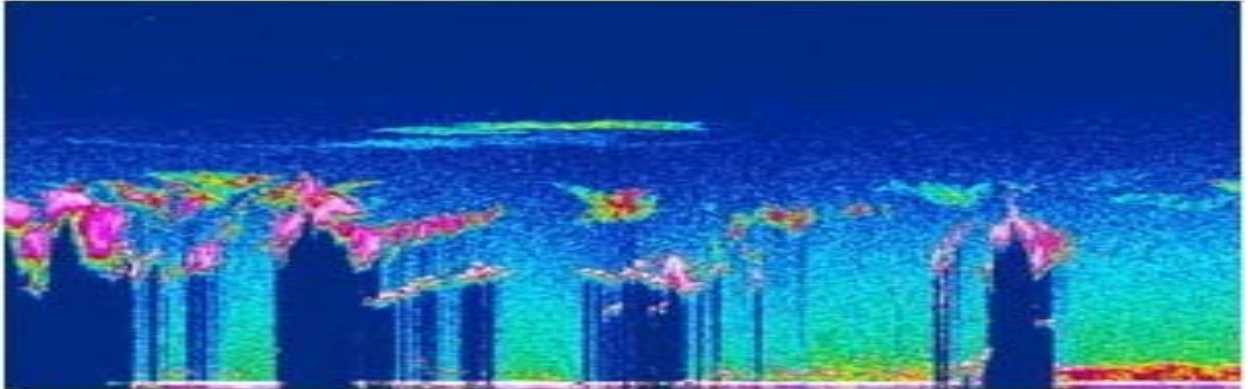**Figure H-2** A-Train satellite systems{source: [61]}..

Figure H-3 Calipso-Lidar logarithmic range adjusted intensity image from sea level up to 30km in June 2006{source: [62]}.

APPENDIX I AERONET & Portable Sun-Photometer (SP) as a Validation and Calibration Sensor

AERONET (AERosol Robotic NETwork) is based on Cimel sunphotometer instrument which is a multi-channel automatic Sun and Sky scanning radiometer that measures the direct solar irradiance and sky radiance at the Earth's surface [63]. Measurements are taken at the visible and near-Infra-Red wavelengths to determine the atmospheric transmission and scattering properties. It only takes measurements during daylight.

The concept of sunphotometer is to measure the direct sun light and calculates the attenuation [64]. Applying the Beer-Lambert-Bouguer's (BLB) law, this relates the intensity of the light at the top of the atmosphere. The Langley plot is constructed based on the BLB law, in which the measured intensity is plotted as a function of solar zenith angle. By extrapolating the curve to zero atmospheric thickness the top of atmosphere intensity is retrieved and can be used to calculate the optical depth or optical thickness of the atmosphere [63, 64]. The sun light attenuation can be divided into the molecular, aerosol, and ozone scattering and absorption. The molecular scattering and ozone scattering are derived from ASA76. The aerosol contribution is expressed as the AOD, which is dependent on the wavelength, and was established by Angstrom [42, 43]. If the AOD is measured at two

different wavelengths the spectral dependence is approximated as a power law relationship between the corresponding ratios of AOD and wavelengths (see chapter 4).

AERONET report their products at three different levels that depends on the methodology used to obtain it. The level 1, 1.5, and 2 reports the following parameters: AOD, WV (water vapor) in cm, Å exponent, AOD Fine/Coarse, and ASD depending on the station. Fig. I-1 show AOD examples reported at La Parguera AERONET station based on level 1 data.
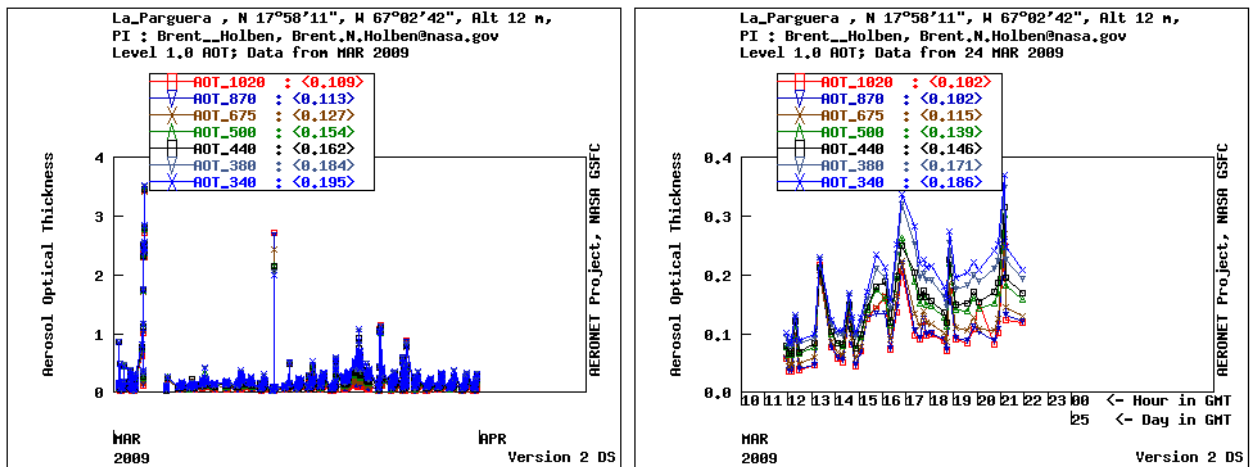

Figure I-1 AOD Level 1 data from March 2009 and March24[th], 2009 reported in La Parguera, PR {source: [65]}.

APPENDIX J   Air Quality

The air quality is calculated by AQI (air quality index) an index for reporting daily air quality. It reports how clean is the air, and if you health is in risk.   The health effects are associated with the inhalation of polluted air by few hours or days. EPA calculated the AQI for the following air pollutants: ground-level ozone, particle pollution or particle matter (PM2.5), carbon monoxide, sulfur dioxide, and nitrogen dioxide [54].   For each of these pollutants, EPA has established national air quality standards to protect public health. Ozone and airborne particles in the PBL are the two principal pollutants that cause greatest threat to the human health in USA [54].

Air Quality Index Levels of Health Concern	Numerical Value	Meaning
Good	0-50	Air quality is considered satisfactory, and air pollution poses little or no risk.
Moderate	51-100	Air quality is acceptable; however, for some pollutants there may be a moderate health concern for a very small number of people who are unusually sensitive to air pollution.
Unhealthy for Sensitive Groups	101-150	Members of sensitive groups may experience health effects. The general public is not likely to be affected.
Unhealthy	151-200	Everyone may begin to experience health effects; members of sensitive groups may experience more serious health effects.
Very Unhealthy	201-300	Health alert: everyone may experience more serious health effects.
Hazardous	> 300	Health warnings of emergency conditions. The entire population is more likely to be affected.

Figure J-1 Air Quality levels in relation with human health {source: [54]}.

Figure J-2 Air Quality Index calculator {source: [53]}. This calculator is available in [53].

Reference

[1] HTTP://WWW.YALE.EDU/YNHTI/CURRICULUM/UNITS/1981/2/81.02.06.X.HTML

[2] Earthwatch, U.N.S.-W., Air pollution and health. 2004, UNEP/GRID- Geneva.

[3] Couach, O., I. Balin, R. Jimenez, P. Ristori, S. Perego, F. Kirchner, V. Simeonov, B.Calpini, and H. van den Bergh, An investigation of ozone and planetary boundary layer dynamics over the complex topography of Grenoble combining measurements and modeling. Atmospheric Chemistry and Physics, 2003. 3: p. 549-562.

[4] Lidar and Atmospheric Aerosol Particles, Albert Ansmann and Detlef Muller, 2005.

[5] Seinfeld, J.H., Pandis, S.N., 1998. Atmospheric Chemistry and Physics: From Air Pollution to Climate Change. Wiley, New

York, 1113-1192.

[6] CALIOP Algorithm Theoretical Basis Document Part 2: Feature Detection and Layer Properties Algorithms, 2006.

[7] Youngha Wu, Ben Herman, CUNY Lidar staff function for algorithm development, September 11, 2006

[8] NOAA, NASA76, and United States Air Force, "U.S. *Standard Atmosphere*", National Aeronautics and Space Administration, 1976.

[9] P. S. ARGALL and R. J. SICA, Lidar, The University of Western Ontario London, Ontario, Canada: p. 869-889 .

[10] Hamed Parsiani and Javier Méndez, Aerosol Size Distribution using Lidar Data and Typical Lidar Assembly, WSEAS Systems journal, 2008.

[11] E. H. Synge, Philos. Mag. **52**, 1,014–1,020 (1930).

[12] Stull, R. B., An Introduction to Boundary Layer Meteorology, Kluwer Academic Publishers, Dordrecht, 1988.

[13] Couach, O., I. Balin, R. Jiménez, P. Ristori, F. Kirchner, S. Perego, V. Simeonov, B. Calpini, and H. Van den Bergh, *An investigation of ozone and planetary boundary layer dynamics over the complex topography of Grenoble combining measurements and modeling.* Atmospheric Chemistry and Physics, 2003(3): p. 549-562.

[14] Hinds, W. C., Aerosol Technology: Properties, Behaviour, and Measurement of AirborneParticles, John Wiley and Sons, New York, 1999.

[15] Measures, R.M., Laser Remote Sensing, Fundamentals and Applications, Krieger Publications, Malabar, F.L., 1992

[16] IPCC, *Climate change 1994*. 1995, Cambridge: Press Syndicate of the University of Cambridge.

[17] Ramanathan, V., P.J. Crutzen, J.T. Kiehl, and D. Rosenfeld, *Aerosols, Climate, and the Hydrological Cycle.* Science, 2001. 295: p. 2119-2124.

[18] Twomey, S., *The influence of pollution on the short-wave albedo of clouds.* Journal of the Atmospheric Sciences, 1977. 34: p. 1149-1152.

[19] Ramanathan, V., Crutzen, P.J., Kiehl, J.T., Rosenfeld, D., *Aerosols, Climate, and the Hydrological Cycle.* Science, 2001. 294: p. 2119-2124.

[20] Schumann, U., *Contrail cirrus*. Cirrus, ed. D.K.L.e. al. 2000: Oxford Univ. Press.

[21]Day, S.e., *Dictionnaire Encyclopédique de l'Ecologie et des Sciences de l'Environnement*, ed. F. Ramade. 1993: Ediscience international. 421.

[22] Houghton, J.T., Y. Ding, D.J. Griggs, M. Noguer, P.J. van der Linden, and D. Xiaosu, *Climate Change 2001: The Scientific Basis: Contribution of Working Group I to the Third Assessment Report of the Intergovernmental Panel on Climate Change (IPCC),* 2001, Cambridge University Press, UK. p. 944.

[23] Balin, I., G. Larchvêque, R. Nessler, P. Quaglia, V. Simeonov, H. van den Bergh, and B. Calpini. *Monitoring of water vapor, aerosols and clouds/contrails in the free troposphere by lidar from Jungfraujoch station (3580 m ASL).* in *21st International Laser Radar Conference*. 2002. Quebec Canada.

[24]Larchevêque, G., Balin I., Quaglia P., Nessler R., Simeonov V., H. van den Bergh and Calpini B. *Optical properties of aerosols-clouds-contrails and water vapor mixing ratio by lidar from Jungfraujoch Research Station (3580 m ASL).* in *EGS (European Geophysical Assembly).* 2002. Nice-France.

[25] Reichardt, J., *Optical and geometrical properties of northern midlatitude cirrus clouds observed with a UV Raman lidar.* Physics and Chemistry of the Earth Part BHydrology Oceans and Atmosphere, 1999. 24(3): p. 255-260.

[26] Kley, D., J.M. Russell, and C. Phillips, *SPARC Assesement of upper tropospheric and stratospheric water vapor.* 2000, WMO/ICSU/IOC: World Climate Research Progamm. p. 11-91.

[27] Melfi, S.H., J.D. Lawrence, and M.P. McCormick, *Observation of Raman Scattering by Water Vapor in the Atmosphere.* Applied Physics Letters, 1969. **15**(9): p. 295-297.

[28] Cooney, J., *Remote measurement of atmospheric water vapor profiles using Raman component of laser backscatter.* Journal of Applied Meteorology, 1970(9): p. 182-184.

[29] Shine, K.P. and A. Sinha, *Sensitivity of the Earths Climate to Height-Dependent Changes in the Water-Vapor Mixing-Ratio.* Nature, 1991. 354(6352): p. 382-384.

[30] Clough, S.A., M.J. Iacono, and J.L. Moncet, *Line by line calculations of atmospheric fluxes and cooling rates: applications to water vapor.* Journal of Geophysical Research-Atmospheres, 1992(97): p. 15761-15785.

[31] Sinha, A. and J.E. Harries, *Water vapor and greenhouse traping: the role of far infrared absorbtion.* Geophysical Research Letters, 1995(22): p. 2147-2150.

[32] Schneider, E.K., B.P. Kirtman, and R.S. Lindzen, *Tropospheric water vapor and climate sensitivity.* Journal of the Atmospheric Sciences, 1999(56): p. 1649-1658.

[33] Browell, E., T.D. Wilkerson, and T.J. McIlrath, *Water vapor differential absorption lidar development and evaluation.* Applied Optics, 1979.

[34] http://hyperphysics.phy-astr.gsu.edu/Hbase/atmos/blusky.html

[35] Maria Grazia Frontoso, " Lidar remote sensing for the characterization of the atmospheric aerosol on local and large spatial scale", PHD dissertation in Apply Physics.

[36] Sigris M., "Air Monitorinc by Spectroscopy Techniques", Chemical Analysis, Vol. 127, 1994.

[37] Stable analytical inversion solution for processing lidar returns; James D. Klett, 1981.

[38] Analysis of atmospheric lidar observations; Frederick G. Fernald, 1984.

[39] Hinds, W. C., Aerosol Technology: Properties, Behaviour, and Measurement of AirborneParticles, John Wiley and Sons, New York, 1999.

[40] Albert Ansmann, Maren Riebesell, and Claus Weitkamp, "Measurement of atmospheric aerosol extinction profiles with a Raman Lidar", 1990 Optical Society of America.

[41] Cooney, J., Remote measurement of atmospheric water vapor profiles using Raman component of laser backscatter. Journal of Applied Meteorology, 1970(9): p. 182-184

[42] Javier Méndez, Hamed Parsiani, Emmanuel Sánches, "Remote Sensing of Atmospheric Particles Using Lidar, Calipso Stellite, & AERONET: Algorithm Development", WSEAS-Transactions on Systems International Conference, November 2008.

[43] Javier Méndez-Rodríguez and Hamed Parsiani, "UPRM Lidar Laboratory for Atmospheric Aerosol Studies: Algorithm development", WSEAS-Transactions on Systems Journal 2009.

[44] Daniela Viviana Vladutescu, Yonghua Wu, Leona Charles, Barry Gross, Fred Moshary, Samir Ahmed, *Analyses of Raman lidar calibration techniques based on water vapor mixing ratio measurements*, Optics and Remote Sensing Laboratory, Electrical Engineering Department, City College of New York, 140th Street & Convent Ave, New York.

[45]I Balin, Measurement and analysis of aerosols, cirrus contrails, water vapor and temperature in the upper troposphere with the Jungfraujoch lidar system, École Politechnique Federale de Lausanne, These No 2975, 2004.

[46] E.J.O'Connor, A.J. Illingworth, and R.J Hogan, A technique for Autocalibration of Cloud Lidar, American Meteorological Society, May 2004.

[47] J.A. Reagan, Fellow, IEEE, X. Wang, and M. T. Osborn, Spaceborne Lidar Calibration From Cirrus and Molecular Backscatter Returns IEEE Transactions on Geoscience and Remote sensing, vol. 40, No.10, Oct 2002.

143

[48] D. N. Whiteman@ all, Scanning Raman Lidar Error Characteristics and Calibration For IHOP, NASA/HQ.

[49] C. Weitkamp, LIDAR range-resolved optical remote sensing of the atmosphere , Springer 2005.

[50] D. V. Vladutescu, Yonghua Wu, Leona Charles, Barry Gross, Fred Moshary, Samir Ahmed, Water vapor mixingtyrt ratio used in lidar calibration technique, WSEAS, Tenerife, Spain, December, 2006.

 [51] Hamed Parsiani, Andres Bonilla, "*Aerosol Size Distribution Estimation using Sun photometer and Artificial Neural Network,*" 12th WSEAS International Conference on SYSTEMS, Heraklion, Greece, July 22-24, 2008.

[52] Chuen-Meei Gan, Leona Charles, Barry Gross, Fred Moshary, Sam Ahmed, *ANALYSIS OF THE INTERACTION OF AEROSOL TRANSPORT LAYERS ON LOCAL AIR QUALITY*, CUNY Graduate Center, Electrical Engineering, 365 Fifth Avenue, New York, NY 10016-4309 and Northrop Grumman Corporation Azusa CA 91702.

[53] http://www.airnow.gov/index.cfm?action=aqi.conc_aqi_calc

[54] http://www.airnow.gov/index.cfm?action=static.aqi

[55] Bockmann, C., *Hybrid regularization method for the ill-posed inversion of multiwavelength lidar data in the retrieval of aerosol size distributions.* Applied Optics, 2001. 40(9): p. 1329-1342.

[56] Mironova, I., C. Bockmann, and R. Nessler. *Microphysical Parameters from 3-Wavelength Raman Lidar*. in *ILRC*. 2002. Quebec: R&D Defence Library Services.

[57] Pappalardo, G., and al., *Algorithm intercomparison of the Raman lidar.* in EARLINET: Quality Assurance Report. internal note, 2001: p. 18-25.

[58] Magnus, G., *Versuche über die Spannkräfte des Wasser-dampfs.* Ann. Phys. Chem, 1844. 61: p. 225-247.

[59] Brilliant B Instruction Manual, October 2005.

[60] http://sky.ccny.cuny.edu/wc/Lidar.htmlc

[61] David M. Winker, NASA Langley Research Center, Chris A. Hostetler, NASA Langley, Research Center, Mark A. Vaughan, Science Applications International Corp. (SAIC), and Ali H. Omar, NASA Langley Research Center, *CALIOP Algorithm Theoretical Basis Document: Part I*, PC-SCI-202 Part 1 Release 2.0,September 9, 2006.

[62] Mark A. Vaughan, Science Applications International Corp. (SAIC), Hampton, Virginia, David M. Winker, NASA Langley Research Center, Hampton, Virginia, Kathleen A. Powell, Science Applications International Corp. (SAIC), Hampton, Virginia, *CALIOP Algorithm Theoretical Basis Document: Part II*, PC-SCI-202 Part 2 ,Release 1.01, 27 September 2006.

[63]http://wwwe.onecert.fr/pirrene/public/heliophotometre_DOTA/AERONET_technical_description.html

[64] Holben, B. N., T. F. Eck, I. Slutsker, D. Tanre, J. P. Buis, A. Setzer, E. Vermote, J. A. Reagan, Y. J. Kaufman, T. Nakajima, F. Lavenu, I. Jankowiak, and A. Smirnov, 1998: AERONET-A federated instrument network and data archive for aerosol characterization. *Remote Sensing of Environment*, 66, (1), 1-16.

[65] http://aeronet.gsfc.nasa.gov/